High-Performance Ferrite Nanoparticles for Magnetothermal Neural Excitation

by
Ritchie Chen

B.S Bioengineering and Materials Science and Engineering
University of California Berkeley, 2010

SUBMITTED TO THE DEPARTMENT OF MATERIALS SCIENCE AND ENGINEERING
IN PARTIAL FULFILLMENT OF THE REQUIREMENTS FOR THE DEGREE OF

DOCTOR OF PHILOSOPHY IN MATERIALS SCIENCE AND ENGINEERING
AT THE
MASSACHUSETTS INSTITUTE OF TECHNOLOGY
[June 2016]

Author Signature redacted
Department of Materials Science and Engineering
May 20, 2016

Certified by Signature redacted
Polina Anikeeva
Associate Professor of Materials Science and Engineering
Thesis Advisor

Accepted by Signature redacted
Donald R. Sadoway
Chairman, Department Committee on Graduate Students

High-Performance Ferrite Nanoparticles for Magnetothermal Neural Excitation

by

Ritchie Chen

Submitted to the Department of Materials Science and Engineering
on May 20, 2016, in partial fulfillment of the
requirements for the degree of
Doctor of Philosophy in Materials Science and Engineering

Abstract

Wireless and cell-specific manipulation of neural circuits may enable non-invasive treatment of the diseased brain. Existing neuromodulation methodologies lack cellular specificity and resolution (electrical deep brain stimulation (DBS)) or rely on transgenes (optogenetics), and require surgical implantation of conduits to deliver electromagnetic stimuli into the targeted deep brain structure. Using nanoscale materials with tunable properties, this thesis seeks to develop minimally invasive tools to facilitate wireless dissection of neural circuits and provide solutions beyond current surgical and pharmacological interventions to treat diseases. We rely on non-invasive alternating magnetic fields as a signaling modality to actuate magnetic nanoparticles to dissipate heat via hysteretic losses. The transduced thermal stimuli can then trigger the depolarization of heat-sensitized cells, leading to phasic excitation of neurons in arbitrarily deep brain structures. We first develop a general dynamic hysteresis model that can qualitatively predict loss power trends for ferrite nanoparticles of variable size and chemical composition in the presence of clinically relevant field frequencies and amplitudes. We then identify synthesis strategies to produce highly-crystalline magnetic nanoparticles with enhanced biomedical performance over previously described methods. With this optimized materials set, we demonstrate wireless control of neural circuits *in vitro* and *in vivo* by magnetothermal stimulation.

Thesis Supervisor: Polina Anikeeva

Title: Associate Professor of Materials Science and Engineering

Acknowledgements

I am grateful to my advisor, Professor Polina Anikeeva, whose resolve and mental clarity helped me immensely to complete this thesis work. Thank you for providing the resources and freedom for me to grow into an independent scientist. Seeing the lab grow was truly a wonderful adventure.

I want to thank my thesis committee members, Professors Darrell Irvine, Alan Jasanoff, and Caroline Ross, for their insight and feedback throughout the course of my PhD. Their guidance and belief really helped to solidify my scientific work, especially during manuscript preparations.

I want to thank all members of the Bioelectronics group for their help in lab and for their fruitful discussions, especially Michael Christiansen and Gabriela Romero, whose contributions to the modeling, electronics, and surface chemistry was foundational to this thesis work. I would also like to thank the many talented undergraduate—Alan Mohr, Allie Sourakov, Colleen Loynachan, Marissa Jasso, Moises Montalvo, and Mila'na Cherie—who helped me with many aspects of my experiments. Additional thanks to staff scientists Charlie Settens, Peter Muller, and Yong Zhang who helped me collect several key pieces of data. I want to acknowledge the various funding sources that funded my work: the NSF GRFP and CAREER award, Sanofi Biomedical Innovation Award, DARPA YFA and the ElectRx program.

Thank you to the Tech Masters Swim Team and coach Bill Paine for helping me stay fresh and focused, and to all my friends for the good times.

Finally, I dedicate my thesis work to my parents who have given me everything and whose unwavering support and love is a source of inspiration.

Contents

List of Figures

Chapter 1

1.1 Introduction

Large-scale research initiatives seek to further our understanding of the human brain, but will require advances in technology to enable fundamental discoveries [7]. No existing stimulation technology can trigger therapeutic responses in a minimally-invasive and cell-specific manner without relying on transgenes [8, 9]. Nanoscale materials, with tunable intrinsic properties and modular surface chemistries, represent a wealth of unexplored possibilities to engineer new molecular interfaces for spatiotemporal control of neural activity [10, 11]. This thesis integrates principles from materials physics and chemistry, protein engineering, and neuroscience to develop alternative modalities to stimulate intact neural circuits. Magnetic nanoparticles (MNPs) are capable of transducing a broad range of stimuli in the presence of magnetic fields, which can penetrate deep into the body due to the low magnetic susceptibility of tissue. In an alternating magnetic field (AMF), magnetic nanoparticles undergo hysteresis and dissipate heat, which, depending on the thermal dosage, can be used to induce apoptosis in tumors or control gene transcription and cell membrane depolarization in thermally-sensitized cells [4, 12, 13]. To evoke action potentials with sub-second latencies and perform chronic stimulation of arbitrarily deep brain structures, further optimization of this MNP platform is required.

To enable fast temporal control of neural activity, we first identified basic physical principles to maximize the specific loss power (SLP), a measure of heating efficiency, in a class of biologically benign magnetic oxides used therapeutically for magnetic resonance imaging and cancer hyperthermia [14, 15]. With this framework, we synthesized ferrite nanoparticles with the highest SLPs measured to date measured at AMF conditions within the limits of field amplitude and frequency products ($H{\cdot}f$) deemed clinically safe [1]. While well-established protocols exist to produce ferrite nanoparticles with controlled shape and size, we further identified a nonaqueous redox mechanism that allowed tuning of the magnetic state of the ferrite material. By improving the crystallinity of the nanoparticles, the SLPs were increased by nearly 500% in comparison to previously published methods [2]. The potent magnetothermal agents we developed enabled wireless stimulation of heat-sensitized neurons in vitro and in vivo within seconds [4]. In addition, the utility of this technology was demonstrated through chronic stimulation of intact neural circuits, where dopaminergic neurons in the ventral tegmental area (VTA) and its known projections could be excited a month after injection of the nanoparticle transducers.

1.2 Neuromodulation in the Clinical Setting

Current clinical neuromodulation relies on two strategies. The first is the administration of pharmaceuticals to treat neurological and psychiatric disorders such as Parkinsons disease (PD) and major depressive disorder (MDD). Serotonin and serotonin-norepinephrine reuptake inhibitors such as Prozac and Cymbalta are currently used to treat MDD, which act upon and increase levels of these neurotransmitters to improve mood, while drugs like Levodopa are converted into dopamine by dopaminergic neurons to diminish motor symptoms in PD patients. These drugs require weeks to years before the desired therapeutic effect is achieved and their systemic administration is often accompanied by unwanted side-effects. In many cases, patients are either unresponsive to these drugs, yields worsened symptoms, or loses its efficacy with time. Approximately 20% of MDD patients are drug-resistant and require alternative therapies [16].

When a patient is unresponsive to behavioral and drug therapy, surgical intervention may become necessary. Since the 1990s, implantable pacemaker technology has been combined with chronically implanted deep brain electrodes to treat various neurological disorders via deep brain stimulation (DBS) [17]. DBS has provided remarkable benefits to essential tremor and PD patients and was recently shown to alleviate the feeling of hopelessness and anhedonia in patients suffering from MDD [16]. While DBS of sub-cortical structures like the globus palluidus reduces all major motor manifestations of PD, its degree of benefit does not usually exceed the individual dosages of Levodopa [17]. Nevertheless, this therapy permits the reduction of medications and their accompanying side-effects with immediate therapeutic results. Likewise in stimulating the subgenual cingulate in MDD patients, patients described acute effects of "'sudden calmness or lightness [and a] disappearance of the void'" during DBS and continue to exhibit antidepressant response 2-3 weeks postoperatively [16]. However, DBS is a highly mechanically invasive procedure that requires surgical implantation of all three components: the pulse generator, the electrode leads, and the extensions connecting the leads to the generator. Several complications can arise postoperatively, including dislodging of a lead and unwanted electrochemical reactions at the electrode surface due to high voltage discharges of 4-12V. Furthermore, the molecular mechanism of DBS remains largely unknown [18].

Transcranial magnetic stimulation (TMS) and transcranial direct current stimulation (tDCS) are alternative non-invasive forms of neural stimulation. TMS involves the application of a time-varying magnetic field, which induces local electric field changes to disrupt neurological processes. Determining the extent and spread of this induced current and its effects on the stimulated area is difficult without more *in vivo* studies, and is exacerbated by the impossibility in differentiating between excitatory, inhibitory or state dependent effects [19]. tDCS is another form of neural stimulation that applies a constant current through electrodes to the brain area of interest [20]. However, these procedures have yet to demonstrate definitive therapeutic effects and suffer from poor spatial resolution and penetration depths limited primarily to the cortical surface. In light of the limitations of current treatments for neurological disorders, an alternative drug-free and minimally-invasive procedure for DBS is desired with specificity to cell type as well as high spatial and temporal resolution without attenuation of the signal.

1.3 Regulation of Action Potentials

Neurons and other excitable cells possess significantly polarized membranes that can transiently depolarize and generate action potentials [21]. Membrane voltage is regulated by the complex interplay between ion pumps and ion channels. The anatomy of an action potential is presented in **Figure 1.1**. Voltage sensitive sodium ion channels open in response to increased membrane potential, leading to sodium influx (**Figure 1.1.1**). Potassium ion channels follow suit to allow extracellular outflow of potassium. A net inward flux of cations can cause depolarization (**Figure 1.1.2**), which leads to the closing of the sodium channels at the peak of the action potential while leaving the potassium channels open. The continued efflux of potassium ions then hyperpolarizes the cell and returns the cell to its resting potential (**Figure 1.1.3**). The expression of voltage-gated sodium channel Na_V 1.3 and an inward rectifying potassium channel $K_{ir}2.1$ was

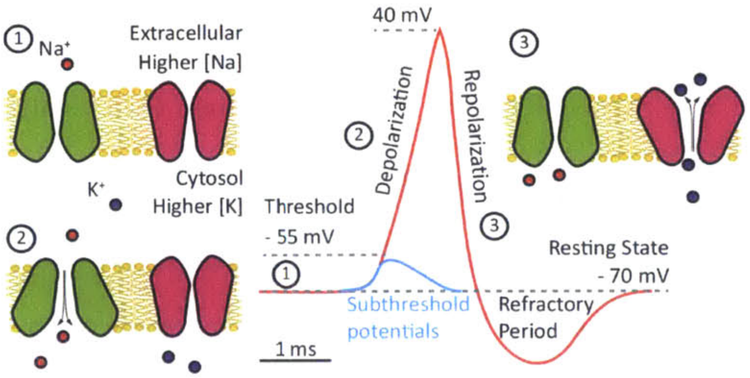

Figure 1.1 Membrane potential schematic. Upon crossing membrane threshold, neurons depolarize due to sodium influx of voltage-sensitive sodium channels. Repolarization occurs at the peak of action potential, where sodium and potassium channels close and open respectively, leading to hyperpolarization via potassium efflux. Resting potential is achieved from influx through passive potassium channels during the refractory period.

sufficient to generate action potentials in non-excitable human embryonic kidney cells [22]. Changing the membrane potential can lead to action potential propagation or silencing through hyperpolarization in neural networks. A number of transmembrane ion channels and pumps can respond to a variety of stimuli including chemical ligands, heat, and mechanical force, and may be integrated with nanoparticle technologies to regulate action potential firing by controlling membrane potential.

1.4 Thermally Sensitive TRP Channels

The transient receptor potential (TRP) ion channels have functional expression in many organisms and provide the molecular basis for our perception of temperature and pain. The common features of this ion channel superfamily include similar tetrameric structures consisting of 6 transmembrane domain subunits and permeability to monovalent and divalent calcium cations [23, 24]. Opening of TRP channels can depolarize cells from their resting membrane potential by raising intracellular calcium levels. This thesis is primarily concerned with the vanilloid receptor TRPV1, the most studied ion channel from the TRP family [23]. TRPV1 was initially isolated by expression cloning of the rat dorsal-root-ganglion library and assaying for capsaicin response [25].

TRPV1 was found to be involved in the transmission of nociception and high temperature stimuli, where acidic conditions, allyl isothiocyante, and temperatures greater than 43 °C all led to intracellular calcium increase. TRPV1 is endogenously expressed and can be found primarily in sensory neurons in the periphery as well as in the hippocampus and cortex of the central nervous system [26]. Delivery of the TRPV1 transgene can sensitize cells to heat and is a critical component in the magnetothermal stimulation scheme [12, 13].

1.5 Next-generation Neuromodulation Technologies

One of the most powerful tools currently used to dissect neural circuits to understand their function and causal behavior is optogenetics [8]. Neurons are genetically modified to express a class of microbial light-sensitive ion channels and pumps called opsins, which contains a light-sensitive retinal molecule within their core [8]. Optical stimulation with the appropriate wavelength results in the isomerization of retinal, leading to conformational changes of the opsin core and translocation of ions. Controlling cell membrane potential with light enables excitation and inhibition of neural activity with millisecond precision using engineered versions of the sodium channel channelrhodopsin-2 (ChR2) and chloride pump halorhodopsin (eNpHR) respectively. While optogenetics has offered insight into the molecular mechanisms behind a variety of behavioral and neurological disorders, the major limitation of this technique is the use of visible light as the external stimulus [27]. Because light is heavily attenuated by tissue [28], direct implantation of waveguides into the brain is required for optical stimulation. Nevertheless, cell-specific remote actuation of ion channels with light can achieve therapeutic effects in rodent models, such as the reduction of depression-like symptoms through phasic excitation of dopaminergic neurons in mice [18, 29-31].

An alternative non-invasive strategy to regulate neural activity is achieved with Designer Receptors Exclusively Activated by Designer Drugs (DREADDs) [32]. Membrane potential is modulated by G-coupled protein receptor evolved to only respond to synthetic ligands. For example, an evolved muscarininc receptor expressed in the hippocampus and cortex of mice induced limbic seizers upon binding of the pharmacologically inert ligand clozapine-N-oxide [33]. Poor temporal and spatial control due to slow and systemic infusion of the drug limits its efficacy to design neuromodulation studies requiring short time intervals.

1.6 Nanoparticle Approaches for Neuromodulation

Inspired by the mechanisms of neural electrophysiology, this thesis examines alternative forms of energy conversion that the body can recognize to modulate cell membrane potential with the same potency as optogenetics. The research findings detailed in this body of work seeks to release current technologies from the confines of wires and implants by shrinking neural probes to the scale of proteins with engineered nanomaterials. Nanoparticles can act as mediators that convert a wireless signal into localized stimuli at the neuron-nanomaterial interface [11]. For example, irradiation of gold nanoparticles with 532 nm light enabled rapid control of neural depolarization at frequencies up to 40 Hz via changes in membrane capacitance through photothermal heating [34]. The absorption wavelength can be redshifted by the introduction of a longitudinal plasmon band through the synthesis of gold nanorods [35], leading to photothermal neural stimulation in the near-infrared regime and the possibility of greater penetration depth [36]. Ultrasound coupling to ferroelectric barium titanate particles generated sufficient current to induce calcium influx in non-excitable glioblastoma cells [37]. However, these stimulation modalities will require conduits to access arbitrarily deep brain structures due to high scattering and absorption of light and sound waves in tissue.

Unlike electric field, light, and pressure stimuli that can damage tissue and have limited penetration depth, we focus on magnetic fields as an ideal stimulation modality because they interact weakly with biological matter [38]. Magneto-mechanical and magnetothermal strategies have been demonstrated to exert control over cellular signaling upon application of an external magnetic field. In magneto-mechanical conversion, magnetic nanoparticles (MNPs) apply mechanical force or torque to act on cellular targets to induce protein-clustering phosphorylation pathways and deformation of the cytoskeleton [39, 40]. However, sufficient force or torque requires the use of micron-size beads or the application of strong spatial field gradients, which is challenging for whole-body applications. More recently, heat dissipation via hysteretic power loss of MNPs was shown to trigger the opening of heat-sensitive calcium ion channels [12, 13]. Controlling the calcium influx into cells with alternating magnetic field (AMF) induced heating of MNPS allowed for on-demand action potential firing *in vitro* and gene transcription for insulin secretion *in vivo* [12, 13].

1.7 Thesis Structure

This thesis specifically focuses on optimizing the properties of magnetic nanoparticles for fast dynamic control of neural circuits through magnetothermal actuation. We describe the optimization of ferrite nanomaterials of composition ABO_4 for neuromodulation, which have been used previously in cancer hyperthermia and as MRI contrast agents in human patients [41, 42]. A dynamic hysteresis model was established to predict qualitative trends that guided the materials selection process for efficient magnetothermal transducers and new methods to synthesize high-performance nanoparticles were developed. The thesis concludes with experimental evidence of a minimally-invasive deep brain stimulation paradigm based on magnetically driven heat dissipation. The thesis is organized as follows:

- Chapter 2 reviews fundamental concepts of magnetic materials and ion channels.
- Chapter 3 examines existing methods to calculate loss powers in nanoparticles and proposes a general approach to calculate hysteresis loops.
- Chapter 4 compares current methods to synthesize monodisperse magnetic nanoparticles and improves upon established chemistries to produce highly-crystalline nanoparticles.
- Chapter 5 details the structural and magnetic properties of the magnetic nanoparticles.
- Chapter 6 establishes protocols to solubilize hydrophobic nanoparticles into water and correlates the nanoparticles' properties to its biomedical performance.
- Chapter 7 demonstrates the feasibility of magnetothermal neural excitation *in vitro* and *in vivo*.
- Chapter 8 summarizes the thesis's findings and discusses future directions.

Chapter 2
Background

2.1 Summary

Here we review the basic concepts of ferromagnetism and magnetic phenomena such as exchange coupling and magnetic anisotropy which can influence the magnetization process and the resulting hysteresis. We also motivate the use of the thermally sensitive TRPV1 channel to transduce magnetothermal heat stimuli.

2.2 Brief Introduction to Magnetism

Orbital and spin angular moments of electrons in atoms give rise to magnetic moments. In most materials, these magnetic moments are randomly oriented in the absence of an external bias field and exhibit no net magnetization. In magnetic materials, electrons in neighboring atoms interact to affect the overall spin state. This coupling between electron spin-angular moments is known as exchange interaction. Pauli's exclusion principle dictates that electrons with the same spin state cannot occupy the same orbital and hence must be far away from each other or be oriented antiparallel to each other to reduce their electrostatic repulsion. When there is sufficient overlap between wavefunctions, such as in 3d transition metals, a bond-length dependent exchange interaction, characterized by the Beth-Slater curve, will determine the configurational alignment of neighboring magnetic moments (**Figure 2.1**) [3]. *Antiferromagnetism* arise in materials with short interatomic distances that force neighboring electron spins to be oppositely aligned leading to no net magnetic moment. In *ferromagnetic* materials, exchange interaction favors spontaneous spin ordering along the same direction. Antiparallel electrons close to each other have spatially symmetric orbitals ψ_s with an antisymmetric spin function, while parallel spins share the same wavefunction confined to separate regions of space with antisymmetric orbitals ψ_a (**Figure 2.1**). Direct exchange occurs only when there is sufficient wavefunction overlap between moments, which decreases rapidly as the ions are separated.

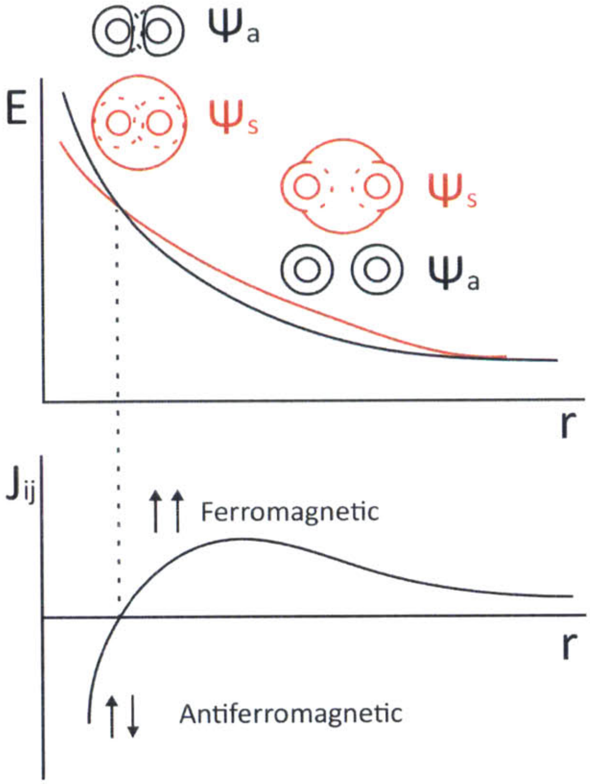

Figure 2.1 Beth-Slater curve. Energy versus atomic separation for spatially symmetric (red) and antisymmetric wavefunctions. Depending on sign of the exchange integral J_{ij}, antiferromagnetic or ferromagnetic coupling will be favored [3].

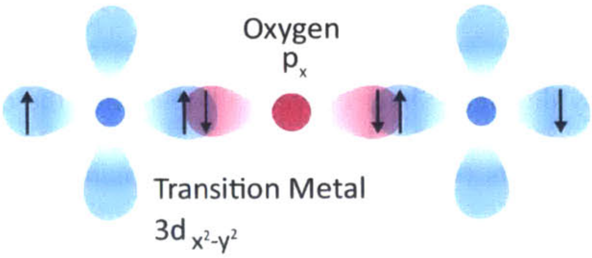

Figure 2.2 Schematic of superexchange interactions between transition metal (blue) and oxygen (red) [3].

For transition metal oxides, the magnetic ions are not close enough to experience direct exchange. Instead, superexchange interactions between the p_x orbital of the oxygen ion, which contains two electrons of opposite spin, force electrons in the $3d_{x^2-y^2}$ orbitals of neighboring metal ions to be antiferromagnetically aligned (**Figure 2.2**). For iron oxide in the rock salt structure (FeO), this interaction is strongest for 180° bonds and results in antiferromagnetic behavior below the Néel temperature (T_N = 192K). For inverse spinel iron oxide with ABO_4 structure, superexchange contributes to only partial cancelation between neighboring A-O-B ion pairs, leading to *ferrimagnetism*, or partial magnetic contribution from B site divalent ions.

2.3 Magnetic Properties and Biomedical Applications of Ferrite Materials

Ferrimagnetic ferrites have the chemical composition $MO{\cdot}Fe_2O_3$, where M can include divalent ions like manganese, iron, cobalt, and nickel. The atomic configuration adopts an inverse spinel structure consisting of oxygen ions forming a face-centered cubic lattice with the metal cations occupying both tetrahedral sites and octahedral sites, also referred to as A and B sites respectively (**Figure 2.3**) [3]. Ferrites, such as magnetite ($Fe^{2+}Fe^{3+}{}_2O_4$), are inverse spinel with 8 divalent ions occupy the B sites, and the 16 trivalent ions are equally divided between A and B sites. Of the ferrites studied in this thesis, only manganese and zinc doped ferrites are predominately normal spinel, with the manganese and zinc ions occupying A instead of B sites.

Tuning the magnetic properties of ferrites is enabled by the ability to manipulate the occupancy of the ferrite structure with different metal ions.

The strongest exchange interactions contained in metal-oxygen-metal bonds are between A and B site cations, with the cation's magnetic moment on the A site oriented antiparallel to the moment on the B site via superexchange interaction. Equal occupation of Fe^{3+} ions between A and B sites eliminates their contribution to the collective magnetic moment of the unit cell, with the magnetization of the unit cell determined primarily by divalent ions occupying the B site. Manganese ions, which have 5 Bohr magneton (μ_B) compared to the 4 μ_B on iron, contribute to a higher saturation magnetization in ferrite materials because the normal spinel configuration results in an additional μ_B uncompensated between A and B sites. The saturation magnetization of ferrite materials can also be increased by the introduction of diamagnetic zinc into A sites, enabling exchange interaction decoupling with Fe^{3+} on B sites such that the Fe^{3+} cations can contribute to the collective magnetic moment of the unit cell. Controlled incorporation of dopants into proper substitution sites is a convenient knob to tune the saturation magnetization of ferrite materials,

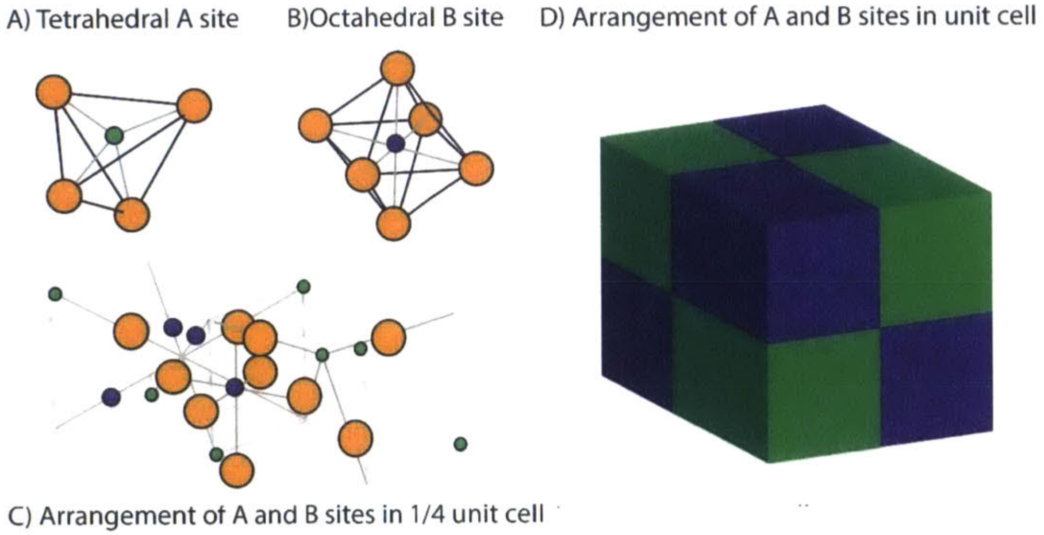

Figure 2.3 Inverse spinel crystal structure of cubic ferrite. A-site (green) and B-site (purple) coordinated metals with oxygen (orange) [3].

with nearly 2 fold enhancement over undoped iron oxide reported in mixed manganese and zinc doped ferrite nanoparticles [42].

The spin-orbital coupling within spinel ferrite can also be tuned via chemical composition to enhance the magnetocrystalline anisotropy of the ferrite material. Octahedrally coordinated Co^{2+} contribute to strong cubic anisotropy because of bond stabilization along the trigonal axis, where neighboring cations with trigonal arrangement disrupts the t_{2g} triple degenerate state of cobalt such that the highest occupied molecular orbital is the doubly degenerate state [43]. This results in spin-orbital coupling quantized along the <111> direction. In contrast, Fe^{2+} in a trigonal environment contains only a nondegenerate ground state, therefore no significant spin-orbit coupling to link the spin to the crystallographic direction is observed [3].

Wüstite is a nonstoichiometric rock-salt form of iron oxide. Wüstite is thermodynamically stable only above 560 degrees Celsius and has a tendency to decompose into α-Fe and magnetite at ambient conditions [44]. In a reducing environment, this metastable phase can be kinetically stabilized [45, 46]. Wüstite is weakly paramagnetic at room temperature and antiferromagnetic (AFM) below its Neél temperature [47]. Because magnetite and wüstite possess a face-centered cubic oxygen sublattice with the phase difference determined only by the coordination state of the iron ions, cation disorder may emerge during nanoparticle nucleation and growth [48-51]. Resulting phase impurities and defects lead to low hysteretic power losses and transverse relaxivities because of unfavorable exchange interactions between the AFM and FiM phases [50, 51]. Exchange coupling between the ferrimagnetic and antiferromagnetic face can pin the magnetization direction of the nanoparticle and prevent full coherent reversal in the presence of an alternating magnetic field [50].

Ferrite nanomaterials are generally biologically benign and widely studied for its diverse biomedical use [52, 53]. Commercial applications include magnetic separation of proteins and small molecules using micron sized beads embedded with MNPs, as contrast agents for magnetic resonance imaging, and for magnetic hyperthermia to destroy cancer cells [52, 53]. The latter technology, which utilizes an injection of a highly concentrated solution of iron oxide nanoparticles (100 mg/mL), has successfully undergone Phase II clinical trials to treat recurrent glioblastoma multiforme and doubled life expectancy [41, 54]. Because of its clinical viability and tunable magnetic properties through chemical composition, this thesis specifically optimizes ferrite nanomaterials for magnetothermal neuromodulation.

2.4 Exchange Coupling

When ferro- or ferri- magnetic (FM) materials are in intimate contact with antiferromagnetic (AFM) materials, the relative orientations of the magnetic moments between the two will be coupled due to exchange bias, which can be characterized by a displacement in the magnetization loop [3]. This effect appears below the T_N of the antiferromagnet. Above T_N, antiferromagnetic materials are paramagnetic.

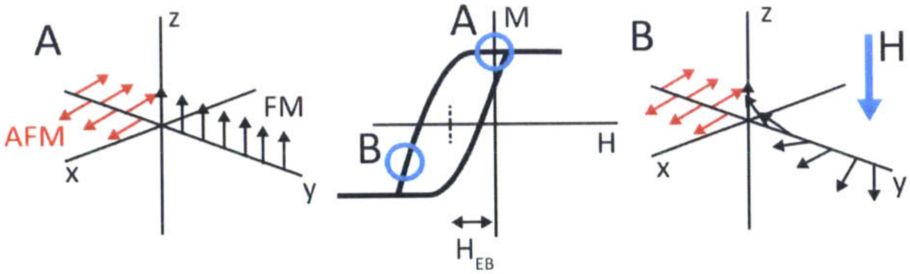

Figure 2.4 (A) Schematic of exchange coupling between antiferromagnetic (red) and ferromagnetic layers below the Néel temperature. (B) As a negative bias is applied, exchange field from the AFM layer requires an additional field to demagnetize the sample. Exchange coupling is seen in a shift in the magnetization (M) versus field (H) loop in the negative direction which is measured as exchange bias (H_{EB}) [3].

As the two-component material is magnetized under field-cooled conditions, a bias field H_{EB} exerted by the AFM material on the FM phase necessitates a stronger negative field to demagnetize the sample below T_N. This shift in the hysteresis loop towards the negative direction arises from this exchange coupling interaction, which gives rise to exchange anisotropy. The degree of exchange can be quantified by measuring H_{EB} (**Figure 2.4**).

2.5 Magnetic Anisotropy

The magnetic moment of a magnetically anisotropic material will tend to lie along an energetically favorable direction of the crystal axis. Spin-orbital coupling gives rise to magnetocrystalline anisotropy, where the nonzero angular momentum of the electrons couples with the crystal electric field to influence the magnetization direction to lie along specific crystal planes [3]. Ferrites have cubic magnetocrystalline anisotropy, which can be expressed to the second order as:

$$K_{cubic} = K_0 + K_1(\alpha_1^2\alpha_2^2 + \alpha_2^2\alpha_3^2 + \alpha_3^2\alpha_1^2) + K_2(\alpha_1^2\alpha_2^2\alpha_3^2) \qquad (2.1)$$

where α_1, α_2, and α_3 are direction cosines of the magnetization along the three coordinate axes. For bulk Fe_3O_4, the anisotropy constants K_1 and K_2 are $-1.3\cdot10^4$ and $-0.3\cdot10^4$ J/m^3 respectively at room temperature [55], which makes the easy axis of magnetization lie along the [111] direction in bulk material.

Symmetry breaking on facets and edges can contribute to significant surface anisotropy for nanoparticle clusters [56]. Spherical nanoparticles contain a higher number of nanofacets with higher spin disorder compared to nanocubes with flat faces [57]. The increased surface defect enhances the surface anisotropy of the nanospheres compared to nanocubes, and can exceed the magnetocrystalline anisotropy of the material [57]. The energy density contribution of surface anisotropy can be written as:

$$K_{surface} = \frac{6K_s}{d} \tag{2.2}$$

K_s is the energy per unit area localized at the surface and d the diameter or edge length of the nanoparticle.

For non-spherical magnetic samples, magnetization along a crystallographic direction can create stray fields, known as demagnetizing fields, which can also raise the sample's net energy. The energy density term associated with shape anisotropy is:

$$K_{shape} = \frac{\Delta N}{2} \mu_0 M_s^2 \tag{2.3}$$

where N is a tensor function of the sample's shape called the demagnetization factor, μ_0 is the magnetic permeability in vacuum, and M_s the saturation magnetization.

The effective anisotropy K_{eff} is a sum of all the anisotropy contributions of the nanoparticle, which includes the magnetocrystalline, surface, and shape anisotropy described in this section. Because the K_{eff} scales the height of the anisotropy energy barrier of the MNPs, proper derivations of its functional form is important in accurate calculations of the magnetization process of the nanoparticle ensemble in a time-varying magnetic field [58].

2.6 Magnetization Process

For single domain particles with uniaxial symmetry and fixed physical orientation, hysteresis is at maximum when the magnetization direction lies along the easy axis. As an external field is applied, the angular position of the moments are fixed and remain locally stable. Only when the field exceeds the anisotropy energy associated with the particle is there an abrupt switch in the magnetization of these domains. Magnetization curves as a function of the applied field H can be calculated by minimizing the free energy expression:

$$\frac{E_i}{V} = -M_s H \cos\theta_i + K_{eff}\sin^2\theta_i \tag{2.4}$$

where V is the volume of the particle, M_s is the saturation magnetization, and K_{eff} the uniaxial effective anisotropy of the particle. The switching field occurs when:

$$\frac{1}{V}\frac{dE_i}{d\theta} = M_s H \sin\theta_i + 2K_{eff}\cos^2\theta_i > 0 \tag{2.5}$$

where h $= \frac{M_s H}{2K_{eff}} > 1$. For h>1, the local stability at $\Theta = \pi$ vanishes and the magnetization of all the domains switches abruptly to $\Theta = 0$. The M-H curve at this condition is sketched out in the red dashed line of **Figure 2.5**. For h<0, locally stable solutions are seen in the black solid line.

The irreversible work done from this switching behavior leads to hysteresis and is lost as heat. The amount of heat released by the MNPs during one magnetization cycle is equal to the area A of the hysteresis loop, which is expressed as:

$$A = \int_{-H_o}^{H_o} \mu_o M(H)dH \qquad 2.6$$

Calculation of the magnetization process in a dynamic manner is considered in Chapter 3, where a general model is proposed that accounts for the MNP's properties and size as well as the frequency and amplitude of the magnetic field applied.

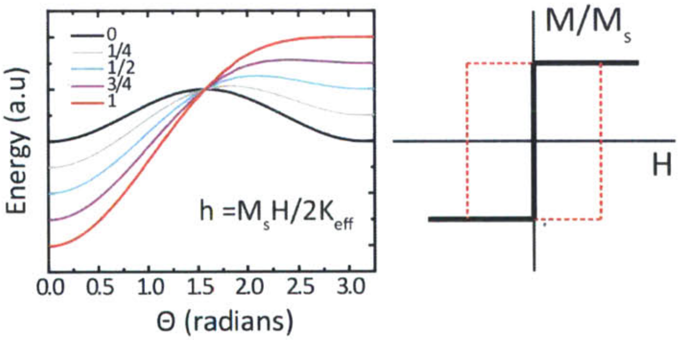

Figure 2.5 (Left) Single domain fixed particles with uniaxial symmetry exhibit two stable orientations at h<1. When h ≥1, all magnetization direction switches abruptly to $\Theta = 0$. The magnetization curve for these two conditions are given on the right for h<1 (black) and h ≥1 (red dashed line) [3].

Chapter 3

Theoretical Framework for Loss Power Predictions

3.1 Motivation

The ability to maximize hysteresis for efficient loss powers at a particular alternating magnetic field (AMF) frequency and amplitude relies on concomitant tailoring of the MNP properties to the AMF conditions and vice versa. The effective anisotropy energy (K_{eff}) of the MNP, which is dependent on its chemical composition, size, and shape, must be chosen such that this energy barrier for coherent magnetization reversal can be surmounted by the relatively modest AMF with amplitude-frequency product set by the Brezovich criterion $<H\cdot f = 5\times10^{9}\ \mathrm{A\cdot m^{-1}\cdot s^{-1}}$. This is crucial to avoid nonspecific heating generated by Eddy currents in the targeted volume from prolonged AMF exposure [38]. As a result, the AMF is generally limited to an amplitude range between 5 to 50 kA $\mathrm{m^{-1}}$ and operated at frequencies below 1 MHz. To maximize the heat dissipated

---

The content of chapter 3.3 was generated in collaboration with Michael Christiansen, and based on published work found in references [1] and [6].

as the MNPs undergo hysteresis loss within these field constraints, the saturation magnetization (M_s) and effective anisotropy energy (K_{eff}) of the material must be optimized.

Within this wide parameter space, where the loss powers of the MNPs depend on its chemical composition and size as well as the applied field conditions, developing a theoretical framework will help identify the most promising MNPs for clinical magnetic hyperthermia. Analytical expressions derived to calculate specific loss powers (SLPs) of magnetic nanoparticles tend to rely on linear response theory (LRT) [59-61], which is valid only when the magnetization of the MNP ensemble increases proportionally to the applied field [58, 62]. Particles with low anisotropy energy tend to saturate at relatively modest applied fields and can no longer be described by LRT. The alternative is to use the Stoner-Wohlfarth model, which is a zero temperature model that requires estimations of the coercive field H_C in order to account for temperature and frequency effects [63, 64]. Understanding the limits of either model is important for deriving accurate predictions of the material's performance in the presence of AMF. This chapter proposes the use of dynamic hysteresis theory as a general model towards identifying efficient magnetothermal transducers without restrictions towards the range of conditions applied [58].

3.2 Linear Response Theory

Linear response theory (LRT) was first proposed by Rosensweig to describe the power dissipation in a fluid containing superparamagnetic MNPs (ferrofluid) in the presence of AMFs [62]. This model approximates the area of the hysteresis loop as:

$$A = \Delta U = \mu_0 \pi \chi'' H_0^2 \tag{3.1}$$

which is the internal energy loss per cycle. The SLP is calculated by multiplying the energy loss per cycle of the magnetization process with the applied frequency (SLP=$A \cdot f$).

The frequency dependence of the complex susceptibility is given by the expression:

$$\chi'' = \frac{\mu_o M_s^2 V}{3k_b T}\frac{\omega\tau_R}{(1+\omega^2\tau_R^2)} \tag{3.2}$$

where M_s is the saturation magnetization, V is the volume of the MNP, $\omega = 2\pi f$ is the AMF sweep rate, and τ_R is the effective relaxation time. This relaxation time is denoted as:

$$\frac{1}{\tau_R} = \frac{1}{\tau_B} + \frac{1}{\tau_N} \tag{3.3}$$

and has contributions from both Neél and Brownian processes.

Neél relaxation characterizes the time the magnetic moment takes to flip between two stable orientations when sufficient thermal energy is present to overcome the MNP's anisotropy energy barrier. The Neél relaxation time τ_N is given by the following expression:

$$\tau_N = \tau_0 exp\left(\frac{K_{eff}V}{k_B T}\right), \tag{3.4}$$

with τ_0 being the intrawell relaxation time and is typically estimated to be 10^{-10} s and K_{eff} the effective anisotropy described in Section 2.5 [58].

In a ferrofluid, the relaxation time for physical rotation of the nanoparticle after perturbation is the Brownian time constant and its relation to η, the viscosity coefficient of the solution, is given by the following relationship:

$$\tau_B = \frac{3\eta V_H}{k_B T} \tag{3.5}$$

where V_H is the hydrodynamic volume. Putting equations (2.1)-(2.5) together, the overall expression for calculating SLP in the linear response regime is given as:

$$A = \frac{\pi\mu_0^2 H_{max}^2 M_s^2 V}{3k_b T}\frac{\omega\tau_R}{(1+\omega^2\tau_R^2)} \tag{3.6}$$

From these expressions, we can identify optimal material properties that should, in principle, yield highly dissipative MNPs. K_{eff} from 0.5 to $2 \cdot 10^4$ J/m^3 and a particle size between

10 to 30 nm exhibits maximum SLP at field frequencies of 500 kHz and amplitude of 10 kA/m (**Figure 3.1A**). The range in which we see this sharp maximum corresponds closely with the magnetocrystalline anisotropy (K_u) of spinel ferrites such as $MnFe_2O_4$ and Fe_3O_4, which is 3×10^3 and 1.6×10^4 J/m^3 respectively.

Figure 3.1B plots the SLP as a function of nanoparticle diameter for spinel ferrites with magnetocrystalline anisotropies varied over two orders of magnitude. Because of the high anisotropy constant of $CoFe_2O_4$ ($K_u = 2.0\times10^5$ J/m^3), the SLP value saturates with increasing size due to the dominance of Brownian relaxation contributing primarily to loss powers by frictional rotation of the particle. The maximum hysteresis loss observed corresponds to the condition when $\omega \cdot \tau_N = 1$, which occurs when the applied frequency is at the same rate as the relaxation time.

LRT aims to describe the response of the MNP ensemble using Neél-Brown relaxation and assumes that the magnetization of the MNPs scales linearly with the amplitude of the applied field. Use of LRT is appropriate when the applied field is far from the saturation regime of the MNPs

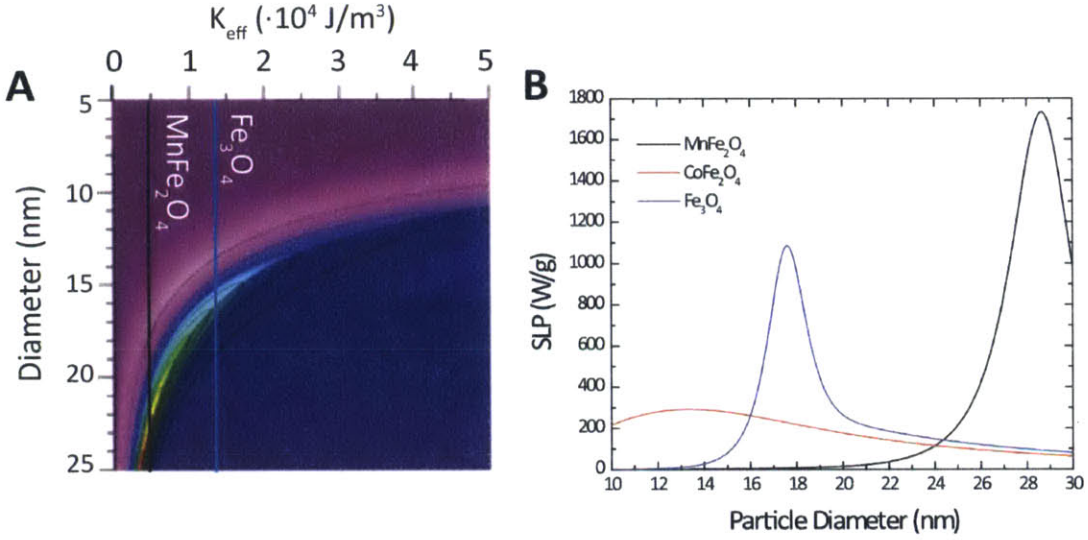

Figure 3.1 (A) Color intensity plot of SLP as a function of the effective anisotropy energy and size at 500 kHz and 10 kA/m. Slices of the intensity map are presented on right panel. (B) SLP as a function of size for the same field conditions for three kinds of ferrites: $MnFe_2O_4$ (black) Fe_3O_4 (blue) and $CoFe_2O_4$ (red).

(i.e when $H_o < 0.1 \cdot H_c$). However in most hyperthermia experiments, the key assumption that magnetization scales linearly with applied field is invalid, as it predicts that materials with low K_{eff} and large volumes to have the highest loss powers [59, 60]. If the applied field amplitude approaches the coercivity of the MNP, the magnetization of the nanoparticle ensemble will already be saturated. No additional power will be dissipated with increasing amplitude and the SLP will be saturated. Because LRT does not account for the effect of applied field on the Néel relaxation, erroneous overestimations of the SLP may occur.

3.2 Stoner-Wohlfarth Model

When the applied AMF amplitude H_o exceeds the coercive field H_C of the material, the entire hysteresis loop is accessed and linear response theory is no longer applicable. In this case, hysteresis losses can be derived from the Stoner-Wohlfarth (SW) model [63]. Because the SW model does not take into account any thermal activation, the model is only valid when temperature T = 0 K or when frequency f approaches infinity. Hence for experimentally accessible parameters, analytical or numerical expressions need to be derived.

The area of the hysteresis loop for the case of randomly oriented particles is:

$$A = 2\mu_0 H_C M_S \tag{3.7}$$

which is half the maximal area of oriented particles.

Frequency and temperature-dependent H_C can be determined from the expression:

$$\mu_0 H_C = \mu_o H_K \left(1 - \kappa^{1/2}\right) \tag{3.8}$$

Where $\mu_0 H_K$ is the magnetic field amplitude sufficient to suppress the anisotropy energy barrier and κ is a dimensionless magnetic dissipation parameter proposed by Usov et al. as [64]:

$$\kappa = \frac{k_B T}{K_{eff} V} \ln\left(\frac{k_B T}{4\mu_0 H_{max} M_s V f \tau_0}\right) \tag{3.9}$$

which accounts for the variation in coercive field with respect to AMF frequency. Comparison between hysteresis loops solved numerically and from the analytical expressions in 3.8 and 3.9 show good agreement for $\kappa < 0.5$.

LRT enables the calculation of the hysteresis area when the applied field amplitude is lower than the amplitude required to overcome the MNP's anisotropy energy barrier such that the relaxation timescale is unperturbed by the applied field. When the major hysteresis loop is accessed by applying high amplitudes to saturate the magnetization of the nanoparticle ensemble, SW analytical methods can be used so long as $\kappa < 0.5$. We utilize an alternative model for intermediate cases to numerically simulate hysteresis loops, which can qualitatively capture trends without being limited by the AMF conditions.

3.3 Dynamic Hysteresis Model

To account for the field amplitude's effect on the relaxation timescale, a general model is presented. This dynamic hysteresis model determines the M-H hysteresis loops of an ensemble of nanoparticle magnetic moments as it undergoes coherent reversal when surmounting a time-varying energy barrier that is dependent on the anisotropy and configurational energy of the MNP in the field [58]. The energy in this macrospin approximation can be written as:

$$E(\theta,\varphi) = K_{eff}V\sin^2(\theta) - \mu_0 M_s V H_{max}\cos(\theta - \varphi) \tag{3.10}$$

and can be rewritten in dimensionless parameters as:

$$\frac{E(\theta,\varphi)}{k_B T} = \sigma\sin^2(\theta) - \xi\cos(\theta - \varphi) \tag{3.11}$$

where $\sigma = \frac{K_{eff}V}{k_B T}$ and $\xi = \frac{\mu_0 M_s V H_{max}}{k_B T}$. We assumed easy-axis alignment as a predictive upper bound and set $\varphi = 0$. Assuming uniaxial symmetry, one can calculate the magnetization as a function of the occupation probabilities between the two minimas:

$$M = M_s(p_1 \cos\theta_1 + (1 - p_1)\cos\theta_2) \qquad (3.12)$$

The probabilities p_1 and $p_2 = 1\text{-}p_1$ are time dependent:

$$\frac{\partial p_1}{\partial t} = (1 - p_1)v_2 - p_1 v_1 \qquad (3.13)$$

and vary with the magnetization switching rate v_1 and v_2 between the two minima:

$$v_1 = v_1^0 exp^{\left(\frac{-\Delta E}{kT}\right)} \qquad (3.13)$$

$$v_2 = v_1^0 exp^{\left(\frac{\Delta E}{kT}\right)} \qquad (3.14)$$

For the sake of simplicity, the attempt frequency v_1^0 was set constant and equal to 10^{10} Hz [58]. The time evolution of p_1 can be determined with an explicit Runge-Kutta method. Loss power is then calculated by integrating over the hysteresis loop to determine the area.

As an estimate, the effective uniaxial anisotropy energy constant (K_{eff}) was taken to be approximately equal to the absolute value of the first order cubic magnetocrystalline anisotropy constant K_1. The effective anisotropy may be expanded to include effects from surface and shape as well. The transition of moments over the barrier is thermally activated, so that the expected power dissipation depends not only on the amplitude of the applied field's perturbation to the anisotropy energy landscape, but also the ambient temperature and cyclic timescale of the perturbation.

We first calculated hysteresis loops for magnetite Fe_3O_4 with varying diameters with applied AMFs at amplitude $H_o = 15$ kA m^{-1} and frequency $f = 500$ kHz (**Figure 3.2**) [1]. Due to surface effects, an effective uniaxial anisotropy is assumed for ferrite MNPs as long as the remanent to saturation magnetization ratio is less than 0.5, which can be experimentally determined [65]. These assumptions are made primarily for convenience and are expected to overestimate SLP values while making reasonable qualitative predictions. Neither perfect

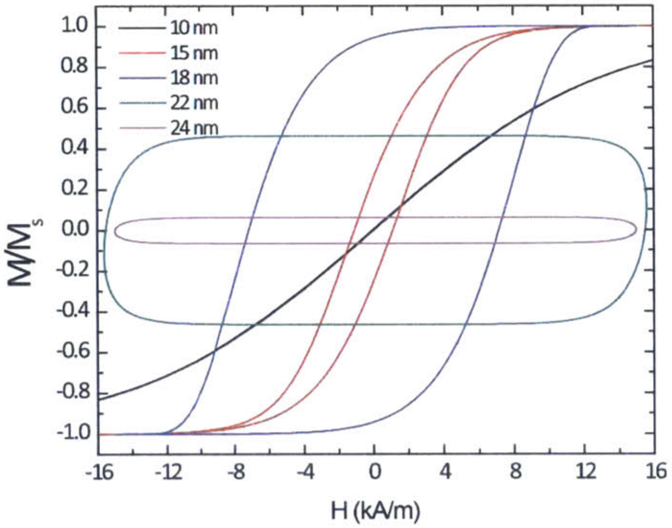

Figure 3.2 Field-dependent magnetization curves from numerical simulations for magnetite NPs of varying sizes in diameter. Field parameters used were H_o = 15 kA m^{-1} and f = 500 kHz.

alignment nor random alignment are well motivated assumptions for MNPs that can freely rotate, and the actual behavior would likely involve intermediate correlation and vary with the effective anisotropy energy of the MNP relative to the ambient thermal energy [58]. For MNPs with diameters less than 15 nm (at f = 500 kHz), the hysteresis loop appears almost reversible due to the negligible anisotropy barrier for the given temperature and frequency. This superparamagnetic behavior results in low power loss. As the energy barrier scales with MNP volume, $E_a \sim K_{eff} \cdot d^3$, the area of the hysteresis loop becomes significantly larger and displays a ferromagnetic shape at diameters above 15 nm. SLP reaches its maximum value for iron oxide MNPs with 18 nm diameters, which corresponds to a hysteresis loop with the largest area at the chosen field parameters. As the MNP diameter increases beyond 20 nm, the anisotropy energy increases such that the field amplitude no longer exceeds the coercive field and only minor hysteresis loops can be accessed, leading to a decrease in overall heat dissipation.

Figure 3.3 summarizes the SLP dependence on the diameter as well as the chemical composition of the MNPs at H_o = 15 kA m^{-1} and f = 500 kHz. Because the K_{eff} value of $CoFe_2O_4$

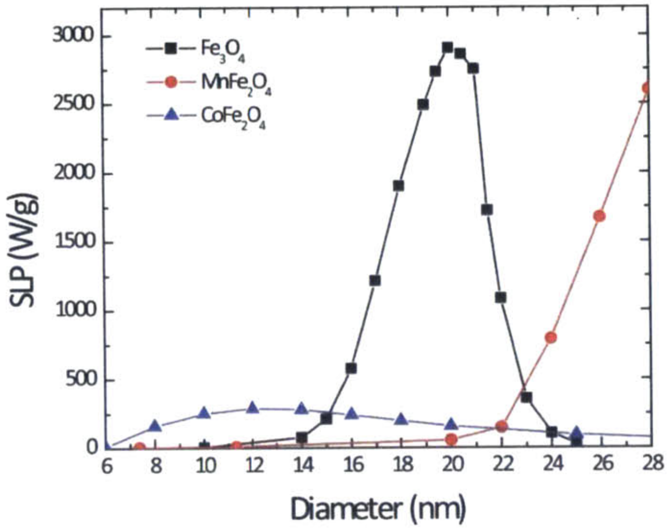

Figure 3.3 SLP calculated from numerical simulations for three different ferrite materials as a function of NP diameter. Field parameters used were $H_o = 15$ kA m^{-1} and $f = 500$ kHz.

is an order of magnitude greater than that of Fe_3O_4 ($K_{eff} = 2.0\times10^5$ J m^{-3} compared to 1.4×10^4 J m^{-3}), only minor hysteresis loops are accessed at the chosen AMF amplitude. We therefore used LRT to determine the SLP values for heat dissipation for $CoFe_2O_4$ nanoparticles, which dissipate heat primarily from the frictional heating generated by Brownian rotation of the particles. For $MnFe_2O_4$, the K_{eff} is an order of magnitude lower than that of Fe_3O_4, and requires larger nanoparticle diameters to exhibit significant hysteretic losses. In fact, we find that $MnFe_2O_4$ MNPs display high SLPs above 22 nm in diameter.

We also simulated SLP values for iron oxide nanoparticles at 100 kHz at various amplitudes and sizes to illustrate the difference in predicted trends between LRT and DH [6, 58]. Unlike **Figures 3.2-3.3**, which was an early iteration of the DH model, we accounted for thermal spreading of the moments about the easy axis following a Boltzmann distribution using a second order Talyor expansion to more accurately quantify the calculated loss powers [6]. Because LRT assumes that the magnetization of the ensemble increases linearly with H_o, SLP is predicted to also increase linearly as the applied amplitude (H_o) exceeds the coercive field (H_c) since the

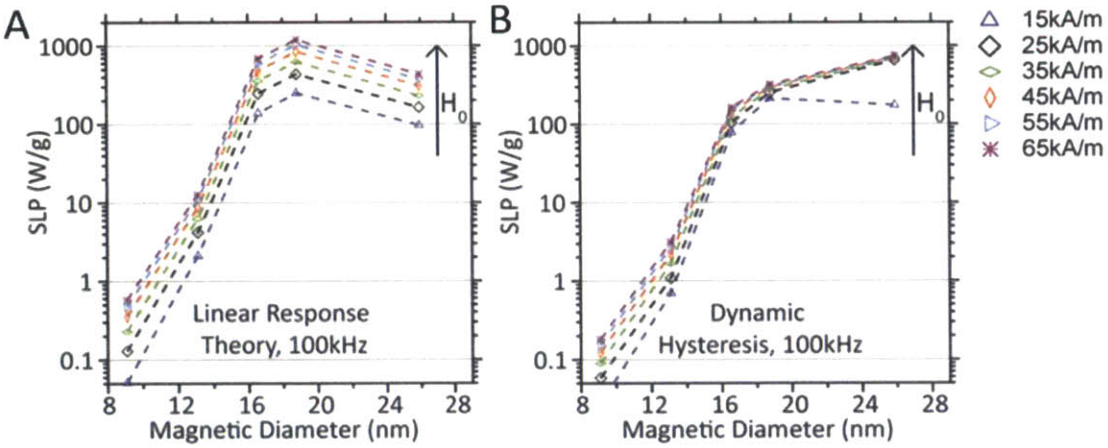

Figure 3.4 Theoretical SLP values simulated with (A) Linear Reponse Theory and (B) dynamic hysteresis as a function of magnetic diameter of iron oxide MNPs. Field conditions were *f* = 100 kHz at amplitudes from 15-65 kA/m as indicated in the legend right of this figure [6].

magnetization will increase without bound (**Figure 3.4A**). By contrast, DH theory predicts a saturation behavior, which arises from the saturation in magnetization of the nanoparticle ensemble as the field bias approaches and exceeds H_c (**Figure 3.4B**). The saturation behavior in SLP is a direct consequence of accounting for the field amplitude's effect on the stochastic rate of coherent reversal (**Equations 3.13** and **3.14**), which can also be accounted for with SW theory. Compared to LRT and SW theory, DH is a more general model that can predict SLP behaviors at clinically relevant field conditions.

In summary, iron oxide MNPs exceeding 20 nm in diameter are predicted to have the highest SLP values. Calculated values for $MnFe_2O_4$ indicate that hysteretic loss increases significantly only at particle diameters greater than 22 nm for the given field and frequency. $CoFe_2O_4$ MNPs do not yield significant heating at this field conditions (H_0 = 15 kA m^{-1} and *f* = 500 kHz) because the energy barrier is too high for the majority of the ensemble to align with the field. Furthermore, saturation behavior in the SLP is predicted as the field amplitude approaches and exceeds the coercive field. Correlation between simulated SLP values and empirically derived results will be presented in Chapter 6.

Chapter 4

Synthesis of Ferrite Nanoparticles with Tunable Size and Composition

4.1 Summary

In this chapter, synthetic protocols to produce ferrite nanoparticles with a wide range in composition and size are developed. While thermal decomposition methods offer unparalleled control over the size and shape of the ferrite nanoparticle, phase control over the various iron oxide polymorphs remains a synthetic challenge due to the local stabilization of thermodynamically unstable phases at nanoscale interfaces [47, 49, 66]. We have compared and contrasted published thermal decomposition methods to identify guidelines for the size and phase control of synthetic ferrites. New mechanistic insight into the solvent chemistry enabled one-pot scalable synthesis of tertiary ferrite MNPs with composition $M_{1-x}Fe_{2+x}O_4$, where M= Fe, Mn, Co and Zn. By creating an optimized MNP toolset with tunable size and composition, we can begin to correlate trends

---

The work described in this chapter was previously published in references [1].

predicted by dynamic hysteresis to experimental measurements of specific loss powers as a function of the nanoparticle's anisotropy energy.

4.2 Thermal Decomposition Method

The thermal decomposition method relies on heating synthetic precursors within a high boiling point solvent to liberate chelated ions to form nanoparticles under controlled nucleation and growth conditions. Depending on the choice of precursor, ligands, and solvent as well as the heating rate, reflux temperature, and annealing time, monodisperse nanoparticles of all shapes and sizes can be produced [5]. Two synthetic methods have been developed using this thermal approach. The first, demonstrated in the 1990s, used a hot injection method to rapidly introduce precursors into a heated solvent (> 150 °C) [67]. However, due to the complexity of this setup and inability to scale-up in a simple manner, this chapter will focus on the heat-up approach instead, which was developed in the early 2000s [68]. Briefly, ramping up a reaction containing precursors from room temperature until thermal decomposition (>250 °C) will enable nucleation and growth of nanocrystals. To gain an intuitive understanding of the various synthetic parameters of this heat-up approach, we consider the nanocrystal formation mechanisms that can influence both shape and size of the resulting nanoparticles.

LaMer first formulized the concept of nucleation and growth of monodisperse colloids within a closed system [69]. When the concentration of reactive monomers reaches a critical concentration and the reaction environment becomes supersaturated, there is a thermodynamic driving force to consume the monomers through nucleation. When monomers are depleted below a level such that the net nucleation rate is zero, the system enters a growth stage. Based on this kinetic process, defined separation between nucleation and growth enables monodisperse nanoparticles to be synthesized.

To better understand the synthetic parameters that govern LaMer kinetics, expressions for both nucleation and growth rate can be derived separately to simulate the reaction environment. To derive the nucleation rate as a function of supersaturation S, where $S = [\mathrm{M}]/[\mathrm{M}_\infty]$ (the monomer concentration at the nanoparticle's surface divided by bulk monomer concentration), the total free energy change of this system ($\Delta G(r)$) can be written as a sum of the surface energy and bulk energy contributions of the spherical nuclei [70]:

$$\Delta G(r) = 4\pi r^2 \gamma + \frac{4}{3}\pi r^3 \Delta G_v \tag{4.1}$$

where γ is the surface free energy per unit area and ΔG_v is the free energy per unit volume expressed as the difference between the free energy of monomers in the crystal and in solution.

$$\Delta G_v = -\frac{RT\ \ln S}{V_m} \tag{4.2}$$

V_m is the crystal's monomer molar fraction. The volume free energy term favors nucleation as long as the level of supersaturation S is greater than 1 such that there is a driving force to relieve excess free energy of the monomers in the supersaturated solution. Plotting the expression reveals that only when the nuclei is greater than the critical radius r^* will the particle resist dissolution, which can be found by solving for r when $\frac{\partial \Delta G(r)}{\partial r} = 0$ (**Figure 4.1**).

$$r^* = \frac{2\gamma V_m}{RT \ln S} \tag{4.3}$$

$$\Delta G(r^*) = \frac{16\pi\gamma^3 V_M^2}{3k_B^3 T^3 N_A^2 (\ln S)^2} \tag{4.4}$$

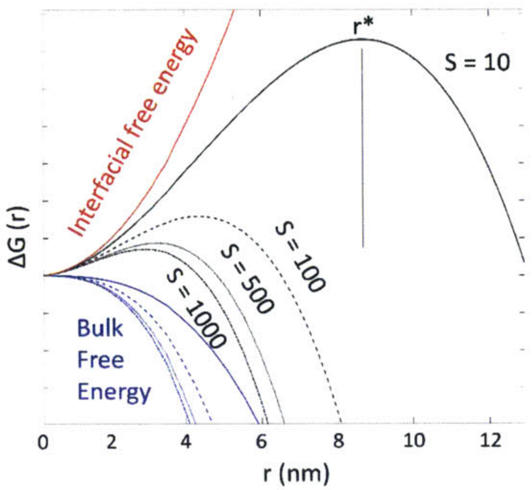

Figure 4.1 Plot of the interfacial (red), bulk (blue), and total (black) free energy contributions as a function of particle size for an arbitrary system at different supersaturation levels (S=100-1000). A barrier exists such that only nuclei of a critical radius r* will become stable.

As the supersaturation levels increase from 10 to 1000, the critical size of the nuclei r* drops drastically from S = 10-500 but with only moderate decrease >500. The sensitivity to supersaturation has significant impact on the quasi-steady-state nucleation rate, which can be written in the Arrhenius form as:

$$\frac{dN}{dt} = Aexp\left[\frac{-\Delta G(r^{*})}{k_B T}\right] \tag{4.5}$$

where N is the number of nuclei, and A is the pre-exponential factor written as:

$$A = Z\beta_c N \tag{4.6}$$

The Zeldovich factor Z is expressed as:

$$Z = \sqrt{\frac{\Delta G_c}{3\pi N_c^2 k_B T}} \tag{4.7}$$

which is typically on the order of magnitude of 10^{-1}. β_c is the rate at which monomers from the solution join the nucleated cluster. For a reaction performed at 250 °C using typical reaction conditions [5], the influence of supersaturation on nucleation rate is significant at low to moderate

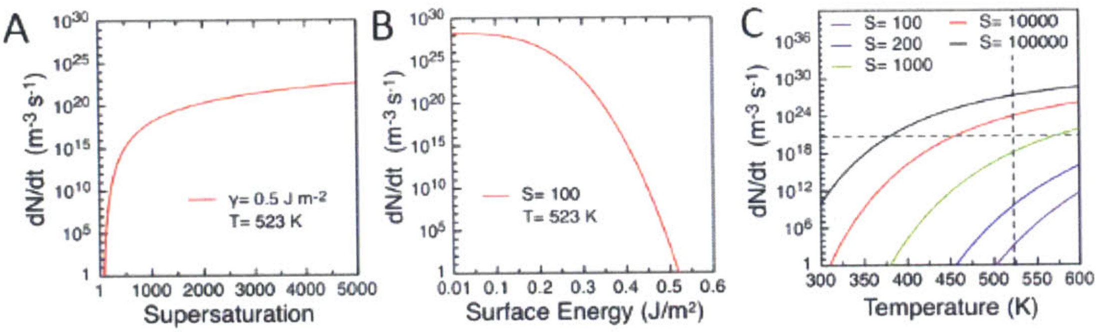

Figure 4.2 Calculated nucleation rate profiles as a function of (A) supersaturation, (B) surface energy and (C) temperature. Dashed line indicates approximate nucleation rates (1 μM/s) and growth temperatures for most heat-up synthesis (523K). This figure was taken from reference [5].

supersaturation (**Figure 4.2A**). This variability is primarily due to significant changes in the critical size of the nuclei observed in **Figure 4.1**, which has negligible decrease at higher supersaturation levels $S > 1000$. The type of ligand used can also significantly influence nucleation rate by varying the ligand affinity to the nanoparticle surface (**Figure 4.2B**). Furthermore, because the liberation of monomers from precursors is highly sensitive to temperature, we can see that nucleation rate is increased with increasing temperature (**Figure 4.2C**). Increasing the supersaturation results in both higher nucleation rates and higher sensitivities to increased temperature. From this simplified rate equation for homogeneous nucleation, 3 experimentally controllable parameters are identifiable: the level of supersaturation, surface free energy, and temperature [70].

During growth, the flux of monomers to the particles surface (J) is proportional to the concentration gradient around the particle of radius r times the diffusion coefficient D according to Fick's first law [5]:

$$J = 4\pi r D([M] - [M_i]) \tag{4.8}$$

$[M_i]$ is the monomer concentration at the nanoparticle interface. The flux can also be rewritten as a first order surface reaction:

$$J = 4\pi r^2(k_r[M_i] - k_d) \tag{4.9}$$

where k_r and k_d are growth and dissolution rate constants respectively.

From 4.8 and 4.9, $[M_i]$ can be rewritten as:

$$[M_i] = \frac{D[M] + k_d r}{k_r r + D} \tag{4.10}$$

The growth rate can also be related to monomer flux through Fick's second law:

$$J = \frac{4\pi r^2}{V_M}\frac{dr}{dt} \tag{4.11}$$

Equating 4.8 to 4.11 and using the relationship derived in 4.10:

$$\frac{dr}{dt} = \frac{DV_M\left\{[M] - \frac{k_d}{k_r}\right\}}{r + \frac{D}{k_r}} \tag{4.12}$$

Because the equilibrium constant $K_e = \frac{k_r}{k_d}$ is related to the equilibrium monomer concentration $[M_e]$ through the Kelvin equation:

$$[M_e] = \frac{1}{K_e} \tag{4.13}$$

$$[M_e] = [M_\infty]exp\left[\frac{2\gamma V_M}{rRT}\right] \tag{4.14}$$

4.12 can be rewritten using this relationship expressed in 4.13 and 4.14 as [5]:

$$\frac{dr}{dt} = \frac{Q\left\{S - exp\left[\frac{2\gamma V_M}{rRT}\right]\right\}}{r + \xi} \tag{4.15}$$

S is the level of supersaturation, $\xi = \frac{D}{k_r}$ and $Q = DV_M[M_\infty]$.

Based on these derivations, time dependent simulations of the reaction parameters can be performed. A typical heat-up synthesis will resemble the profile seen in **Figure 4.3**. As monomers are liberated during pyrolysis of organometallic precursors, supersaturation reaches a critical point to promote the formation of nuclei. This occurrence results in significant increase in the nucleation rate and the resulting nanocrystal concentration. As monomer concentration is consumed to fuel formation of nuclei, decline in nucleation rate from its apex coincides with the the onset of growth. Due to early stage Ostwald ripening, polydispersity in the nanoparticle size will be observed during the initial growth period. Further reaction time during the growth regime will size focus the nanoparticles with small size distribution. Once remaining monomers are depleted, the nanoparticles will have reached its equilibrium size, concentration, and distribution.

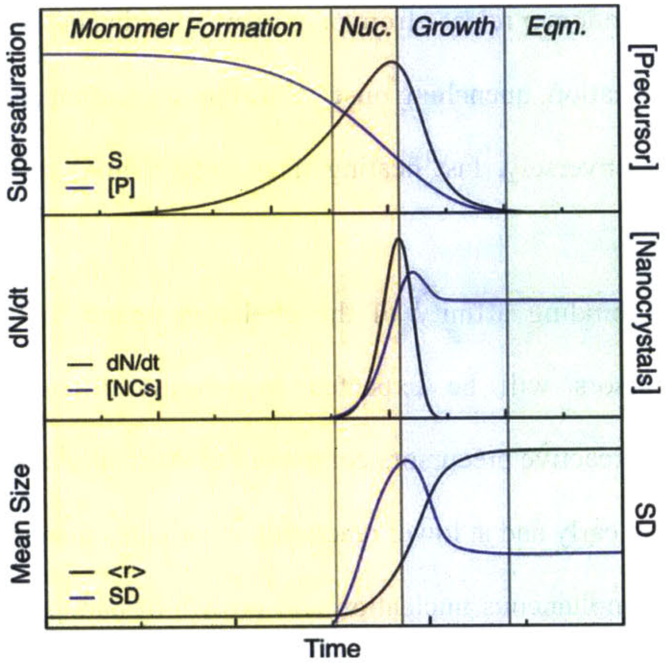

Figure 4.3 (Top) Monomer formation follows LaMer kinetics. Nuclei begin to form at supersaturation, which consumes liberated monomers. When monomer concentration falls below nucleation conditions, the reaction enters the growth phase. [P] is the precursor concentration and S is the level of supersaturation. (Middle) The nucleation rate increases sharply at supersaturation and ceases to commence once monomers are consumed. dN/dt is the nucleation rate and [NC] the concentration of nanocrystals formed. (Bottom) As the nucleation rate declines, the particles enter a growth stage where early Ostwald ripening helps size focus the size range of the nanoparticles to promote monodispersity. <r> is the mean size of the nanocrystal and SD the size distribution. This figure was taken from reference [5].

4.3 Experimental Parameters for Controlled Synthesis

A key requirement to synthesize monodisperse nanoparticles with the heat-up method is defined separation between nucleation and growth. Without defined boundaries between the two stages, simultaneous nucleation and growth will contribute to the polydispersity of the sample.

Changes in experimental parameters such as heating rate and precursor reactivity can determine the viability of a particular synthesis design. A general synthetic method for both tunable composition and size is necessary to correlate empirical with simulated results.

Because nucleation rate depends exponentially on temperature, heating rate is expected to have a profound impact on the size and polydispersity of the sample. Slow heating rates (0.1-5 K/min) will delay the monomer release from precursors such that nascent nuclei will begin to grow at faster rates then nucleation, quenching onset of further nucleation and favoring the formation of large nanoparticles. Conversely, fast heating rates (>10 K/min) results in rapid nucleation of smaller nanoparticles.

Based on the binding affinity of the chelating ligand to the metal center, different organometallic precursors will be expected to possess different activation energies for decomposition. Highly reactive precursors comprised of short alkyl metal complexes are expected to form supersaturation early and at lower reaction temperatures than the reflux temperature of the solvent, resulting in simultaneous nucleation and growth of nanoparticles. Compounded by the tendency for nanoparticles to undergo Ostwald ripening at higher temperatures as the reaction proceeds to its boiling point, polydispersity in the synthesized nanoparticles is expected. By increasing the alkyl chain length, higher activation energies of the precursor will lead to decomposition temperatures closer to the reflux temperature of the solvent. This temperature matching will be expected to promote gradual supersaturation needed to separate nucleation and growth to achieve monodispersity.

4.4 Experimental Methods and Synthetic Protocols

4.4.1 Fourier Transform Infrared Spectroscopy (FTIR)

FTIR is a convenient spectroscopic tool to infer chemical species in a given sample. A Fourier transform is performed on raw data collected from a detector to identify phase differences as infrared light is passed through an interferometer and the sample. The infrared absorbance spectra collected reveals resonant frequencies characteristic of the sample's structure. FTIR was used in this thesis to identify reaction components of the synthesis. Aliquoted reactions collected at different time points were diluted 1:10 in chloroform. 10 μL of this solution was drop-casted then sandwiched between NaCl windows (International Crystal Laboratories). FTIR spectra was collected on a Thermo Fisher FTIR6700 Spectrometer using transmission mode. Aliquots during the course of a reaction were drawn using a 1 mL gas-tight Hamilton syringe.

4.4.2 High-resolution Transmission Electron Microscopy (HRTEM)

To form an image of nanoparticles, electrons in a HRTEM are focused and transmitted through the sample, enabling images to be detected by a CCD camera as electrons interact with the sample. The short wavelength at high acceleration voltages (2-15 pm) enables sub-angston resolutions to be imaged. Electron diffraction patterns can be obtained to examine the crystal structure of the sample. As-synthesized MNPs dispersed in hexane were drop casted onto carbon-coated copper grids (Ted Pella Inc.) and washed three times with methanol. TEM images were taken using a JEOL 2010F electron microscope at 200 kV.

4.4.3 Preparation of metal-oleate complex

The metal-oleate $MFe_2(C_{18}H_{33}O_2)_8$ precursor (where M=Co^{2+}, Fe^{2+}, Mn^{2+}) was prepared by reacting sodium oleate and the respective metal chloride salt as previously reported [68, 71]. We scaled our preparation such that the total metal content was 60 mmol per reaction. An example synthesis for a binary metal complex $M_2(C_{18}H_{33}O_2)_8$ was prepared by dissolving 40 mmol of $FeCl_3$, 20 mmol of $CoCl_2$, and 160 mmol of sodium oleate in 100 mL of ethanol, 100 mL of filtered de-ionized water, and 200 mL of hexane and heated to reflux at 60 °C for 4 hours. After removal of the aqueous phase, the organic phase was heated to 70 °C for 2 hours and then placed under vacuum at 110 °C for an additional 2 hours to remove residual solvent, leaving behind a highly viscous metal-oleate product. For ferrite nanoparticles prepared by co-solvent methods, the metal-oleate protocol was modified to improve batch-to-batch consistency: In a 1 L 3 neck flask, 30 mmol of $FeCl_3{\cdot}6H_2O$ and 92 mmol of sodium oleate was heated to reflux (60 °C) in a solvent mixture comprised of 200 mL of hexane, 100 mL of ethanol, and 100 mL of ddH_2O for one hour under N_2. The hexane layer containing the iron-oleate complex was then extracted with a separatory funnel and washed twice with ddH_2O. The iron-oleate mixture was heated to 110 °C in a beaker and dried overnight stirring on a hotplate. Preparation of binary metal-oleate complexes can be made by simply adapting the stated protocol while balancing the charge stoichiometry when Fe3+ is substituted with M2+ (where M=Co^{2+}, Fe^{2+}, Mn^{2+} or Zn^{2+}).

4.4.4 Synthesis of monodisperse and spherical MFe_2O_4 nanocrystals of different sizes from metal-oleate precursors.

To synthesize 15 nm in diameter iron oxide nanoparticles, 5 mmol of the metal-oleate complex and 2.5 mmol of oleic acid was dissolved in 25 mL of 1-octadecene in a 250 mL 3-neck flask and evacuated for 30 minutes. Then the solution was heated to 200 °C under nitrogen flow and further heated to 310 °C at a rate of 1 °C/min and held at the specified temperature for 1 hour. After precipitation and washing, the nanocrystals were then dispersed in toluene after. 10 nm, 18 nm, and 23 nm MNPs were synthesized by setting the final temperature to 305 °C, 320 °C, and 325 °C respectively. 26 nm MNPs were prepared by setting the final temperature to 330 °C in 25 mL of 1-eicoscene.

To synthesize $MnFe_2O_4$ 15 nm MNPs, 5 mmol of the metal-oleate complex and 2.5 mmol of oleic acid was dissolved in 10 mL of 1-octadecene in a 250 mL 3-neck flask and evacuated for 30 minutes. Then the solution was heated to 200 °C under nitrogen flow and further heated to 315 °C at a rate of 1 °C/min and held at the specified temperature for 1 hour. 10 nm and 18 nm MNPs were synthesized by setting the final temperature to 305 °C and 325 °C respectively. 28 nm MNPs were prepared by setting the final temperature to 330 °C in 10 mL of 1-eicoscene.

To synthesize $CoFe_2O_4$ 13 nm MNPs, 5 mmol of the metal-oleate complex and 2.5 mmol of oleic acid was dissolved in 25 mL of 1-octadecene in a 250 mL 3-neck flask and evacuated for 30 minutes. Then the solution was heated to 200 °C under nitrogen flow and further heated to 305 °C at a rate of 1 °C/min and held at the specified temperature for 1 hour. 20 nm MNPs were preparing by setting the final temperature to 310 °C with a change in heating rate from 1 °C/min to 3 °C/min.

4.4.5 Synthesis of highly-crystalline single phase $MnFe_2O_4$ nanocrystals of different sizes from metal acetylacetonate (acac) precursors.

7 nm $MnFe_2O_4$ MNPs were synthesized by previously reported methods in a 250 mL 3-neck flask [72]. To increase the size of the MNPs, $MnCl_2$ instead of $Mn(acac)_2$ was used. 11 nm MNPs were

synthesized by mixing Fe(acac)$_3$ (2 mmol), MnCl$_2$ (1 mmol), oleic acid (6 mmol), oleylamine (6 mmol), 1,2-hexadecanediol (10 mmol), and 20 mL of benzyl ether and evacuated for 30 minutes. Then the solution was heated to reflux for one hour at a rate of 3.3 °C/min under nitrogen flow. MNPs 16 nm in diameter were synthesized by mixing Fe(acac)$_3$ (2 mmol), MnCl$_2$ (1 mmol), oleic acid (6.31 mmol), oleylamine (12.16 mmol), and 2 mL of dioctyl ether and heated to 200 °C under nitrogen flow for 2 hours. The reaction was further heated to 330 °C at a rate of 3.3 °C/min. To grow MnFe$_2$O$_4$ MNPs greater than 20 nm, 50 mg of 11 nm MNP seeds dispersed in hexane was added to Fe(acac)$_3$ (2 mmol), MnCl$_2$ (1 mmol), oleic acid (6 mmol), oleylamine (6 mmol), 1,2-hexadecanediol (10 mmol), and 20 mL of benzyl ether and evacuated for 30 minutes at 60 °C. Then the solution was heated to reflux for one hour at a rate of 3.3 °C/min under nitrogen flow.

9 nm CoFe$_2$O$_4$ MNPs were synthesized by previously reported methods in a 250 mL 3-neck flask [72]. To increase the size of the nanoparticles, MnCl$_2$ instead of Mn(acac)$_2$ was used. 11 nm MNPs were synthesized by mixing Fe(acac)$_3$ (2 mmol), CoCl$_2$ (1 mmol), oleic acid (6 mmol), oleylamine (6 mmol), 1,2-hexadecanediol (10 mmol), and 20 mL of benzyl ether and evacuated for 30 minutes. Then the solution was heated to reflux for one hour at a rate of 3.3 °C/min under nitrogen flow.

4.4.6 Synthesis of magnetic nanoparticles with different solvents and co-solvents.

In a 250 mL 3 neck flask, 5 mmol of iron-oleate, 2.5 mmol of oleic acid, and 20 mL of solvent (octadecane, 1-octadecene, squalene, dioctyl ether, or dibenzyl ether) was degassed at 90 °C for 30 minutes. Then the mixture was heated to 200°C under N$_2$, then to reflux at 3.3 °C/min and held at the reflux temperature for 30 minutes. The nanoparticles were extracted by transferring the reaction solution into 50 mL conical tubes, adding 30 mL of ethanol to promote flocculation, then precipitated by centrifuging at 10,000 rpm for 10 minutes. Following two washes (disperse in hexane followed by the addition of ethanol then centrifugation), the nanoparticle pellet was re-dispersed in 5 mL of chloroform. For co-solvents, 5 mmol of iron-oleate and 5 mmol (10 nm), 10 mmol (15 nm), 12.5 mmol (19 nm), or 15 mmol (27 nm) of oleic acid was combined in a 2:1 volume ratio of 1-octadecene (10 mL) and dibenzyl ether (5 mL) and degassed at 90 °C for 30 minutes. Then the mixture was heated to 200°C under N_2, then to reflux (325 °C) at 3.3 °C/min and held at the reflux temperature for 30 minutes. After pelleting and washing, the nanoparticle pellet was re-dispersed in 5 mL of chloroform.

4.4.7 Oxidation of as-synthesized nanoparticles.

After cooling the reaction solution to room temperature, 15 mmol of trimethylamine N-oxide was added, heated to 140 °C in air, and allowed to react for 30 minutes. An alternative air-oxidation protocol is presented in **Section 6.3.2**.

4.4.8 Washing step to pellet nanoparticles

After removing the heating mantle and cooling to room temperature, all reaction solution was transferred to a 50 mL conical tube along with a 1:1 mixture of ethanol and hexane. The sample was centrifuged at 9000 rpm for 10 minutes to collect the synthesized nanocrystals. The pelleted nanocrystals was redispersed in 10 mL of hexane and flocculated with 5 mL of ethanol and centrifuged at 9000 rpm for 10 minutes twice to remove excess ligand and solvent.

4.5 Thermal Decomposition of Metal-Oleate Compounds

A MNP material set was first synthesized from the thermal decomposition of metal-oleate precursors because of the ease in which size can be tuned above 10 nm [68, 71]. Slight modifications to the procedure were made because we found that the previously reported heating rate yielded faceted MNPs in our reaction conditions. By reducing the heating rate from 3.3 °C/min to 1 °C/min, monodisperse and spherical iron oxide MNPs with a size-distribution of less than 5% were produced. Nanoparticles 12 nm in diameter were synthesized at 3.3 °C/min [68], which increased to 22 nm with a slower ramp rate of 1 °C/min. This size increase is consistent with a delayed nucleation onset, where a smaller number of total nuclei are formed due to the rate of nuclei formation being faster than the rate of monomers generated [5]. As a result, rapid quenching of the nucleation rate leads to the remaining monomer reservoir to contribute to the growth of larger nanoparticles. Similar trends were also observed in the synthesis of $MnFe_2O4$ and $CoFe_2O_4$ MNPs. While it has been hypothesized that nucleation and growth occur separately at 240 °C and ~300 °C respectively [68], recent reports show that the transition occurs within 10 °C of each other

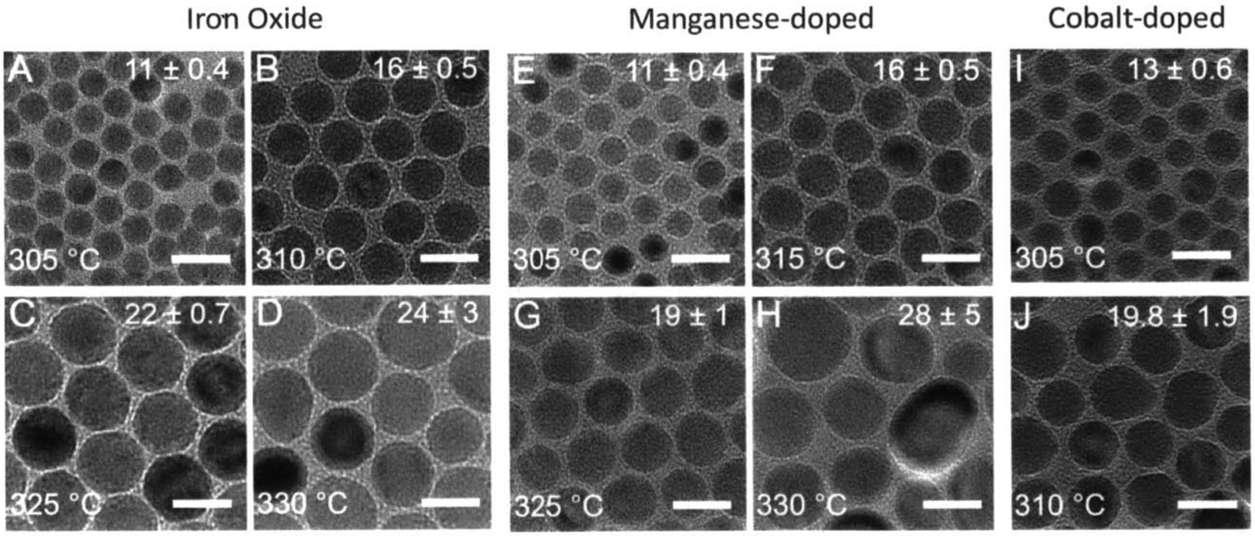

Figure 4.4 Transmission electron microscopy (TEM) images of monodisperse MFe_2O_4 MNPs of various sizes synthesized from the thermal decomposition of metal oleate precursors. (A-D) Iron Oxide (E-H) Manganese Ferrite (I,J) Cobalt Ferrite [1]. Scale bar = 20 nm.

[73], and that the bulk of the homogeneous nucleation occurs above 300 °C [74, 75]. This suggests that a faster heating rate will result in overlap between nucleation and growth. By reducing the heating rate to 1 °C/min, gradual increase to supersaturation resulted in defined separation between the two stages.

Rather than tuning the size based on the reflux temperature of the solvent as reported previously [68], a simple change to the final annealing temperature in 1-octadecene (ODE, b.p ~320 °C) enabled access to a wide range of MNP diameters. Transmission electron micrographs of the ferrite MNPs produced by this method can be seen in **Figure 4.4**. In the case of iron oxide, particle size varying from 10 to 22 nm in diameter was synthesized by setting the temperature from 305 to 325 °C (**Figure 4.4 A-D**). Higher annealing temperatures promoted more monomers to be generated, which can fuel the growth of nanoparticles towards larger sizes. Of note is the appearance of core-shell morphology in these nanoparticles indicative of two phase components. While these MNPs were previously described as single-crystalline [68], this unexpected feature will be addressed in Sections 4.8-10 and in Chapter 5. Under the same reaction conditions, $MnFe_2O_4$ MNPs were cubic in shape. To promote supersaturated isotropic growth the solvent amount was decreased from 25 mL to 10 mL. In 10 mL ODE, nearly spherical $MnFe_2O_4$ MNPs 10 to 18 nm in diameter were synthesized when the final temperature was varied from 305-325 °C (**Figure 4.4 E-H**). Further decreasing the solvent to 5 mL led to larger polydisperse MNP samples.

4.6 Thermal Decomposition of Metal Acetylacetonate compounds

While metal-oleate decomposition in solvents exceeding 300 °C produced nanoparticles in the superparamagnetic to ferromagnetic transition regime suitable for magnetic hyperthermia, the observed core-shell morphology was indicative of defects and unwanted phases which is expected to impact the resulting magnetic properties and the measured specific loss powers [46, 49]. The synthesized nanoparticles should exhibit bulk-like magnetic properties of ferrite materials to correlate empirical values with expected trends predicted by the dynamic hysteresis model presented in Chapter 3. We find that the thermal decomposition of metal acetylacetonate precursors can produce monodisperse MFe_2O_4 MNPs with magnetic properties approaching those of bulk tertiary ferrites, but a seed-mediated growth process is required to synthesize the MNPs above 10 nm [72]. In an attempt to develop a one-pot synthesis method, we varied both heating

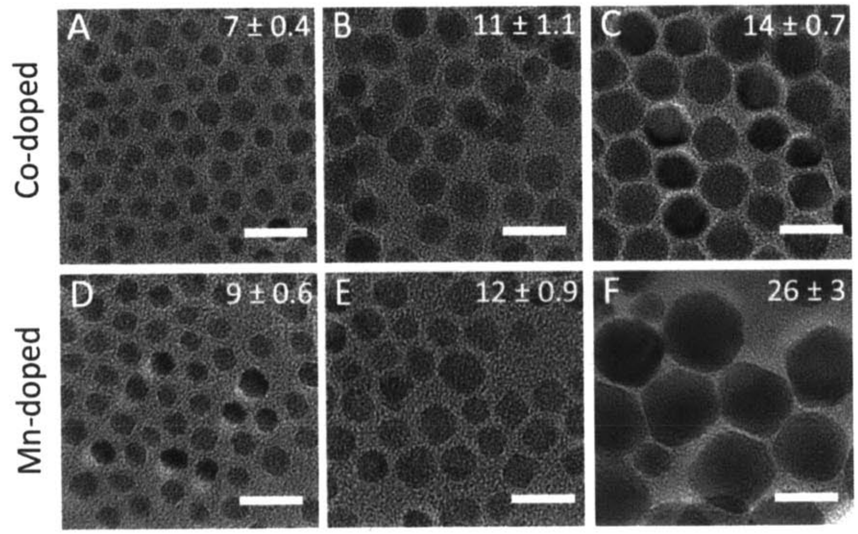

Figure 4.5 TEM images of MFe_2O_4 MNPs synthesized from the thermal decomposition of metal acetylacetonate (acac) precursors. The size and the standard deviation (nm) are indicated on the images. (A - C) Cobalt ferrite MNPs with diameters of 9, 12, and 14 nm. (D - F) Manganese ferrite MNPs with diameters 7, 11, and 26 nm [1]. Scale bar = 20 nm.

rate and the reaction temperature to investigate their effects on the average diameter and size distribution of the MNP ensemble.

$CoFe_2O_4$ and $MnFe_2O_4$ MNPs 8.9 nm and 7.4 nm in diameter were initially synthesized using the method developed by Sun et al. (**Figure 4.5A** and **D**) [50]. To create MNPs with diameters greater than 10 nm, we modified the synthesis by replacing $Mn(acac)_2$ and $Co(acac)_2$ with the chloride salts $MnCl_2$ and $CoCl_2$ and directly heated the reaction solution to reflux at a rate of 3.3 °C/min (**Figure 4.5B** and **E**). The original synthesis requires the reaction to be set at 200 °C for 2 hours prior to raising the temperature to reflux to promote nuclei formation and homogeneous decomposition of both metallic sources to achieve monodispersity. However, the increased number of nuclei formed during this prolonged nucleation period can reduce the final size of the MNPs during the growth phase. Because $Fe(acac)_3$ decomposes at a different temperature compared to $Mn(acac)_2$ and $Co(acac)_2$ [76], we introduced Mn^{2+} or Co^{2+} sources from chloride salts, which can be directly incorporated as $Fe(acac)_3$ decomposes. This approach was similarly adopted for homogeneous doping of core-shell iron oxide nanoparticles composed of magnetically soft cores and magnetically hard shells or vice versa [77]. With these modifications, $CoFe_2O_4$ and $MnFe_2O_4$ MNPs with diameters 11.7 nm and 11.3 nm respectively were synthesized.

Because the magnetocrystalline anisotropy of $MnFe_2O_4$ is an order of magnitude lower than Fe_3O_4, nanoparticles larger than 20 nm are required to observe appreciable heating at AMF with amplitude 15 kA m^{-1} and frequency 500 kHz (**Figure 3.3**). Replacing dibenzyl ether (DBE) with a higher boiling point solvent such as ODE yielded MNPs 14 nm in size but was found to be polydisperse [78]. Monodisperse 16 nm particles were synthesized when a higher molar ratio of ligand to solvent was used in dioctyl ether (DOE) [79]. However, increasing the temperature in different solvents was found to be insufficient to increase the MNP size above 20 nm due to the excess ligands required with the highly reactive Fe(acac)$_3$ source. Consequently, a seed-mediated protocol was developed. By directly heating the reaction to reflux and bypassing the 2 hour nucleation step, a 5 to 7 nm shell can be grown [80]. Using this seed-mediated approach, we have synthesized 14.3 nm $CoFe_2O_4$ and 26.3 nm $MnFe_2O_4$ MNPs (**Figure 4.4C** and **F**).

4.7 Comparison between Synthetic Methods

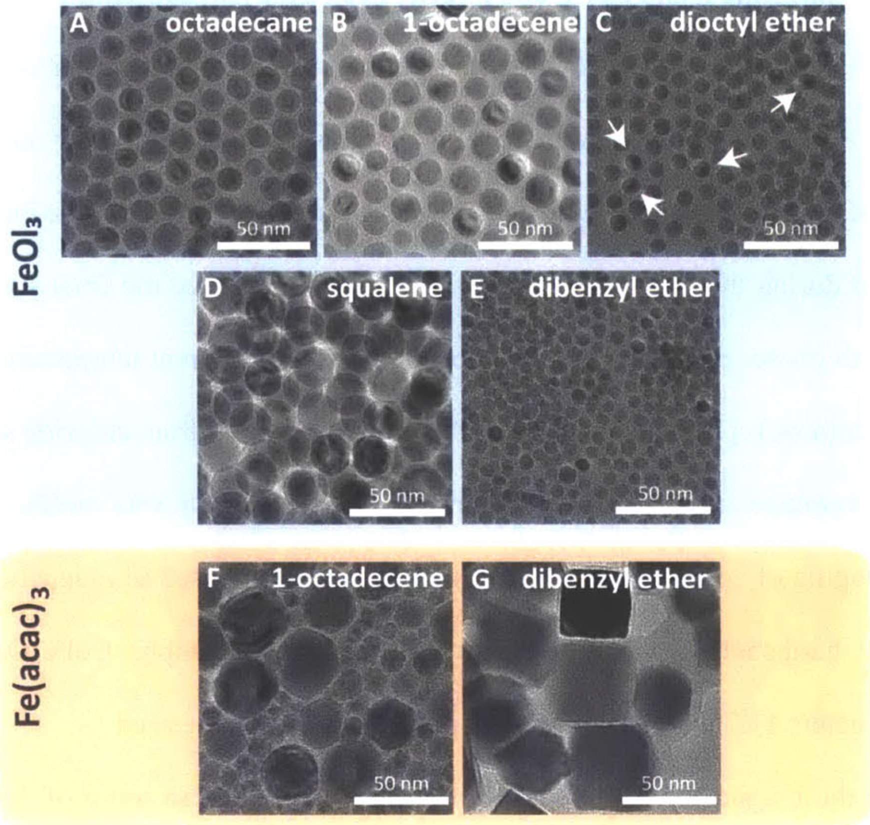

Figure 4.6 Solvent influences phases found in iron oxide nanoparticles. Transmission electron micrographs of ferrite nanoparticles synthesized from FeOl$_3$ decomposition in (A) octadecane (B) 1-octadecene (C) dioctyl ether (D) squalene and (E) dibenzyl ether. Arrows in (C) point to nanoparticles with clear core-shell morphology. TEM images of Fe(acac)$_3$ decomposition in (F) 1-octadecene and (G) dibenzyl ether. FeOl$_3$ with higher activation energy than Fe(acac)$_3$ produces monodisperse nanoparticles (blue) compared to polydisperse samples (red) [2].

To identify the variability in nanoparticle morphology presented in Section 4.5 and 4.6 and in pursuit of a one-pot reaction of phase-pure magnetite in the 20-30 nm range, we systematically decomposed the two precursors, $FeOl_3$ and $Fe(acac)_3$, in octadecane, ODE, squalene (SQE), DOE, and DBE. Heterogeneous contrast from high-resolution transmission electron (HRTEM) micrographs revealed core-shell architecture for nanoparticles produced from $FeOl_3$ in all solvents except in DBE (**Figure 4.6A-E**). $Fe(acac)_3$ pyrolysis similarly produced core-shell nanoparticles in ODE but not in DBE with broader size distribution (**Figure 4.6F, G**). In comparison to $Fe(acac)_3$, which begins to decompose at ~180 °C, $FeOl_3$ possesses higher activation energies due to its long C_{18} alkyl chains. The higher decomposition temperature (>300 °C) enabled finer control over the nanoparticle size and size distribution due to the critical supersaturation levels being reached closer to the boiling points of the chosen solvents [5]. Because of the higher reactivity of $Fe(acac)_3$, excess addition of coordinating ligands such as oleylamine and 1,2-hexadecanediol must be introduced to inhibit simultaneous nucleation and growth [72]. The resulting increase in interfacial energy limits the growth of nanoparticles, typically leading to nanoparticle sizes <10 nm as seen in Section 4.6.

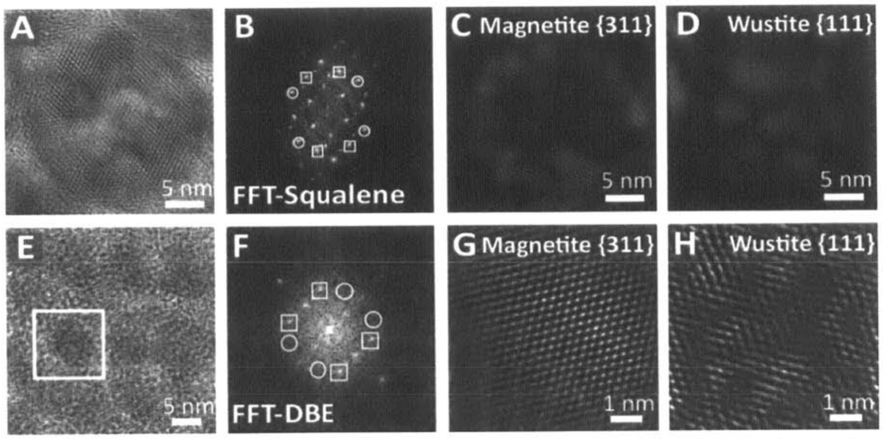

Figure 4.7 High-resolution transmission electron micrographs of individual particles synthesized in squalene and in (E) dibenzyl ether. (F, G) Fast Fourier transform of individual particles. Reconstructed images filtered from specific plane orientations for (H, I) {311} magnetite and (J,K) {111} wüstite [2].

We further mapped the phases of an individual nanoparticle synthesized in SQE using fast Fourier transform (FFT) to identify the origin of the observed core-shell morphology, which revealed a rock-salt core and an inverse spinel shell (**Figure 4.7A-D**). Although the diffraction peaks corresponding to the {111} and {311} planes from wüstite (rock-salt) and magnetite (inverse spinel) overlap due to similar interplanar spacing, the plane angle relative to the <200> direction is unique and allows for identification of the two phases as denoted by the spots marked with circles ○ ({111} wüstite, d = 0.2498 nm) and squares □ ({311} magnetite, d = 0.2534 nm) in **Figure 4.7B** and **F**. Reconstructed images filtered for the {111} reflections of wüstite showed preferential distribution within the core, while the inverse FFT from the {311} planes assigned the inverse spinel phase predominately to the shell. This morphology is consistent with an oxidation mechanism that converts metastable wüstite into magnetite at the MNP surface (**Figure 4.7C** and **D**) [81]. By contrast, single-crystalline inverse spinel 6.7±0.7 nm nanoparticles were synthesized in DBE (**Figure 4.7E-H**). While inverse spinel magnetite is favored for its ferrimagnetic properties, existing methods can only produce single-phase nanoparticles <10 nm. Nanoparticles >10 nm in diameter typically contain magnetite and the additional wüstite phase. In Section 4.8 and 4.9, a solvent redox mechanism is developed to synthesize highly-crystalline magnetite. Chapter 5 will examine the differences in structural and magnetic properties between the core-shell and single phase systems in more detail.

4.8 Solvent Redox Mechanisms Dictates Nanoparticle Phases

Comparison of the two syntheses presented in Section 4.7 led us to hypothesize that the role of the solvent can determine the phases found within the nanoparticles. Rock-salt wüstite (Fe_xO_{1-x}) contains primarily reduced Fe^{2+} while inverse spinel magnetite is mixed valent $Fe^{2+/3+}$ (Fe_3O_4). Examination of the chemical structure of the solvents revealed potential redox activity,

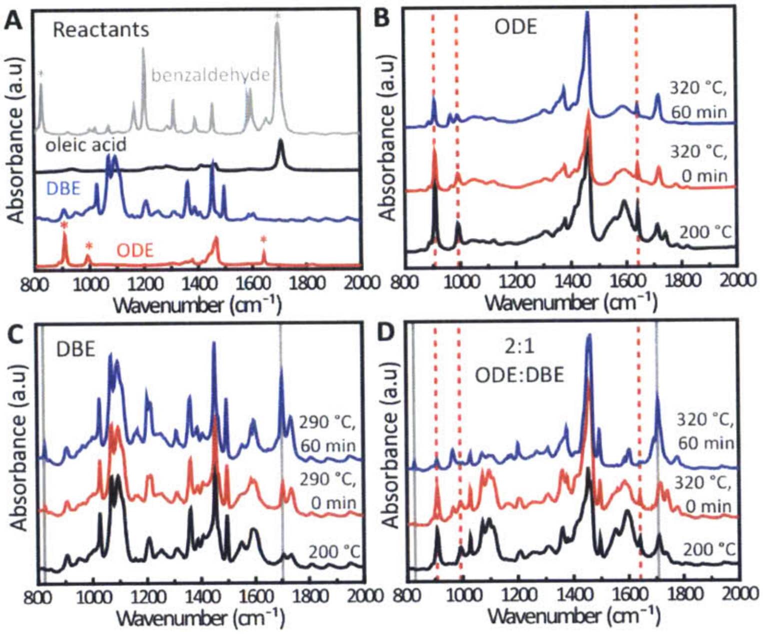

Figure 4.8 Solvent redox mechanism of ferrimagnetic nanoparticles with tunable size. (A) FTIR absorbance spectroscopy of pure reactants with the aldehyde of benzaldehyde (grey *) and vinyl double bond of ODE (red *) starred. Evolution of reaction at 200 °C, at reflux, and at 1 hr of refluxing for $FeOl_3$ decomposed in (B) ODE, (C) DBE, and (D) 2:1 volume ratio of ODE:DBE. The absorption peak positions of the double bond of ODE (red dashed line) and of the aldehyde of benzaldehyde (grey solid line) are marked [2].

which can dictate the electrochemical potential of the solution to bias between reduced and oxidized forms of iron oxide. We selected the solvents ODE and SQE to examine the reductive tendencies of unsaturated bonds in alkene hydrocarbons [44, 82]. The aromatic ether DBE was investigated for potential oxidative effects, since its decomposition can generate intermediate radical products [83]. While the valence state of iron exists only in the 3+ state in the precursor [73], production of CO_2 during $FeOl_3$ decomposition was reported to be sufficient to reduce Fe^{3+} to Fe^{2+} [75]. Recent studies have also demonstrated that the moles of CO_2 emitted over the course of a reaction exceeded the moles of reactants by an order of magnitude, indicating that oxidation of ODE, a commonly used solvent, into CO_2 may contribute to the reduction of Fe^{3+} [84]. By performing Fourier transform infrared (FTIR) spectroscopy on the aliquots of reaction solutions at different times during the heating process (**Figure 4.8**), we found that the characteristic absorption peaks of the vinyl group (=C-H bend (909.7 and 991.2 cm^{-1}); C=C stretch (1641.4 cm^{-1})) decreased during reflux at 320 °C for 1 hour (**Figure 4.8B**), consistent with vinyl group oxidation. This observation was in line with previous reports demonstrating that alkene oxidation can reduce selenium dioxide into metallic selenium[82] and Fe^{3+} into metallic iron [44]. By contrast, DBE undergoes free radical decomposition into toluene and benzaldehyde during thermolysis (**Figure 4.8C**) [83]. New peaks associated with the characteristic vibrational frequencies of an aromatic aldehyde (C=O stretch (1700 cm^{-1}); C=O bend (827 cm^{-1}))[85] emerged during synthesis indicating formation of benzaldehyde. To confirm free-radical generation during DBE thermolysis we performed reactions in mixtures of co-solvents containing of 4:1, 2:1, and 1:1 ODE to DBE volume ratios. Progressively higher oxidation of the vinyl group in ODE was observed with increasing proportions of DBE (**Figure 4.9**). The integrated absorbance of the =C-H band at ~910 cm^{-1} after 30 minutes of reflux was normalized to the initial value at 200 °C. Elimination of up to ~60% (~13 mmol) of the vinyl groups was observed in 1:1 ODE:DBE mixture compared to just ~4% (~2 mmol) oxidized in pure ODE.

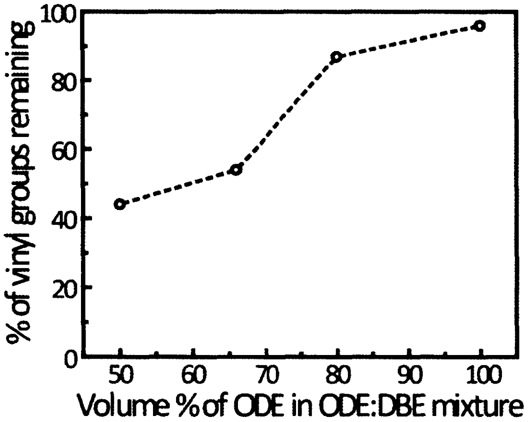

Figure 4.9 Integrated area of the vinyl peak of ODE (=C-H, 910 cm^{-1}) after 30 minutes of reflux normalized to the initial integrated area of the same peak at 200 ° C for different volume ratios of ODE:DBE with all other reaction parameters remaining the same.

4.9 Solvent optimized redox enables synthesis of nearly defect-free MNPs.

While ferrite MNPs with dimensions <10 nm are appropriate for applications in MR imaging, magnetic hyperthermia demands larger nanoparticles for efficient heat dissipation. According to dynamic hysteresis modeling presented in Chapter 3, the loss power is maximized for ferrite MNPs at the superparamagnetic to ferromagnetic transition for low alternating magnetic field amplitudes, and in the ferromagnetic regime for higher amplitudes. This transition corresponds to iron oxide MNPs 20-30 nm in size that are approximately spherical for alternating magnetic field frequencies *f* on the order of hundreds of kilohertz [6]. To fully decompose $FeOl_3$ and grow the MNPs to this size range, reaction temperatures exceeding 300 °C must be attained as demonstrated in Section 4.5 [73]. Pure DBE provides an in-situ oxidation mechanism that prevents wüstite formation, but its low reflux temperature of 290 °C sets an upper limit of ~7 nm on MNP dimensions in the conditions tested.

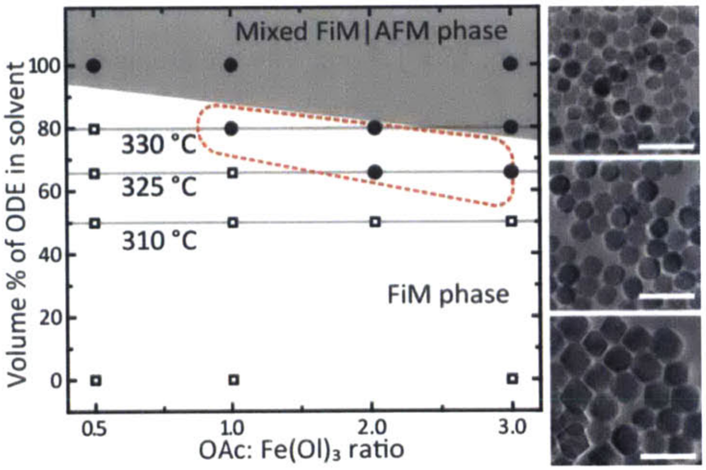

Figure 4.10 Reaction space as a function of volume percentage of ODE in a co-solvent of ODE and DBE and oleic acid (OAc):$FeOl_3$ ratio. Nanoparticle size <15 nm in diameter are denoted as □ and • for diameters >15 nm. Optimal size range (15-30 nm) of ferrimagnetic nanoparticles is circled with the red dashed line. Transmission electron microscopy images of nanoparticles synthesized in a 2:1 volume ratio of ODE to DBE with an OAc:$FeOl_3$ molar ratio of 1:1, 2:1, and 3:1 resulting in particle diameters of (Top to bottom) 15 ± 1.5 nm, 19 ± 1.8 nm, and 27 ± 1.9 nm [2].

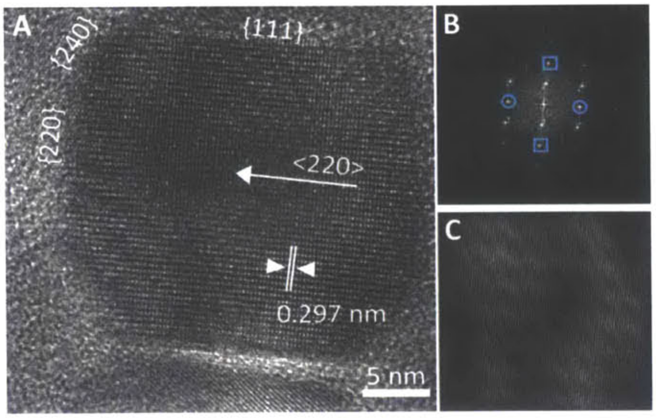

Figure 4.11 (A) High-resolution transmission micrograph of single nanoparticle synthesized by SORT. (B) Fast Fourier transform of the single particle image with the {111} and {220} marked ○ and □ respectively. (C) Reconstructed image exhibiting single-crystalline, inverse spinel nanoparticles free of the wüstite phase [2].

We relied on solvent optimized redox tuning (SORT) to access temperatures >300 °C while selectively promoting the formation of the inverse spinel phase. We found that ODE:DBE solvent mixtures with volume ratios of 4:1 and 2:1 had reflux temperatures of 330 °C and 325 °C respectively. An ODE:DBE mixture with a volume ratio of 1:1 exhibited a reflux temperature of 310 °C, which was too low to synthesize nanoparticles >15 nm. Monodisperse ($\sigma < 10\%$) faceted ferrite MNPs with sizes of 10 ± 0.8 nm, 15 ± 1.5 nm, 19 ± 1.8 nm, and 27 ± 1.9 nm were produced using oleic acid to $FeOl_3$ ratios of 1:1, 3:2, 2:1, and 3:1 respectively in an ODE:DBE solvent mixture with a 2:1 volume ratio (**Figure 4.10**). Faceted FiM 26 ± 2.2 nm nanoparticles were also synthesized with a 2:1 volumetric ratio mixture of SQE:DBE (T=330 °C) and a molar ratio of oleic acid to $FeOl_3$ of 2:1. HRTEM of SORT nanoparticles further confirmed that only the inverse spinel phase was synthesized (**Figure 4.11**). Without the addition of DBE, only biphasic FiM/AFM nanoparticles could be synthesized. Note that the direct addition of the DBE decomposition product benzaldehyde to ODE did not assist in the oxidation process (**Figure 4.12**).

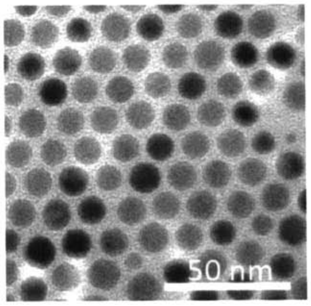

Figure 4.12 TEM image of nanoparticles synthesized in 15 mL of ODE with 10 mmol oleic acid and 10 mmol of benzaldehyde. Without the addition of DBE, the nanoparticles have core-shell morphology characteristic of biphasic nanoparticles, demonstrating that radicals generated during decomposition of DBE into benzaldehyde is necessary for the production of nearly-defect free nanoparticles [2].

4.10 Conclusion

A comprehensive study of well-established heat-up protocols enabled guidelines to be developed for the synthesis of highly-crystalline magnetite with tunable size and composition. While Fe(acac)$_3$ decomposition in DBE produced single phase magnetite, this highly reactive precursor required excess molar concentrations of ligands to separate nucleation and growth, which inadvertently also suppressed growth. Full decomposition of FeOl$_3$ required solvent reflux temperatures to exceed 300 °C and allowed for monodisperse nanoparticles up to 30 nm to be synthesized. However, the solvents required to reach these high boiling points had reductive tendencies to generate unwanted wüstite phases. By combining high activation energy FeOl$_3$ in a co-solvent incorporating DBE, the electrochemical potential of the reaction environment was shifted to favor the formation of single-phase magnetite while reaching solvent temperatures >320 °C, which enabled tunable sizes up to 30 nm. Structural and magnetic properties of the nanoparticles will now be examined in the next chapter.

Chapter 5

Structural and Magnetic Properties of Ferrite Nanoparticles

5.1 Summary

Iron oxide can exist in three magnetic phases: fully oxidized maghemite (γ-Fe_2O_3), mixed valent $Fe^{2+/3+}$ magnetite (Fe_3O_4), and reduced metastable wüstite (Fe_xO, $x = 0.83 - 0.96$) [48, 49, 66]. In this chapter, powder x-ray diffraction and magnetization measurements were collected to identify the differences in structural and magnetic properties between the nanoparticles produced by the synthetic methods studied in Chapter 4. We found that $Fe(acac)_3$ decomposition in DBE produced non-stoichiometric magnetite ($Fe_{3-\delta}O_4$) with high saturation magnetization (M_s) approaching values of the bulk material (94 $A{\cdot}m^2/kg$) [72, 86], while synthesis from $FeOl_3$ with biphasic morphology composed of an AFM core and a FiM shell exhibited anomalous magnetic properties [44, 73, 81, 87]. Antiphase boundaries that form at the subdomain interfaces in this AFM/FiM coupled system lead to undesirable magnetic properties, including low M_s, high-field susceptibility, and exchange bias [49]. Although post-synthesis oxidation has been proposed to

---

The work described in this chapter was previously published in references [1].

yield only the FiM phase [1, 46, 88, 89], defects may persist due to limited diffusion in disordered cationic layers [49]. Annealing at high temperatures was found to be effective at removing AFM content but insufficient to remove residual defects. By contrast, the SORT chemistry detailed in Section 4.8 produced single phase magnetite without the need for post-synthesis modification and exhibited several hallmark features of a nearly defect-free system. Structural optimization and improvement in magnetic properties lead to high-performance ferrite nanoparticles for biomedical applications, which is examined in Chapter 6.

5.2 Experimental Methods

5.2.1 Structural Characterization

Powder x-ray diffraction patterns of as-synthesized nanoparticles was collected on a three-circle diffractometer coupled to a Bruker-AXS Smart Apex charged-coupled-device (CCD) detector with graphite-monochromated Mo K α radiation ($\lambda = 0.71073$ Å).

5.2.2 Magnetic Characterization

Room temperature magnetization measurements were performed with a vibrating sample magnetometer (VSM), which obtains field-dependent magnetization curves from induced voltages in a pickup coil as the sample vibrates sinusoidally in a uniformly applied field. A superconducting quantum interference device (SQUID) magnetometer was used to obtain hysteresis curves at 5 K as well as magnetization measurements as a function of temperature. SQUID magnetometers measures the magnetization of samples based on superconducting loops composed of two Josephson junctions that are sensitive to the magnetic flux of a sample is moving through the loop. The external magnetic field applied by the sample results in a screening current that is amplified until a critical current is oscillating in the loop which is a function of the applied magnetic field.

The voltage induced across the shunt resistance that is connected across the junctions can then be determined.

As-synthesized nanoparticles were sealed in quartz tubes using rubber stoppers. Hysteresis curves at 5 K were measured using a superconducting quantum interference device (SQUID, MPMS-XL, Quantum Design). Field cooled and zero field cooled magnetization measurements were performed with an applied field of 100 Oe. Room temperature hysteresis were generated on a vibrating sample magnetometer (VSM, Digital Measurement Systems Model 880A).

5.3 Structural Characterization of Ferrite Nanoparticles

Powder x-ray diffraction (XRD) was performed on the nanoparticles described in Chapter 4 to elucidate the structural differences between the synthetic methods. XRD studies of nanoparticles synthesized from $Fe(Ol)_3$ precursors confirmed the presence of both wüstite and magnetite, with the (111), (200), (220), (311), and (222) peaks associated with wüstite clearly identified for all solvents tested except for DBE (**Figure 5.1**). XRD analysis further supports the

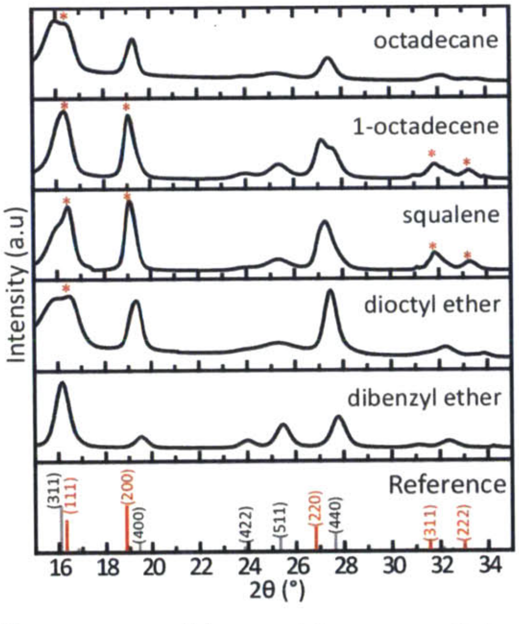

Figure 5.1 Powder x-ray diffractograms of iron oxide nanoparticles synthesized in the indicated solvents from Fe(Ol)3 decomposition using a Mo Kα source.

observation of a spinel-like phase coherently embedded in a wüstite matrix as seen by single particle HRTEM analysis in **Figure 4.7**.

Wüstite forms as an intermediary species when the solvent environment is not sufficiently oxidizing to form maghemite or magnetite phases, which is characteristic of most reactions that use solvents with boiling temperatures >300 °C [45, 73, 88]. In Section 4.8, evidence that ODE had reductive tendencies was provided. By contrast, $Fe(Ol)_3$ decomposition in DBE produced nanoparticles with no wüstite content (**Figure 5.1**). This phase difference is consistent with an in-situ oxidation mechanism of DBE proposed in Section 4.10 to favor the mixed valent Fe^{2+}/Fe^{3+} inverse spinel phase.

Because wüstite is a metastable phase, annealing the nanoparticles should relax the cation distribution into the thermodynamically stable magnetite phase [45, 90]. We found that the wüstite peaks associated with the as-synthesized state was eliminated by annealing in air at 240 °C through

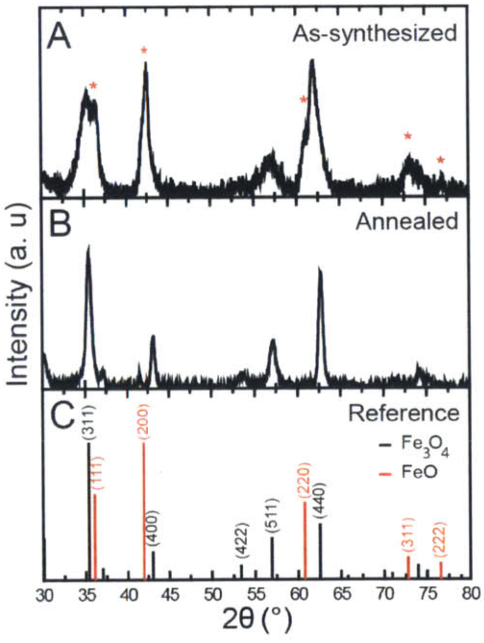

Figure 5.2 Powder x-ray diffraction patterns collected with a Cu Kα source of (A) as-synthesized iron oxide nanoparticles with the wüstite FeO phase marked with a red asterix, and (B) after annealing with high-temperature ligand exchange protocol. (C) Reference pattern of bulk Fe3O4 (black) and FeO. (red) [1].

a high temperature ligand-exchange protocol (**Figure 5.2A,B**) [91]. The high temperature phase transfer step provided an oxidizing environment that enabled the transformation of metastable wüstite into maghemite and magnetite phases with no evidence of FeO peaks apparent in the powder diffraction patterns (**Figure 5.2B**). Our data is in agreement with prior reports that observed the conversion of wüstite MNPs into Fe_3O_4 and γ-Fe_2O_4 when annealed in air at temperatures between 140 – 200 °C [45]. While annealing can remove metastable phases from the synthesized nanoparticles, this additional step was observed to have batch-to-batch inconsistencies due to heterogeneity in defect elimination and Ostwald ripening at high temperatures contributing to polydispersity in nanoparticle size [49, 89].

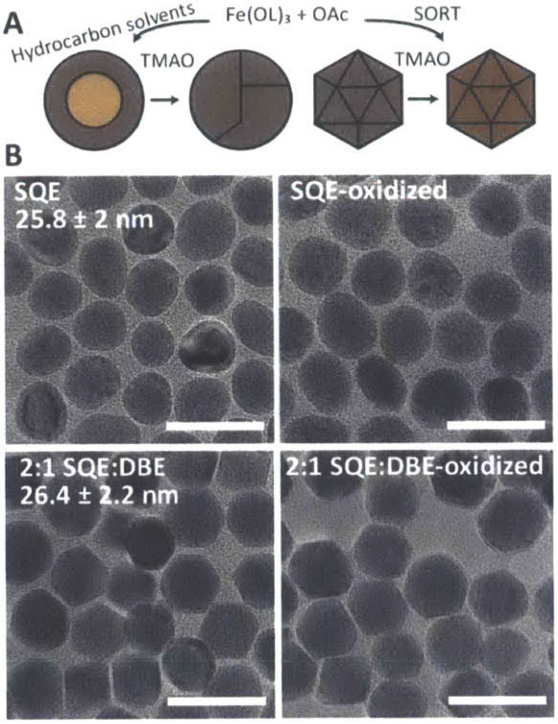

Figure 5.3 (A) Schematic illustrating the four different phase compositions synthesized. Pyrolysis in SQE leads to biphasic nanoparticles which can be oxidized with TMAO into strained single-phase Fe3-δO4. Truncated icosahedrons composed of Fe3-δO4 are synthesized by SORT and can be oxidized to γ-Fe2O3. OAc = oleic acid. (B) TEM images of similarly sized ~25 nm nanoparticles corresponding to the four chemical treatments (SQE = biphasic FeO/ Fe3-δO4, SQE-oxidized = strained Fe3-δO4, 2:1 SQE:DBE (SORT) = Fe3-δO4 , 2:1 SQE:DBE (SORT Ox) = γFe2O3). Scale bar = 50 nm.

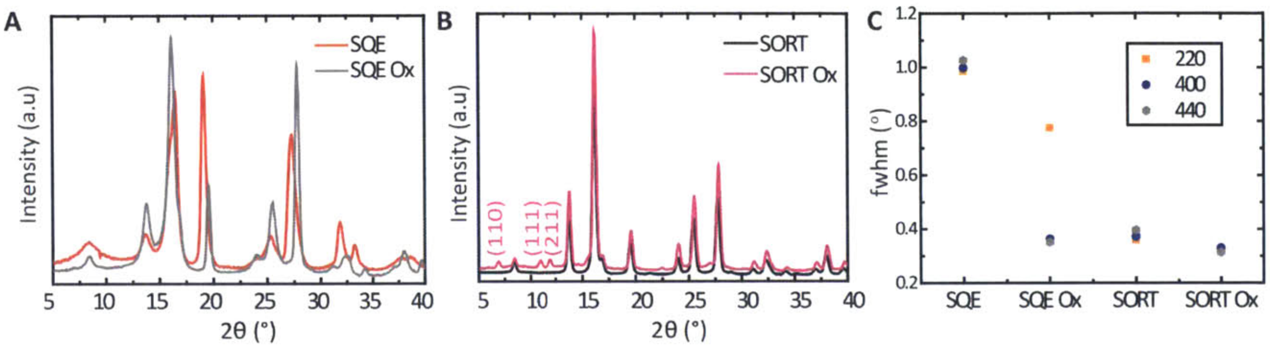

Figure 5.4 Powder x-ray diffractogram using a Mo Kα source of (A) SQE biphasic nanoparticles (red) and SQE oxidized nanoparticles containing defects (grey), and (B) as-synthesized ferrite nanoparticles that underwent SORT (black) and SORT oxidized nanoparticles (magenta). (C) Full-width at half max values of the (220) (orange), (400) (blue), and (440) (grey) diffraction peaks of the four samples.

A novel electrochemical co-solvent method (SORT) identified in Section 4.9 enabled the synthesis of single-crystalline magnetite nanoparticles with sizes >20 nm appropriate for magnetic hyperthermia. To investigate the impact of this phase engineering on the structural property of the MNPs, we compared similarly sized ~25 nm nanoparticles synthesized by SORT (co-solvent volume of 2:1SQE:DBE), with those produced in pure SQE. (**Figure 5.3A, B**). SQE was a convenient solvent choice due to its higher boiling point compared to ODE to synthesize similarly-sized nanoparticles >20 nm for the pure and co-solvent conditions tested. The effects of iron valency were assessed by applying a post-synthesis oxidation procedure to both types of particles (**Figure 5.3A, B**). XRD patterns revealed that oxidation with trimethyl amine N-oxide (TMAO) for 30 minutes at 140 °C was sufficient to anneal biphasic MNPs synthesized in SQE into inverse spinel $Fe_{3-\delta}O_4$ (**Figure 5.4A**). Application of the same oxidation treatment to SORT nanoparticles led to the conversion of $Fe_{3-\delta}O_4$ into γ-Fe_2O_3, detected as small increases (~0.2°) of higher angle peaks and the emergence of weak diffraction peaks corresponding to the (110), (111), and (211) planes (**Figure 5.4B**). To evaluate the impact of the redox processes on crystal structure, the full width at half-maximum (fwhm) values for the (220), (400), and (440) peaks associated with the inverse spinel phase were determined from line profile fits to XRD patterns for nanoparticles produced in SQE and co-solvents (SORT) prior to and following post-synthesis oxidation (**Figure 5.4C**). For biphasic nanoparticles synthesized in SQE, we observed fwhm values of ~1° for all three diffraction planes with significant reduction in line broadening for the (400) and (440) peaks following oxidation, while the (220) line was not affected to the same degree. Because both the octahedrally-coordinated iron interstitials and oxygen sublattice of the inverse spinel (400)/(440) and rock salt (200)/(220) diffraction peaks overlap, defects along these crystallographic directions can contribute to anisotropic strain broadening as observed in the biphasic nanoparticles [49, 92]. Tetrahedrally coordinated iron in the inverse spinel solely contributes to the diffraction line along the (220) direction, which should not be significantly influenced by oxidation treatment. Fwhm <0.4° was measured for all planes for MNPs produced by SORT independent of post-synthesis oxidation, suggestive of the low defect density within these nanoparticles.

In summary, XRD analysis illustrates how the electrochemical potential of the solvent environment can bias the iron oxide polymorph between metastable wüstite and thermodynamically stable magnetite. While high-temperature annealing can remove most wüstite content in biphasic nanoparticles synthesized in reducing solvents, residual defects seen in anisotropic peak broadening of the XRD peaks may have detrimental impact on the magnetic properties. An alternative method is to use SORT to synthesize phase pure magnetite nanoparticles, which are highly crystalline and nearly defect-free.

5.3 Magnetic Properties of Ferrite Nanoparticles

This subsection presents detailed magnetic characterization of the nanoparticles described in Chapter 4. We first investigated the magnetic behavior of as-synthesized nanoparticles using vibrating sample magnetometry (VSM) measured at room temperature. We find that nanoparticles synthesized from metal-oleate precursors exhibited low saturation magnetization M_s relative to the bulk material (**Table 5.1**). While low M_s values for small MNPs (<10 nm) can be attributed to the formation of a magnetically frustrated surface layer due to incomplete coordination of metal ions, this effect becomes less significant with increased size of the nanoparticle [93]. Surprisingly, MNPs synthesized with metal-oleate precursors exhibit further decrease in M_s with increased particle size. Saturation magnetization values for iron oxide MNPs fall from ~35 $\text{A}\cdot\text{m}^2/\text{kg}$ to less than 20 $\text{A}\cdot\text{m}^2/\text{kg}$ as MNP diameters increased from 5 nm to 22 nm even as spin canting effects decreased with decreased surface to volume ratios [68].

We calculated the magnetic volume, a proxy for the magnetic moment that assumes bulk saturation magnetization of the magnetized material from the obtained magnetization curves using a linear fit for static magnetic susceptibility in the low field limit [58]:

$$\chi_0 = = \frac{\mu_0 M_s^2 V}{3k_B T} \tag{5.1}$$

We find that the as-synthesized magnetic diameter of these MNPs never exceeded 10 nm despite a large physical diameter (**Table 5.1**). As the size of the MNP increased, the decreasing magnetic diameter indicated that <10% of the volume fraction of the MNP was ferrimagnetic, suggestive of the weakly magnetic wüstite content within the as-synthesized MNPs (**Table 5.1**). Similarly, the ternary metal oxides had M_s that also decreased with increasing MNP size from 54 to 31 $\text{A}\cdot\text{m}^2/\text{kg}$ for $MnFe_2O_4$ and 15 to 3 $\text{A}\cdot\text{m}^2/\text{kg}$ for $CoFe_2O_4$ MNPs.

In addition, the as-synthesized MNPs did not exhibit saturation even at high fields ($H_o = 5$ T), which is indicative of paramagnetic content (**Figure 5.5**). The inset in **Figure 5.5** details the field-dependent magnetization at low fields measured at 5 K and presents evidence of exchange-bias (H_{EB}), which not only arises in compositionally hybrid structures but also at order-disorder interphases [94]. The example hysteresis curves of as-synthesized 18 nm iron oxide and 11 nm $MnFe_2O_4$ MNPs display an H_{EB} of 104 mT and 68 mT respectively. Because the characteristic

Table 5.1 Summary of Magnetic Properties of as-synthesized and water-soluble MNPs at 300K.[a]

sample	d (nm)	d_{mag} (nm)	d^*_{mag} (nm)	M_s (300K) ($A \cdot m^2/kg$)	M^*_s (300K) ($A \cdot m^2/kg$)	$\Phi_{Ferrimagnetic}$
	11	9.2	9.1	28	70	0.65 (0.62)
Iron	**16**	8.5	13.1	18	69	0.17 (0.61)
Oxide	**18**	9.6	16.6	39	64	0.15 (0.78)
Oleate	**22**	9.8	18.8	41	65	0.08 (0.59)
	24	10.5	16.3	22	67	0.08 (0.31)
$MnFe_2O_4$	**11**	7.7	7.6	8	47	0.36 (0.35)
Oleate	**16**	10.8	10.2	13	54	0.32 (0.27)
	19	9.8	9.6	5	25	0.09 (0.133)
	28	9.0	11.4	3	31	0.03 (0.13)
$CoFe_2O_4$	**13**			15.2	30.8	
Oleate	**20**			3	7	
$MnFe_2O_4$	**7**	7.6	7.2	53	51	0.79 (0.85)
Acac	**11**	9.2	11.3	75	74	0.53 (0.82)
	26	10.9	25.3	95	92	0.07 (0.89)
$CoFe_2O_4$	**9**			39	37	
Acac	**12**			60	62	
	14			58	59	

[a]Average diameters (d) were measured from TEM. Magnetic diameters (d_{mag}) were obtained from linear fits of root temperature hysteresis curves in the low field range. *Indicates the sample was measured from annealed nanoparticles. The $\Phi_{Ferrimagnetic}$ indicates the volume fraction that is ferrimagnetic. The bracketed values indicate the volume fraction after annealing.

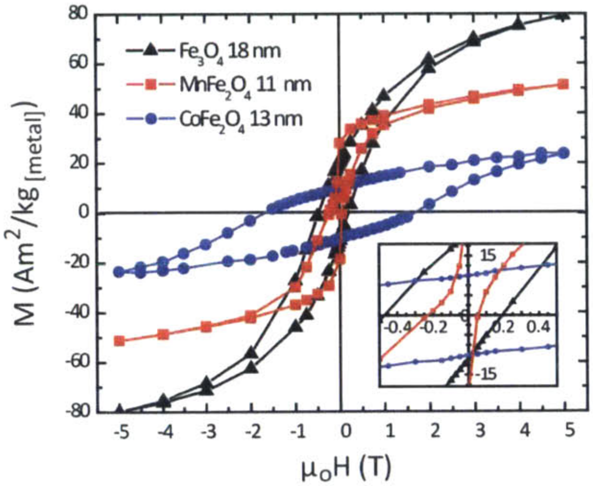

Figure 5.5 Field-dependent magnetization loops for tertiary ferries measured at 5 K. (A) As-synthesized MNPs from thermal decomposition of metal-oleate precursors. Inset: low-field region shows negative field shift characteristic of exchange bias.

length for H_{EB} is on the order of 1-2 nm nanometers [95], the observed shifts cannot be attributed to dipole-dipole interactions between particles with different magnetic phases. Levy *et al.* showed that regions of structural disorder in their iron oxide nanoparticles contributed to this effect since the moments of the magnetically frustrated phases do not fully align even at high field [50]. The observed H_{EB} in these samples, in addition to the HRTEM analysis in Section 4.7 and XRD analysis in the previous section, indicate that the ferromagnetic magnetite and antiferromagnetic wüstite phase are in intimate contact [96].

By contrast, thermal decomposition of metal acetylacetonate precursors in DBE produced monodisperse MFe_2O_4 MNPs with M_s comparable to bulk values in the as-synthesized state (**Table 5.1**). The saturation magnetization of the tertiary ferrites $CoFe_2O_4$ and $MnFe_2O_4$ MNPs increases with increasing MNP diameter reaching 63 and 95 A·m^2/kg for $CoFe_2O_4$ and $MnFe_2O_4$ respectively above 10 nm. Hysteresis loops of the 11 nm $MnFe_2O_4$ MNPs measured at 5 K indicate a low coercive field of 20 mT with no H_{EB} (**Figure 5.6**). $CoFe_2O_4$ MNPs display a markedly higher coercivity of 1.6 T with no exchange bias. A dip in M_s to 28 A·m^2/kg was measured for the 16 nm $MnFe_2O_4$ MNPs. This may be attributed to the strong reducing environment of excess oleylamine and the use of the solvent DOE instead of DBE, which was employed to increase the

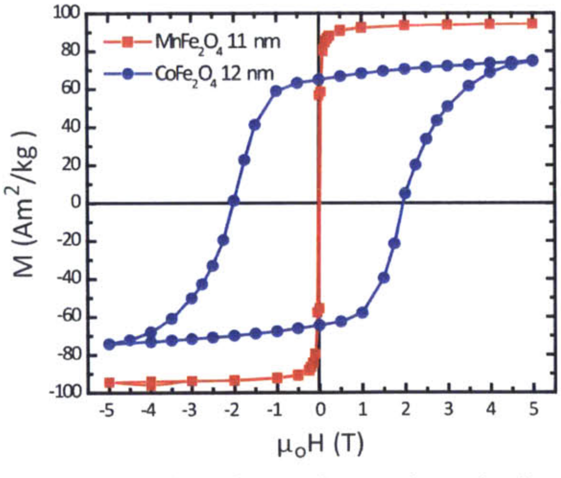

Figure 5.6 Field-dependent magnetization loops for tertiary ferries measured at 5 K for as-synthesized MNPs from thermal decomposition of metal-acac precursors.

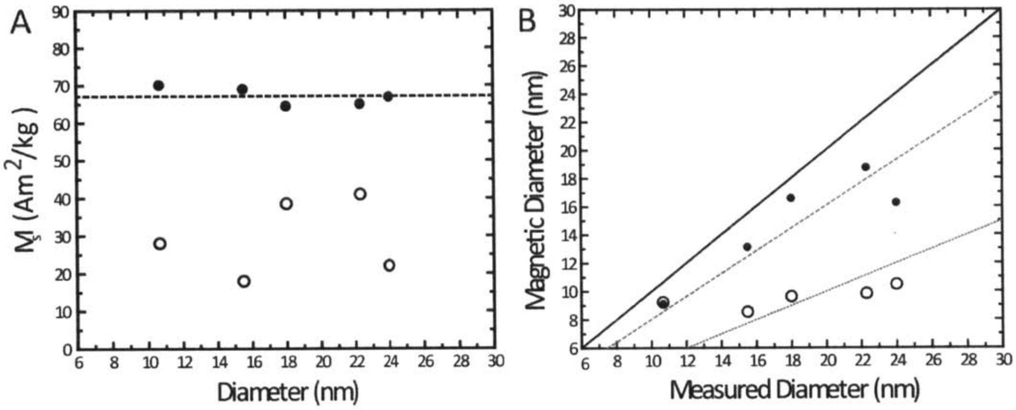

Figure 5.7 Magnetic properties of iron oxide MNPs in the as-synthesized (open circles) and annealed state (filled-in circles). (A) M_s increases after high-temperature annealing in phase-transfer step (B) Increase in magnetic diameter trending linearly with increasing MNP size. Solid black line represents 1:1 correspondence, grey dashed-lines are from linear fits to the data with intercept set at 0.

MNP diameter beyond 11 nm [45]. MNPs of $MnFe_2O_4$ with diameters of 26 nm synthesized *via* our one-step heterogeneous nucleation exhibited the highest measured M_s (95 A·m^2/kg) in the synthesized MNP set due to its increase in volume to surface area ratio.

Because wüstite is metastable, annealing the nanoparticles should enhance the magnetic properties by removing the antiferromagnetic content in favor of the ferrimagnetic phase. We found that the magnetic properties of the MNPs prepared from metal-oleate precursors was significantly improved by annealing in air at 240 °C [1, 91]. For iron oxide nanoparticles, M_s increased from 15 - 40 A·m^2/kg to an average of 67 A·m^2/kg, which is closer to bulk values of magnetite (92 A·m^2/kg, **Figure 5.7A**). The magnetic diameters were also found to correlate closely with the physical MNP diameters determined by TEM, and the ferromagnetic content of the nanoparticles exceed a volume fraction of 60% (**Figure 5.7B**, **Table 5.1**). Furthermore, the coercive field decreased from 1350 to 350 Oe and there was no observable H_{EB} (**Figure 5.8A**). These improvements in the magnetic properties can be attributed to the conversion of wüstite into the desired magnetite phase.

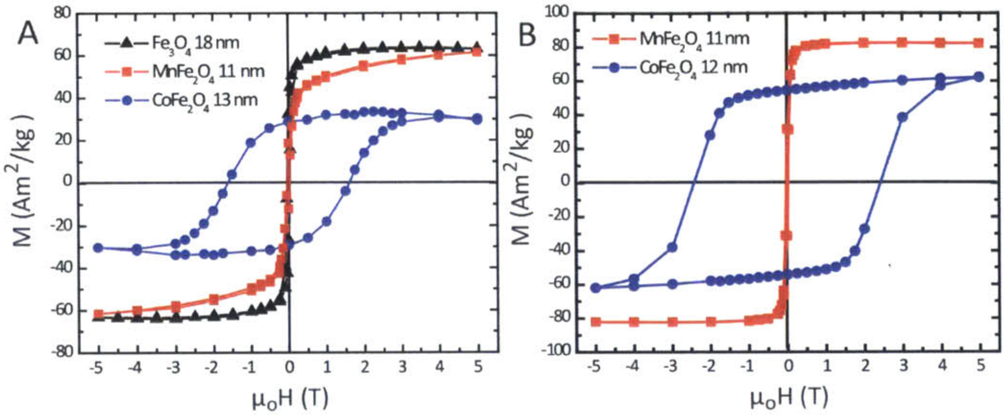

Figure 5.8 Field-dependent magnetization loops for tertiary ferries measured at 5 K for MNPs from thermal decomposition of (A) metal-oleate precursors and (B) metal-acac after annealing.

The M_s values of the $MnFe_2O_4$ and $CoFe_2O_4$ MNPs synthesized from metal-oleate precursors improved by 4-10 times after annealing. However, the low M_s still limits the MNP's application as efficient magnetothermal transducers (**Table 5.1**). The magnetic properties of the MNPs synthesized from the metal-acac precursors are preserved during the annealing phase-transfer process (**Figure 5.8B**). Furthermore, the ferromagnetic volume fraction for $MnFe_2O_4$ MNPs was found to exceed 80% (**Table 5.1**). We also find that our assumption of uniaxial anisotropy used in the dynamic hysteresis model was consistent with calculations of the remanent to saturation magnetization ratio being <0.5 from the SQUID hysteresis curves [65]. Conversely, the value calculated for $CoFe_2O_4$ MNPs was 0.84, suggestive of cubic anisotropy. The poor magnetic properties of ternary ferrites synthesized from metal-oleate precursors even after annealing necessitates alternative synthetic approaches to be identified.

Based on the four synthetic protocols depicted in **Figure 5.3 A, B**, we collected field-cooled magnetization curves at 5 K to correlate the MNPs' structural differences presented in the previous section with their magnetic properties. Characteristic of coupled systems with FiM and AFM subdomains, exchange bias (H_{EB}) and coercivity (H_c) was present in the hysteresis loop of biphasic MNPs synthesized in SQE (**Figure 5.9A,B**) [49]. Although oxidation treatment increased

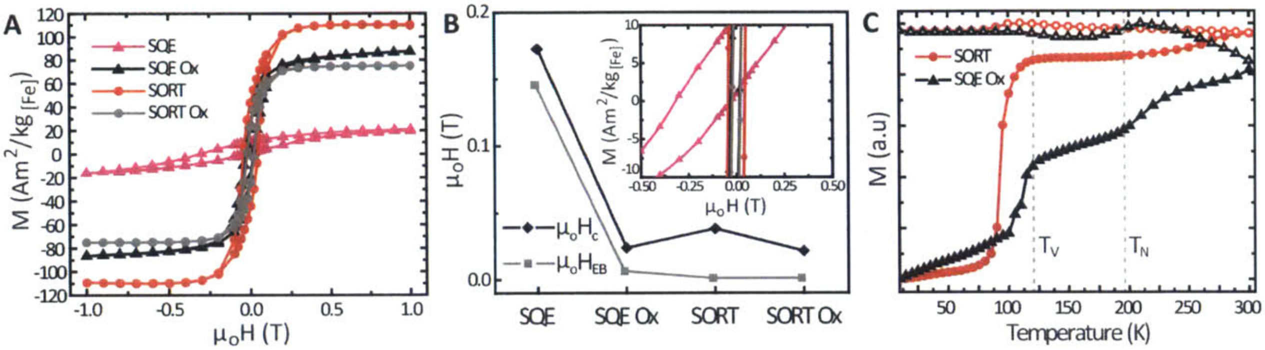

Figure 5.9 (A) Field-cooled magnetization curve measured at 5K for the four samples (SQE (pink), SQE Ox (black), SORT (red), SORT Ox (gray)). (B) Measured exchange-bias (μ_oH_{EB}) and coercive field (μ_oH_C) for the four samples calculated from the magnetization curve. (inset) low-field region of the magnetization curve in D. (C) Magnetization curve as a function of temperature for SORT (red) and SQE Ox (black) nanoparticles. Neél temperature (T_N) and the Verwey transition temperature (T_v) are marked with the grey dashed line.

the M_s from ~20 to 87 A·m^2/kg$_{[Fe]}$, residual H_{EB} of ~60 mT and high-field susceptibility persisted in these materials, and may be due to the presence of antiphase boundaries and other structural defects that cannot be eliminated due to insufficient cation diffusion during oxidation. By contrast, we found that ferrite nanoparticles synthesized in co-solvent mixtures exhibited M_s (110 A·m^2/kg$_{[Fe]}$) values approaching those of bulk magnetite (128 A·m^2/kg$_{[Fe]}$) and H_{EB}=0 (**Figure 5.9A,B**). Post-synthesis oxidation of nanoparticles produced by SORT into γ-Fe_2O_3 resulted in a decrease in M_s to 75 A·m^2/kg$_{[Fe]}$. Temperature-dependent magnetization curves of SORT-synthesized MNPs exhibited a sharp increase in magnetization near its Verwey temperature (T_V = 123 K), characteristic of $F_{e3\text{-}\delta}O_4$ as it undergoes a metal-to-insulator transition (**Figure 5.9C**) [97]. Oxidized $Fe_{3\text{-}\delta}O_4$ nanoparticles synthesized in pure SQE exhibited a suppressed Verwey transition [84], indicative of potential short-range cation disorder impeding this charge-ordering phenomenon [49, 98]. Furthermore, an increase in magnetization above the Neél temperature (T_N = 192 K) of wüstite suggested that the AFM phase could not be completely eliminated by oxidation.

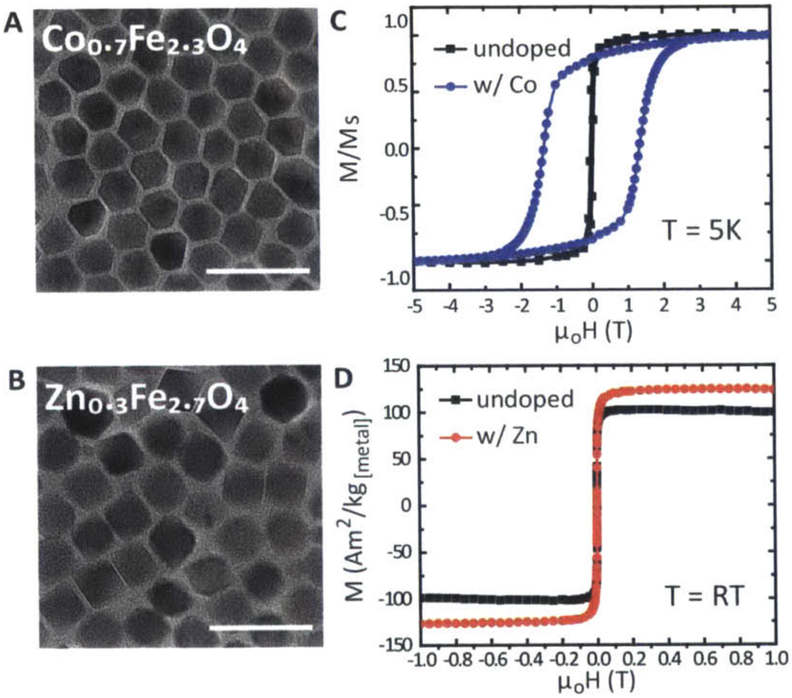

Figure 5.10 Doped ferrites with tunable magnetic properties. Transmission electron microscopy of (A) cobalt-doped ferrite MNPs and (B) zinc-doped ferrite MNPs. Degree of dopant incorporation was measured by ICP-AES and is indicated on the image. Scale bar = 50 nm. (C) Normalized magnetization curve measured for cobalt-doped MNPs in (A) at 5K exhibiting nearly 40 fold increase in the coercive field H_c compared to undoped iron oxide of the same size. (D) Room-temperature magnetization curve of zinc-doped MNPs in (B) showing increased saturation magnetization M_s compared to undoped iron oxide of the same size.

The SORT method further enabled the synthesis of highly-crystalline ternary ferrite nanoparticles, which allowed for tunability of the MNP's magnetic properties in a single reaction. As we and others have observed, tertiary ferrites synthesized via standard metal-oleate decomposition in alkene hydrocarbons exhibit phase inhomogeneity manifested by the presence of H_{EB} and low M_s [71, 99, 100], which cannot be fully eliminated by post-synthesis oxidation [1]. We find that introduction of cobalt and zinc during SORT synthesis yielded 40-fold increase in H_c and 25% increase in M_s respectively, indicative of proper substitution and homogeneous distribution of dopants within the nanoparticles (**Figure 5.10**).

The ability to tune the electrochemical potential of the solvent environment, presented in Chapter 4, is a versatile strategy for selective phase control in colloidal synthesis. While solvents and surface ligands containing double bonds have been described as effective reducing agents during production of metallic and semiconducting nanoparticles [44, 82], in-situ oxidizers for valency control of metal oxides remain poorly characterized. Free radical generation during thermolysis of aromatic ethers provides an electrochemical approach to ensure batch-to-batch consistency of structural and magnetic properties in ferrite MNPs, and may enhance their performance as MRI contrast agents and magnetothermal transducers, which is examined in Chapter 6.

Chapter 6

Water-soluble Ferrite Nanoparticles with Enhanced Biomedical Performance

6.1 Summary

While high temperature thermolysis of organometallic precursors can produce monodisperse nanocrystals with controllable shape and size, the nanoparticles are coated with hydrophobic ligands and need to be rendered hydrophilic for biological applications. This chapter explores both ligand exchange and encapsulation methods for dispersing hydrophobic nanoparticles in aqueous media. We further examine the hyperthermic performance of these water-soluble ferrite nanoparticles and correlate the measured trends to the dynamic hysteresis model presented in Chapter 3. The transverse relaxivity of the nanoparticles was also quantified. Consistent with the structural and magnetic properties of the MNPs presented in Chapter 5, we observed nearly 500% improvement in both the transverse relaxivities and specific loss powers of our optimized iron oxide nanoparticles synthesized by SORT, which has important implications in

---

The work described in this chapter was previously published in references [1]. SLP measurements were conducted with custom apparatuses developed by Michael Christiansen.

enhancing their biomedical performance as magnetic resonance contrast agents and as magnetothermal transducers.

6.2 Surface Chemistry for Water Soluble Nanoparticles

Nanoparticles synthesized by thermal decomposition are usually hydrophobic and require post-synthesis processing to become hydrophilic for general biomedical use. Water solubilization protocols typically utilize ligand exchange, which displaces hydrophobic ligands by combining the nanocrystals dispersed in a nonpolar solvent such as hexane with excess hydrophilic ligands in a miscible polar solvent at room temperature [101]. Vigorous mechanical agitation over a period of time is then expected to displace the hydrophobic coating with the hydrophilic ligand. Frequently, the first ligand exchange step is insufficient and requires repeating the phase transfer protocol in solvents with increasing polarity to promote sufficient adsorption of hydrophilic ligands to render the nanoparticles water-soluble. Furthermore, if the ligand has a low binding energy to the nanoparticle's surface, irreversible desorption may lead to nanoparticle aggregation and sedimentation over several hours to days [102].

Another method is to solubilize nanoparticles via encapsulation with amphiphilic ligands. Phase transfer is readily achieved since the amphiphile will contain both hydrophobic hydrocarbon chains that can interdigitate with the hydrophobic coating of the nanocrystals and hydrophilic groups that can form hydrogen bonds with water. The disadvantage of this method is that several nanocrystals can become encapsulated together during micellization [103], which can influence the magnetization process in an alternating magnetic field and lead to deviations from trends predicted by dynamic hysteresis modeling. The labile nature of the amphiphilic ligand to form micelles only above a critical surfactant concentration is an additional concern for colloidal stability.

While a number of these protocols exist to solubilize hydrophobic nanoparticles in water, application for neuromodulation requires additional considerations. First, because the attractive forces between MNPs scale proportionally to the size of the nanoparticles, colloidal stability for MNPs >20 nm becomes difficult to ensure due to attraction between magnetic dipoles. Second, the surface chemistry needs to minimize cytotoxic effects *in vitro* and *in vivo* in order to enable chronic stimulation in the deep brain. Finally, because of exponential temperature decay from the surface of the nanoparticle [104], compact coatings to minimize hydrodynamic radius is desired.

6.3 Experimental Methods

6.3.1 High-temperature ligand exchange.

The as-synthesized MNPs were transferred into water using a protocol adopted from Zhang et al. [105] 0.5 g of poly(acrylic acid) (Mw ~ 1800) was dissolved in 10 mL diethylene glycol and heated to 110 °C under nitrogen. 1 mL of MNPs dispersed in hexane (~50 mg/mL) was injected into the mixture and then heated to reflux at 240 °C for 3 hours. The sample was precipitated with 10 mL of 1 M HCl then washed twice with water. 50 mM NaOH solution was added to disperse the MNPs and sonicated for 30 minutes.

6.3.2 Poly(acrylic acid)-MNP conjugation to poly(ethylene glycol).

Poly(acrylic acid)-coated MNPs dispersed in water were activated with N- hydroxysuccinimide (NHS)/1-Ethyl-3-[3-dimethylaminopropyl]carbodiimide hydrochloride (EDC) for 30 minutes at pH 5.6 (1 mg of MNPs in 1 mL 10 mM NHS, 10 mM EDC). Then 5 mg of monofunctional amine-terminated poly(ethylene glycol) (MW 5000; Laysan) dissolved in 1 mL of 10 mM NHS/EDC at pH 8.6 was added and mechanically agitated for 8-12 hours. Hydrodynamic radius after conjugation was determined using dynamic light scattering at concentrations of 100 μg/mL in water, phosphate buffer saline (PBS), and cell culture media (DMEM + 10% FBS). Electron micrographs were taken with a transmission electron microscope at 200 kV. The poly(ethylene glycol)-MNP was dispersed in Tyrode's solution prior to *in vitro* and *in vivo* testing.

6.3.3 Synthesis of poly(ethylene glycol) grafted to poly(maleic anhydride-alt-1-octadecene).

Poly(maleic anhydride-alt-1-octadecene) was combined with methoxy-PEG (Mw=5000) in a 1:30 molar ratio with trace sulfuric acid and refluxed for 48 hours in chloroform under N_2. The polymer was precipitated and washed twice with hexane then dried in a desiccator for further use.

6.3.4 Encapsulation with amphiphilic PEG-grafted polymer.

100 μL of nanoparticle solution dispersed in chloroform (~10 mg/mL) was combined with 1 mL of poly(ethylene glycol) grafted poly(maleic anhydride-alt-1-octadecene) solution (10 mg/mL in chloroform) and sonicated for 15 minutes. After evaporating the chloroform under vacuum, 2 mL of 1X Tris/Borate/EDTA buffer was added and sonicated for 30 minutes. The nanoparticles were magnetic separated and washed twice with water, then reconstituted in 1 mL of water (~1 mg/mL) and sonicated for 10 minutes.

6.3.5 Cytotoxicity assay.

Colorimetric MTT (3-(4,5-dimethylthiazol-2-yl)-2,5-diphenyltetrazolium bromide) assays were performed in 96 well plates where MNPs of various concentrations (1-100 μg/mL) were added to each well seeded with HEK293FT 24 hours prior. After each time interval, 20 μL of MTT (5mg/mL in PBS) was incubated for 3 hours. Then the supernatant was aspirated and 200 μL of dimethyl sulfoxide (DMSO) was added. Each 200 μL sample in DMSO was spun down to remove

MNPs in solution and the supernatant was read with a 96 well plate reader for absorbance at 550 nm.

6.3.6 Elemental analysis.

Inductively coupled plasma atomic emission spectroscopy (ICP-AES) was used to determine the concentration of the transition metal ions on a Horiba ACTIVA-S. To remove residual ligands that may interfere with the degradation of MNPs in aqua regia, we annealed the samples in air at 400 °C for 4 hours. Organic ligands are expected to be fully decomposed above 350 °C. The amount of magnetic material in a given volume of 100 μL was determined by ICP-AES after annealing then digesting in a solution of aqua regia (1:3 v/v 37 wt % HCl to 70 wt % HNO_3) overnight at 60 °C. The quantity of metal determined was used to normalize all magnetization and SLP values that were experimentally obtained.

6.3.7 Stability Test.

0.1 mg of MNPs as determined by [Fe] content was dispersed in either 1X Tris base, acetic acid and EDTA (TAE), HEPES, or 1X phosphate buffer saline (PBS) buffer for one month and its hydrodynamic diameter was compared to the same MNPs dispersed in MilliQ water using dynamic light scattering (DLS, Malvern Nano ZS90).

6.3.8 Specific loss power measurements.

Calorimetry measurements in the presence of an AMF were conducted with a custom built setup. A toroid composed of a soft ferromagnetic material optimized for high frequency power transformers was specially machined to include a gap large enough to accommodate a sample vial and used as a coil core. A transformer circuit with a resistive ballast in the primary circuit was used to generate high, reasonably stable currents in the secondary while simultaneously matching the impedance of the variable frequency 200W amplifier (1020L, Electronics & Innovation). In the secondary, the coil acted as the resistive and inductive elements of an RLC resonance circuit, with a high voltage series capacitor setting the resonant frequency. The field magnitude was measured by a custom built probe employing a pickup loop and an oscilloscope (TDS2022C, Tektronix). Error bars placed on the field value result primarily from the moderate heating of the core over the course of 30 seconds, which was mitigated by a simple cooling system circulating ice water to the coil *via* silicone tubing.

Temperature measurements made by an AMF insensitive fiber optic temperature probe were recorded as an AMF was applied for 30 seconds. Each measurement was repeated 8 times and control samples containing only water were measured after every 4 trials to determine the background heating rate. All samples were 1 mL with a MNP concentration of approximately 2 mg/mL. The SLP value measured was normalized to the metal content determined by elemental analysis.

6.3.9 Magnetic Resonance Imaging.

MRI experiments were performed on a 7 T PharmaScan® MRI instrument (Bruker). The relaxivity of the samples were determined by using the MSME (multi-slice multi-echo) sequence at room temperature with the following: TR (repetition time) = 2 s, 30 echoes with 24 ms TE (echo time) averaged over 4 acquisitions, FOV (field of view) = 5x5 cm, matrix = 256x256, and section thickness = 2 mm.

6.4 Biocompatible MNPs with Improved Colloidal Stability

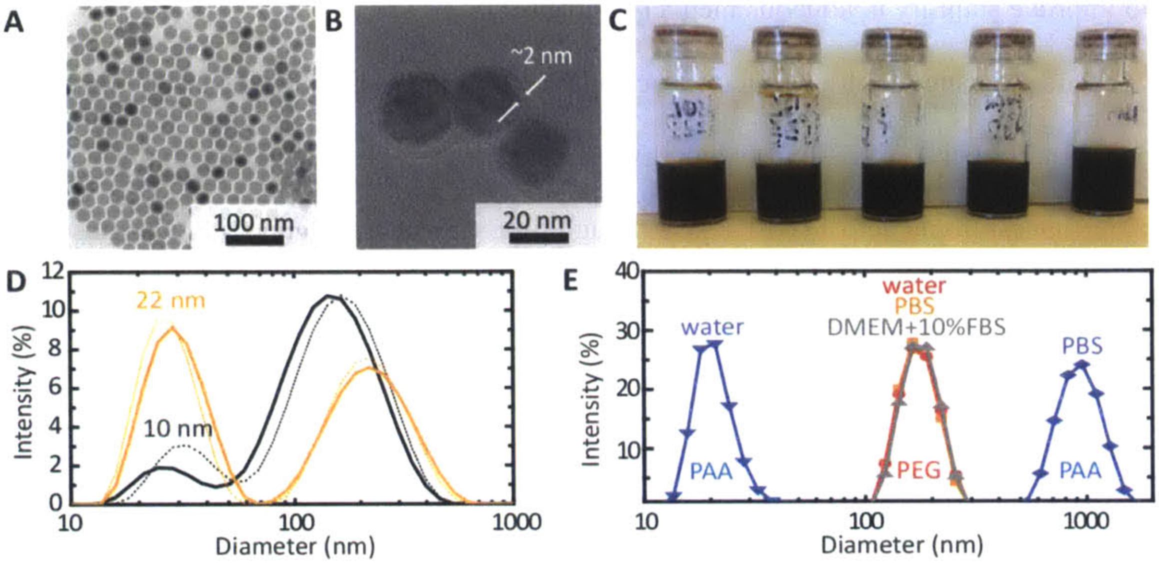

Figure 6.1 Transmission electron micrographs of (A) as-synthesized MNPs (B) and after surface modification with a 2 nm poly(ethylene glycol) (PEG) shell. (C) Photograph of PAA-coated iron oxide MNPs solutions in water after > 6 months following phase transfer procedure. MNP diameters from left to right: 11 nm, 16 nm, 18 nm, 22 nm, and 24 nm. (D) Dynamic light scattering (DLS) plots of intensity % vs. size of 10 nm (black) and 22 nm (orange) iron oxide nanoparticles in water (solid line) and in TAE (dashed line) after 1 month. No significant change in the hydrodynamic radius was observed. (E) Size distribution plot for poly(acrylic acid) (PAA) and PEG coated MNPs observed by dynamic light scattering. Aggregation in physiological fluids is observed for PAA coated MNPs but not for PEG coated MNPs

To increase adsorption kinetics using ligand exchange, we adopted a high-temperature phase transfer protocol developed by Zhang et al. which allowed us to simultaneously improve the magnetic properties of the as-synthesized core-shell MNPs through annealing and introduce polyelectrolytes to the nanoparticle's surface [105]. We used diethylene glycol, which is a high boiling point polar solvent miscible with organic solvents such as toluene, to drive the coordination of the dissolved polyelectrolytes onto the surface of the nanocrystals at temperatures greater than 200 °C. This strategy is advantageous because the high temperature accelerates the exchange of the original surfactant with the polyelectrolyte through mass action. Furthermore, the multiple binding sites of the polyelectrolyte prevents desorption as well as increased ionic interactions with water to improve stability in aqueous media (**Figure 6.1**).

Ligand exchange with poly(acrylic acid) (PAA) resulted in the MNPs to be highly stable in Good's buffers such as tris(hydroxymethyl)aminomethane (Tris) and (4-(2-hydroxyethyl)-1-piperazineethanesulfonic acid) (HEPES), although time-dependent aggregation was observed in phosphate buffered saline (PBS) which has been attributed to the formation of salt bridges (**Figure 6.1 C-E**) [91]. We observed nanoparticle aggregates with hydrodynamic radius >100 nm (**Figure 6.1D)**, which may arise from multidentate PAA bridging two or more nanoparticles.

Carboxylic acid groups on PAA-coated MNPs can be conjugated to primary amines through carbodiimide chemistry to introduce further functionality. We conjugated monofunctional amine-terminated poly(ethylene glycol) (PEG) (M_w=5000) to sterically-stabilize nanoparticles in aqueous media. By eliminating ionic interactions, PEG conjugated nanoparticles became colloidally stable in PBS as well as cell culture media containing serum without the larger aggregations seen with PAA coatings (**Figure 6.1E**).

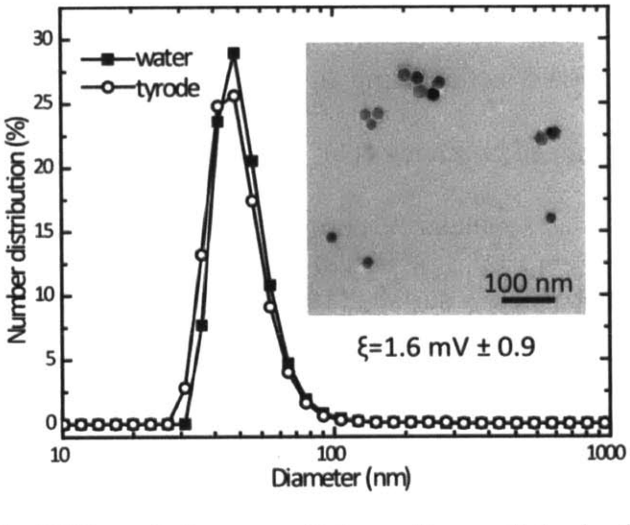

Figure 6.2 Water-soluble PEG-coated nanoparticles with small hydrodynamic radius. Number distribution of the hydrodynamic diameter of 25 nm SORT nanoparticles dispersed in water and in physiological buffer (Tyrode's solution) measured by dynamic light scattering. (inset) TEM image of PEG-coated nanopartices. Zeta-potential measurements (ξ) indicates charge neutrality.

Because SORT nanoparticles exhibit superior magnetic properties without the need for post-synthesis annealing, we adopted a rapid and facile method to render these nanoparticles water-soluble. Multiple hydrophobic subunits on amphiphilic polymer can enhance binding affinity to hydrocarbon coated nanoparticles compared to single unit amphiphiles. We utilized a room temperature ligand encapsulation protocol to intercalate amphiphilic poly(maleic anhydride-alt-1-octadecene) modified with PEG (PMAO-PEG) with the surface oleates to make the nanoparticles water-soluble [106]. The maleic anhydride group in the polymer is susceptible to nucleophilic attack, enabling surface modification through condensation reactions with ligands carrying primary amines or through acid-catalyzed hydrolysis with alcohols [106]. 25 nm nanoparticles passivated with PMAO-PEG were colloidally stable at physiological conditions with a charge neutral surface (**Figure 6.2**). Polymer encapsulation is a single-step method to improve colloidal stability of large (20-30 nm) magnetic nanoparticles in physiological fluids, and is faster and less cumbersome than the multistep protocol previously developed with ligand exchange.

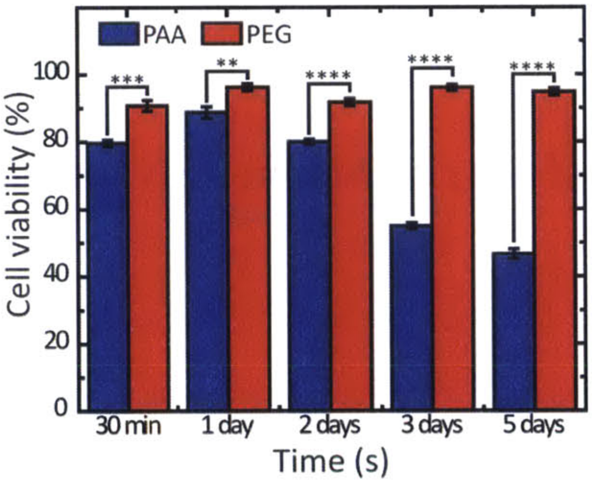

Figure 6.3 MTT colorimetric assay for measuring cell viability as a function of time. PEG coated MNPs had minimal cytotoxic effects on cell viability as compared to PAA coated MNPs (unpaired t-test, ** P < 0.01, **** P < 0.0001). PEG chains above 3000 MW can decrease non-specific protein and cell interaction, reducing agglomeration and interaction with macrophages in physiological conditions. Concentration of nanoparticles used was 100 µg/mL [Fe].

PEGylataion of MNPs prevents protein adsorption and cellular uptake [107], which can improve their biocompatibility when interfaced with cells. We used the colorimetric 3-(4,5-dimethylthiazol-2-yl)-2,5-diphenyltetrazolium bromide (MTT) assay to compare the cytotoxic effect of water-soluble MNPs with different surface chemistries on cell viability. Incubation with healthy, rapidly dividing cells will exhibit high oxidoreductase activity, which will metabolize MTT into formazan, which has a purple color that can be read out with a spectrometer. Charged PAA-coated MNPs significantly disrupted the metabolic rates of human embryonic kidney cells (HEK293FT) when compared to PEGylated (PEG M_w = 5000) MNPs (**Figure 6.3**). Increased endocytosis of negatively-charged MNPs is expected to impact cell viability in comparison to MNPs with neutral charge and reduced protein adsorption [108]. While grafting PEG onto nanoparticles can improve colloidal stability and biocompatibility, increased hydrodynamic diameter from <30 nm for PAA to >60 nm with PEGylation can hinder targeted heat transfer to the cell membrane. Alternative strategies not explored in this thesis, such as zwitterionic polymers and ligands [107, 109], may enable biocompatible coatings of MNPs with smaller hydrodynamic radiu0s.

6.5 Loss Powers of Ferrite Magnetic Nanoparticles

Hyperthermic performance, quantified as specific loss power (SLP), was assessed by exposing the water-soluble MNPs to an alternating magnetic field (AMF) and recording the temperature change as a function of time. The SLP can be calculated from the temperature increase with time using the expression:

$$SLP = \frac{C}{m}\frac{dT}{dt} \tag{5.1}$$

where C is the specific heat capacity of water per unit volume ($C = 4.184$ J K^{-1} mL^{-1}), m is the concentration (g/mL of the ferrofluid by metal content), and $\frac{dT}{dt}$ is the experimentally measured slope of the temperature increase as a function of time inside the AMF.

We first evaluated whether trends predicted by dynamic hysteresis (DH) theory could be correlated to the hysteretic losses of MNPs with anisotropy energies varied over three orders of magnitude (**Figure 6.4**). At a field condition of 500 kHz and 15 kA/m, we observed qualitative agreement between simulated and empirically measured results [1]. $CoFe_2O_4$ MNPs from both oleate and acac–decomposition did not exhibit significant hysteretic losses when exposed to the given AMF conditions, which is expected for highly anisotropic nanoparticles with heat dissipation derived primarily from Brownian rotation [110]. In the case of $MnFe_2O_4$ with comparatively low K_{eff} values, the low anisotropy energy barrier of MNPs <22 nm in diameter results in negligible observable hysteretic loss. Only Mn-doped MNPs with diameters of 26 nm produced significant heating. For materials with intermediate anisotropy energies such as iron oxide, an optimal size range between 18 – 22 nm was identified for the applied AMF parameters. The SLP value of iron oxide MNPs 22 nm in diameter was measured to be 716 ± 31 W g^{-1}, which is among the highest recorded values for synthetic ferrite materials at the given frequency and field strength [59]. This behavior is consistent with the calculated areas of the hysteresis loops presented in Chapter 3, which increase progressively with size up to 22 nm due to a transition from reversible superparamagnetic to ferromagnetic hysteresis loss regimes. Above this size range, minor hysteresis loops are accessed due to the increased anisotropy field of the nanoparticle, which requires larger field amplitudes for full coherent magnetization reversal of the nanoparticle ensemble.

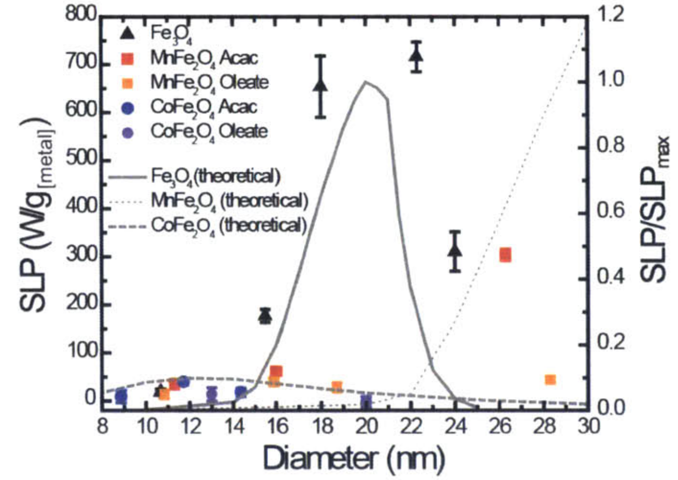

Figure 6.4 SLP measurements as a function of NP size (measured by TEM) obtained at $H_0 = 15.5 \pm 1.4$ kA m^{-1} and $f = 500$ kHz. The calculations based on theoretical models are normalized to the maximum SLP value calculated for 20 nm iron oxide MNPs, and the experimental SLP are normalized to the metal content determined from elemental analysis.

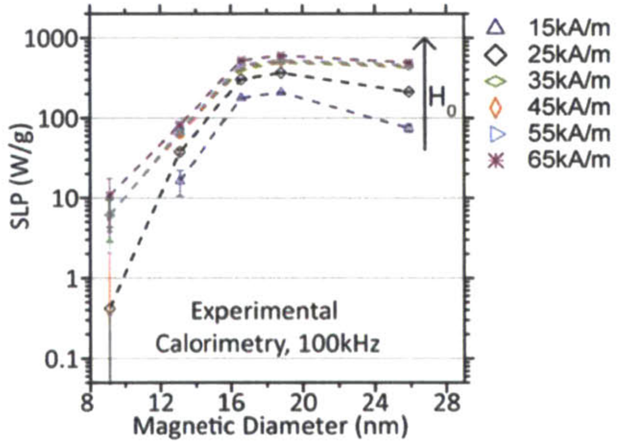

Figure 6.5 Experimental calorimetry data measured for iron oxide MNPs with various magnetic diameters. Field conditions were $f = 100$ kHz at amplitudes from 15-65 kA/m as indicated in the legend right of this figure [6].

We also studied size-dependent loss powers of iron oxide nanoparticles at different field amplitudes at a frequency of $f = 100$ kHz (**Figure 6.5**). When driven at field amplitudes ($H_o > 35$ kA/m) near the anisotropy field (H_k), large MNPs (>18 nm) exhibit significantly higher loss powers than small MNPs, suggestive of the increased hysteresis by scaling the anisotropy energy barrier with increased volume. Consistent with the DH trends predicted in **Figure 3.4**, we observed saturation in SLP as the amplitude increased above 35 kA/m (**Figure 6.5**) [6]. We have empirically demonstrated that DH theory can qualitatively capture trends of SLP as a function of anisotropy energy and AMF parameters for iron oxide MNPs and may be extended to other material systems to further maximize SLP at clinically relevant field conditions.

6.6 High-Performance Ferrite Nanoparticles

While qualitative correlations were made between theoretical and empirical measurements of SLP, we found that there were discrepancies in the measured SLP between tertiary ferrite MNPs produced from the oleate and acetylacetonate precursors. MNPs synthesized from metal-oleate precursors exhibited lower measured SLP values compared to similarly sized MNPs prepared from metal acetylacetonate precursors, which was consistent with their lower saturation magnetization (**Table 5.1**). For example, 11 nm $MnFe_2O_4$ MNPs prepared from acac precursors exhibited SLP values of 35 W g^{-1} while MNPs prepared from oleate precursors have SLP values of 13 W g^{-1}. Furthermore, their low ferromagnetic volume fraction led to deviations from numerical simulations as seen in the measured SLP value of 44 $W/g_{[metal]}$ for 28 nm MNPs prepared from oleate precursors. By contrast, $MnFe_2O_4$ MNPs prepared from acetylacetonate chemistries trend with predictions due to their optimized magnetic properties, with a measured SLP of 304 $W/g_{[metal]}$. Similarly, DH predicts large nanoparticles near the ferromagnetic regime to exhibit larger SLPs at $H_o > H_k$, yet we measured higher SLPs for 22 nm MNPs than 25 nm MNPs (**Figure 6.5C**).

In Section 5.3, we demonstrated how the synthesis of nearly defect-free nanoparticles using solvent redox chemistry exhibited superior magnetic properties compared to similarly sized nanoparticles that were annealed to remove defects. We compared the SLPs for ~25 nm

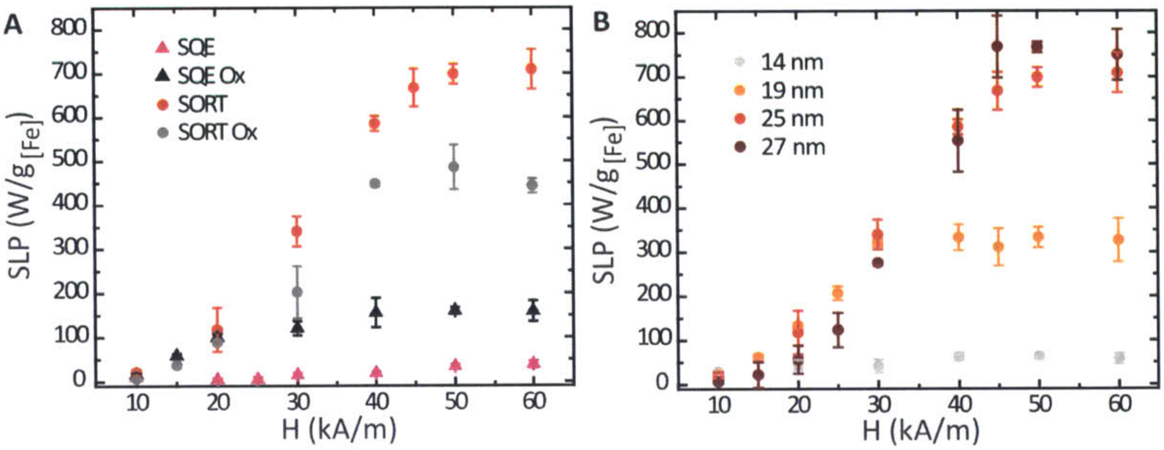

Figure 6.6 SLP as a function of field amplitude H_o at f=100 kHz for (A) ~25 nm nanoparticles composed of different phases and (B) nanoparticles with different diameters synthesized by SORT.

nanoparticles of different phase and defect compositions depicted in **Figure 5.3**, which are presented in **Figure 6.6A** at a frequency of f = 100 kHz and AMF amplitudes varied from 10-60 kA/m. Biphasic 25 nm MNPs (SQE) exhibited negligible SLP values (<50 $W/g_{[Fe]}$ at 100 kHz and 50 kA/m) that increased by a factor of 4 to 160 $W/g_{[Fe]}$ following oxidation (SQE Ox) (**Figure 6.6A**). At the same AMF conditions, 25 nm SORT nanoparticles had SLP values of 700 $W/g_{[Fe]}$. The 4.7 fold improvement highlights the necessity in preventing defect formation during the reaction. While SQE nanoparticles exhibit improved magnetic properties following oxidation, residual defects may serve as pinning layers to prevent full coherent reversal of the magnetic moment needed to maximize hysteretic losses [111]. As a result, the measured SLP is lower than predicted. For SORT-synthesized nanoparticles, we observed size-dependent increase of the SLP with increasing AMF amplitude that reached a plateau at ~40 kA/m (Figure 4E), which is qualitatively consistent with trends predicted by the DH model [6]. We found that 27 nm MNPs exhibited higher SLPs than 25 nm MNPs at H_o >45 kA/m, which was not observed with annealed nanoparticles presented in Section 6.5.

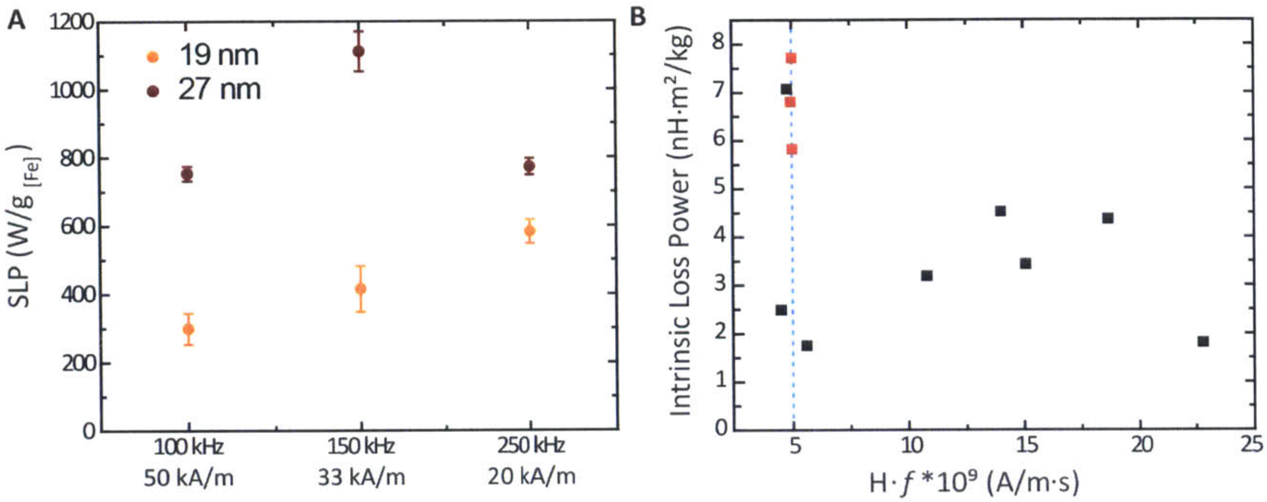

Figure 6.7 Specific and intrinsic loss powers of SORT nanoparticles. (A) SLP values measured for 19 and 27 nm SORT-synthesized iron oxide MNPs at different field frequencies and amplitudes with constant field product $H \cdot f = 5 \cdot 10^9$ A/m·s. (B) Intrinsic loss powers of synthetic iron oxide nanoparticles used in this study (red) compared to other reported values (black) as a function of the field product $H \cdot f$. Blue dashed line indicates upper limit set by the Brezovich criterion.

Within clinical limits for safe AMF exposure ($< H_o \cdot f = 5 \times 10^9$ $A \cdot m^{-1} \cdot s^{-1}$) [38], we measured SLPs exceeding 1000 $W/g_{[Fe]}$ for 27 nm MNPs (**Figure 6.7A**). The intrinsic loss power [112], a figure of merit intended for performance comparison between different laboratories, exceeded 7.5 $nH \cdot m^2/kg$, and is amongst the highest recorded for synthetic iron oxide nanoparticles (**Figure 6.7B**). Notably, it was observed at an AMF with an amplitude and frequency product <50% of the fields previously presented in Section 5.5 [1, 59]. The improved SLP values illustrate that defect elimination during the synthesis yields nanomagnetic agents with enhanced theranostic performance.

6.8 Transverse Relaxivity of Ferrite Nanoparticles

The MR relaxivity for the MNPs presented in **Figure 5.3** were also investigated for their potential application as theranostic agents. We measured the transverse relaxivity r_2 values of the PEG-MNPs synthesized by SORT and compared them to similarly-sized particles prepared in SQE and subjected to oxidation (**Figure 6.8A, B**). SORT-synthesized MNPs exhibited an r_2 of 543 $mM^{-1}s^{-1}$, which was 3.6 times greater than the r_2 determined for oxidized MNPs containing defects. Note that r_2 values of 740 $mM^{-1}s^{-1}$ near the theoretical limit of 800 $mM^{-1}s^{-1}$ were previously observed for 28 nm iron oxide nanocubes synthesized in pure DBE, which similarly required phase-pure ferrimagnetic nanoparticles dispersed as single core magnets to observe these exceptionally high values [113].

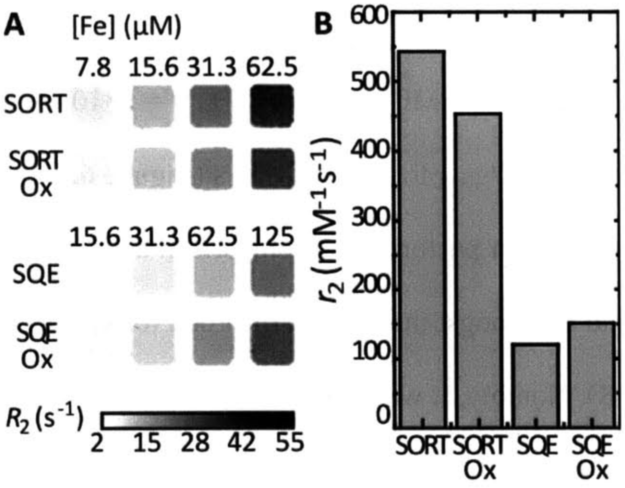

Figure 6.8 (A) T_2-weighted magnetic resonance images at 7 T of iron oxide nanoparticles at different concentrations for 25 nm nanoparticles from the four synthetic protocols. (B) Comparison of the measured r_2 values.

6.6 Conclusion

In Chapter 4, we found that the solvent can bias the nanoparticle's phase composition towards or away from its thermodynamically favored FiM configuration during synthesis. Surprisingly, analysis of the reaction environment with FTIR spectroscopy revealed that the solvents exhibited redox activity, with aromatic ethers identified as potential in-situ oxidizers. Introduction of aromatic ethers into solvent mixtures with reflux temperatures >300 °C enabled the synthesis of nearly defect-free ferrite MNPs with nanocrystal sizes in the 10-30 nm superparamagnetic to ferromagnetic transition regime. We saw in Chapter 5 that the MNPs synthesized via SORT exhibited low anisotropic peak broadening, lack of exchange bias and high-field susceptibility, M_s near bulk values, and a pronounced Verwey transition. These hallmark features of nearly defect-free magnetite nanoparticles were absent in nanoscale ferrites prepared by conventional oxidation methods. This structural optimization of the MNPs led to their enhanced performance as MR contrast agents with r_2 values exceeding 500 $mM^{-1}s^{-1}$, and as magnetothermal transducers with SLP exceeding 1000 $W/g_{[Fe]}$ recorded for 27 nm nanoparticles at clinically relevant AMF conditions.

Chapter 7

Wireless Magnetothermal Stimulation of Heat-Sensitized Cells

7.1 Summary

This thesis culminates with the application of the magnetic nanoparticles as wireless transducers of neural activity through magnetothermal power dissipation. In this chapter, we demonstrate minimally-invasive and remote neural excitation through the activation of the heat-sensitive capsaicin receptor TRPV1 using the magnetic nanoparticles detailed in Chapters 4-6. When exposed to alternating magnetic fields, the nanoparticles dissipate heat generated by hysteresis, triggering widespread and reversible firing of TRPV1$^+$ neurons. Wireless magnetothermal stimulation in the ventral tegmental area of mice evoked excitation in subpopulations of neurons in the targeted brain region and in structures receiving excitatory projections. The nanoparticles persisted in the brain for over a month, allowing for chronic stimulation without the need for implants and connectors.

The content of this chapter is based on published work found in reference [4]. Custom AMF apparatuses for *in vitro* and *in vivo* experiments were developed by Michael Christiansen.

7.2 Experimental Methods.

7.2.1 Molecular Cloning and Virus Packing.

Rat Vr1 (TRPV1) in pCDNA3 was a gift by D. Julius (UCSF), and pLenti-CamKII-hChR2 (T159C)-p2A-mCherry-WPRE was a gift by K. Deisseroth (Stanford). For the construction of pLenti-CaMKIIa-TRPV1-p2A- mCherry, we first obtained the TRPV1 fragment from pCDNA3 by PCR with the primers GGGGATCCGCCACCATGGA ACAACGGGCTAGCTTAG and CGGGCGCGCCTTTCTCCCCTGGGACCATGG to introduce BamH1 and AscI restriction sites. After digestion and purification, the PCR product was cloned into the pLenti construct between the BamH1 and AscI site, replacing hChR2. Packing of the plasmid into Lenti virus was done according to established protocols [8].

7.2.2 General Cell Culture.

The HEK293FT cell line was a gift by F. Zeng (MIT). Cell culture was maintained in DMEM with GlutaMAX™ supplemented with 10% Fetal Bovine Serum (FBS). To promote adhesion of the HEK293FT cells to glass substrate for imaging during field stimulation, 4 x 5 mm glass slides in each 24 well plate were coated with 100 µL of Matrigel® solution (50 µL Matrigel® in 1.5 mL of DMEM+FBS) overnight prior to cell seeding at 80% confluency in 24-well plates. Transfections were performed using 1 µL of Lipofectamine® 2000 with 500 ng of total DNA in Opti-MEM and used for imaging and magnetothermal stimulation a day after transfection. Hippocampal cell culture was isolated according to established protocols (1). Dual viral transfection was achieved by first adding 1 µL (10^9 transducing units/mL) of the *Lenti- CamKIIα::TRPV1-p2A-mCherry* or *Lenti-CamKIIα::mCherry* followed by a 3 day induction period. Then, 0.5 µL (10^{12} transducing units/mL) of *AAV9-hSyn::GCaMP6s* was added. *In vitro* magnetothermal stimulation was performed 5 days later.

7.3.3 *In vitro* magnetothermal stimulation.

A custom built coil, consisting of litz wire wound around a toroidal soft ferromagnetic core with a 7.5 mm gap, was used to apply an alternating magnetic field stimulus. A voltage signal from a function generator amplified by a 200W amplifier was used to drive the coil at its resonance with a series capacitor, with a transformer impedance-matching the amplifier. The field magnitude was measured by an inductive pickup loop of known geometry and an oscilloscope. HEK293FT cells in 2 mg/mL ferrofluid in PBS were stimulated for 30 s with alternating magnetic field at 500 kHz and 15 kA/m during 60 s long fluorescence recordings. Primary hippocampal cultures in 10 mg/mL ferrofluid in Tyrode's solution were stimulated with 10 s field pulses at 500 kHz and 15 kA/m with a 50 s rest period repeated 3 times during the fluorescent recordings.

7.3.4 Subjects.

Male C57BL/6 mice (Jackson Laboratory) aged 8 weeks were maintained with a reverse 12-hr light/dark cycle and provided food and water *ad libitum* during the duration of the experiment. Animal husbandry and all experimental procedures were approved by the MIT Committee on Animal Care.

7.3.5 Stereotactic injection for heat sensitization.

All mouse surgeries were performed under aseptic conditions using a stereotaxic frame. Mice were anesthetized via an intraperitoneal injection of ketamine (100 mg/kg) and xylazine (10 mg/kg) mixture. Coordinates used for injection into the ventral tegmental area (VTA) relative to bregma were established according to the Mouse brain Atlas (*34*) as followed: -4.5 mm dorsoventral, ± 2.9 anteriorposterior, and -0.5 mediolateral. 1.5 μL of Lentivirus solution was bilaterally injected into the VTA using a 10 μL nanofil syringe with a beveled 34 gauge needle facing the dorso-lateral side at 0.1 μL/min using a microsyringe pump and its controller. Immediately after injection, the syringe was lifted up by 0.1 mm and remained within the brain for an additional 10 minutes prior to slow withdrawal. Skin tissue was closed with an adhesive and sutures, and the mouse was allowed to recover on a heat pad. Magnetothermal stimulation was conducted 4-6 weeks following injection to allow for viral expression.

7.3.6 *In vivo* magnetothermal stimulation.

Mice were anesthetized as previously described. Using the VTA coordinates, a 2.5 μL MNP solution (100 mg/mL) was bilaterally injected as described above. Once the skin was closed, the head was placed within the 18 mm gap of a toroidal field coil otherwise similar to the one employed for in vitro experiments and driven by the same circuit. The gap was insulated with Styrofoam lining and cooled with ice-water pumped through tubing wound around the core. 10s pulses of alternating magnetic field at 15 kA/m and 500 kHz were delivered with 50s rest intervals in between over the course of 20 minutes. Mice were sacrificed after 90 min to allow for c-fos expression. For chronic stimulation, anesthetized mice were subjected to the same field treatment paradigm one month after ferrofluid injection and sacrificed after a 90 min c-fos induction period.

7.3.7 Immunohistochemistry.

Anesthetized mice were perfused transcardially with PBS and 4% paraformaldehyde (PFA) at 100 minutes after the magnetic field stimulation. Isolated brains were fixed in 4% PFA overnight and equilibrated in 30% sucrose for cryoprotection. 40 μm-thick coronal sections were cut on a vibratome. Free-floating sections were then incubated for 30 minutes in 0.3% TritonX100 and 3% normal donkey serum (NDS) followed by overnight incubation with rabbit anti-c-fos (1:500 in 3% NDS/PBS) at 4 °C. After washing twice with PBS for 20 minutes each step, sections were incubated with secondary anti-rabbit antibodies conjugated to Alexa Fluor 488 for 3 hours at room temperature. Following two more washes with PBS, the slices were incubated with 4',6-diamidino-2-phenylindole solution in PBS (DAPI, 1:50,000) for 20 minutes and subsequently washed three more times and mounted on glass slides with PVA-DABCO. Primary antibodies for the biocompatibility study and dilutions are provided in **Table 7.1**.

Table 7.1 Antibodies and dilutions.

Primary Antibody	Secondary Antibody
Rabbit anti-cfos (1:500, Calbiochem)	Goat anti-rabbit, Alexa Fluor 488 (1:1000, Life technologies)
Rabbit anti-NeuN (1:500, abcam)	Goat anti-rabbit, Alexa Fluor 488 (1:1000, Life technologies)
Goat anti-GFAP (1:1000, abcam)	Donkey anti-goat, Alexa Fluor 633 (1:1000, Life technologies)
Goat anti-Iba1 (1:500, abcam)	Donkey anti-goat, Alexa Fluor 633 (1:1000, Life technologies)

7.3.8 Fluorescence change quantification for action potential detection.

The relative fluorescent change ΔF/F of somatic fluorescence signals was acquired with ImageJ for all neurons within a particular trial. Action potential events were detected with an automated algorithm that searched point by point through a trace for events. An event was counted if it satisfied two criteria: (i) the fluorescence increase was at least 5 standard deviations (5σ) above baseline, which was defined as the first 10 seconds of each trace, and (ii) the event persisted for more than 250 ms (**Figure 7.1**). Shorter events were discarded. To make the algorithm less sensitive to baseline drift, a linear regression fit every 1 s was subtracted before the current position was counted. Using the same algorithm across all trials with no adjustment between conditions, 86% of events were correctly identified with 3% false negatives and 11% false positives (of 165 events counted, 5 were missing and 18 incorrectly assigned). Raster plots generated from this algorithm were randomized and further assigned in 2 s bins. The percentage of responsive neurons was counted as the number of neurons that spiked within 5 s after magnetic field was turned off and averaged over three cycles over three trials.

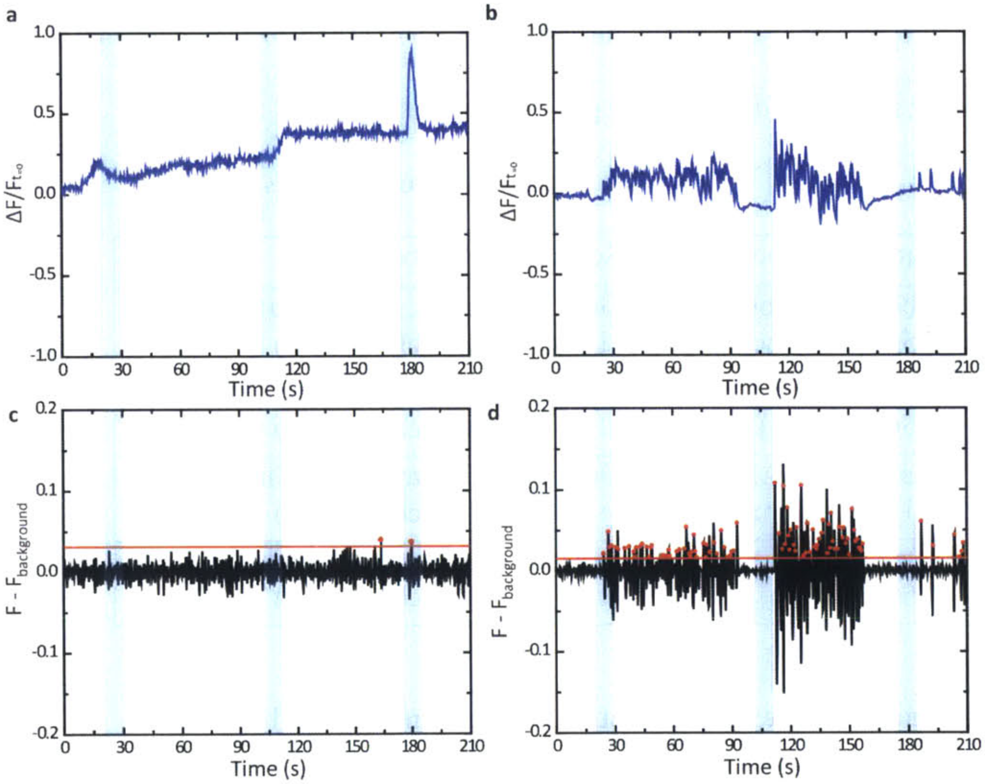

Figure 7.1 Fluorescence change quantification for action potential detection. ΔF/F raw trace of **(A)** TRPV1$^-$ and **(B)** TRPV1$^+$ neuron subjected to three rounds of alternating magnetic field treatment in ferrofluid. Automated algorithm subtracts baseline drift from data and counts action potential events indicated by red dot for **(C)** TRPV1$^-$ and **(D)** TRPV1$^+$ neurons. Red line indicates threshold to count an event. Blue colored area indicates duration of AMF pulse.

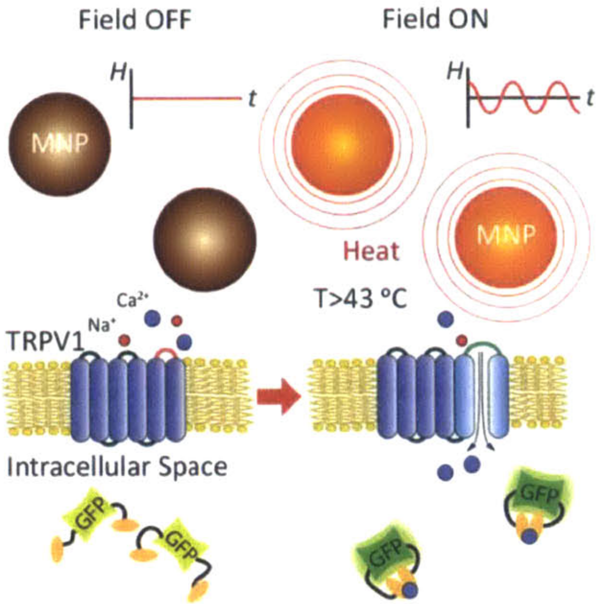

Figure 7.1 Experimental scheme. Magnetic field stimulation ('Field ON') of TRPV1 from MNP heating is visualized by GCaMP6s fluorescence changes.

7.3 Magnetothermal Scheme for Cellular Control.

To achieve reversible neuronal activation with alternating magnetic fields (AMF), we developed an intracellular calcium control scheme by sensitizing cells to heat generated from MNPs (**Figure 7.2**). Earlier experiments relied on synthetic transgenes to target MNPs to the cell membrane and required 10s to 1000s of seconds to observe increased calcium ion (Ca^{2+}) influx, which exceeded temporal dynamics of neuronal firing by orders of magnitude. Streptavidin or His-Tag functionalized magnetic nanoparticles were tethered to cell membrane in close vicinity to TRPV1 channels, which enabled control of neuronal action potential and insulin transcription *in vitro* with AMF exposure times of 10s of seconds to minutes [12, 13].

The efficacy of this approach may be lost when applied to chronic neuromodulation. While Fourier heat transfer laws suggest that thermal equilibrium should reach steady state within <1s at nanoscale dimensions with negligible temperature increase at the MNP surface [114, 115], recent evidence suggest longer timescales with large temperature changes at equilibrium [104, 116, 117].

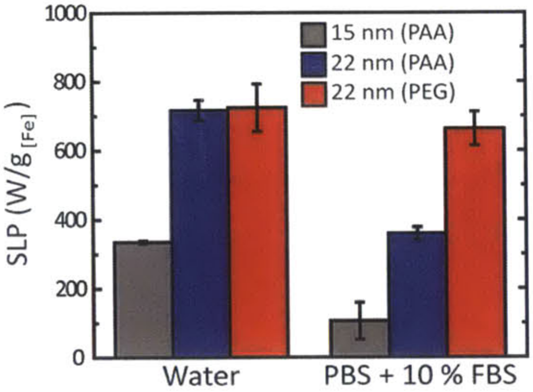

Figure 7.2 Specific loss power (SLP, normalized to iron content [Fe]) measurements in water and in phosphate buffer saline (PBS) with 10% fetal bovine serum (FBS). The SLP was calculated from the rate of temperature increase of a 1 mg/mL [Fe] sample. Compared to ~15 nm in diameter MNPs currently used in clinical settings, our 22 nm ± 1.2 in diameter MNPs have a two-fold higher SLP. A decrease in SLP is observed for poly(acrylic acid)-MNPs (PAA) when transferred into PBS supplemented with 10% FBS due to electrostatic screening which induces flocculation [1, 2]. By preventing aggregation in sterically stabilized poly(ethylene glycol)-MNPs (PEG), high SLP is preserved at physiological conditions.

A fundamental understanding of nanoscale thermal transport remains elusive, and requires further experimental validation to reduce latency times for neuromodulation [118]. Furthermore, recent studies suggest that MNP functionalization with proteins induces cell internalization and the formation of protein coronas that may reduce the effectiveness of targeting and heat dissipation *in vivo* [119, 120]. We reasoned that un-targeted Fe3O4 MNPs optimized for efficient heat dissipation at clinically relevant alternating magnetic field conditions can (i) reduce the latency period for neural excitation, (ii) eliminate exogenous targeting transgenes, and (iii) have chronic utility *in vivo* because MNPs exhibit minimal cytotoxicity and remain intact several months after injection [41, 121]. Spherical Fe3O4 MNPs 22 nm in diameter possess some of the highest heating rates per gram, or specific loss power, measured for a synthetic material at a therapeutically relevant frequency f=500 kHz and field amplitude H_o=15 kA/m [1]. As described in Chapters 4 and 6, we prepared these monodisperse MNPs via the thermal decomposition of an environmentally benign iron-oleate precursor [68], and dispersed them in physiological buffers through high-temperature ligand exchange with poly(acrylic acid) followed by conjugation with poly(ethylene glycol (M_w=5000) [1]. These MNPs exhibited specific loss power of 660 W/g ± 50 at physiological conditions, which is 6-fold higher than hyperthermia agents currently used in clinical settings (**Figure 7.3**) [122]. Magnetic fields were generated by a resonant coil custom-designed for fluorescence imaging during stimulation (**Figure 7.4**). Although TRPV1 is naturally expressed across the mammalian nervous system [123], we designed a transgene to establish sustained and uniform levels of TRPV1 expression for magnetothermal membrane depolarization across different cell lines [124]. The TRPV1 transgene was placed under the excitatory neuronal promoter calmodulin kinase II α-subunit along with mCherry separated from TRPV1 by the post-transcriptional cleavage linker p2A (*CamKIIα::TRPV1-p2A-mCherry*) [125] and packed into the lentiviral vector to enable long-term *in vitro* and *in vivo* neural transfection [126]. Cells were additionally transfected with the adeno-associated virus serotype 9 (AAV9) carrying GCaMP6s under the neuronal promoter human synapsin (*hSyn::GCaMP6s*) for measurement of intracellular Ca^{2+} changes as a proxy for membrane depolarization [127]. GCaMP6s is a circularly permuted green fluorescent protein fused to calcium-binding calmodulin, which increases brightness in a calcium dependent manner to enable quantification of intracellular calcium levels [127]. Functionality of the two genes was confirmed by observing increased fluorescence intensity in response to capsaicin, a TRPV1 agonist, and temperature increase above 43 °C in non-excitable HEK293FT cells (**Figure 7.5**).

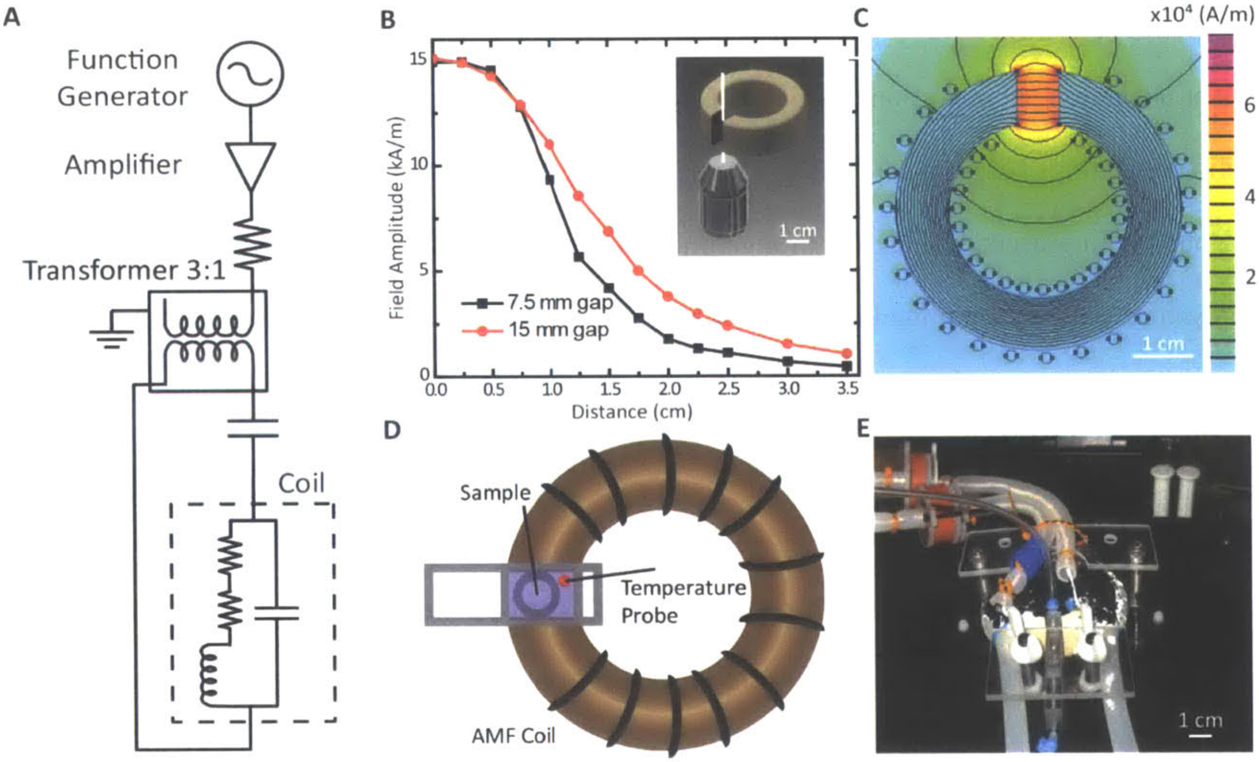

Figure 7.4 *In vitro* coil design for simultaneous magnetothermal stimulation and fluorescent imaging. (A) Schematic of the resonant circuit. The coil (represented schematically as a non-ideal inductor in the dashed box) is wrapped around a toroidal core with a machined gap. (B) The component of the field tangential with respect to the gapped toroid was measured at points along the axis of the microscope lens, passing through the center of the gap, which was set as the origin. An inductive pickup loop and an oscilloscope were used for this purpose. Each measurement represents an average over the area of the inductive pickup loop, which has a 3.0 mm radius. The *in vitro* alternating magnetic field coil was machined with the smallest possible gap (7.5 mm) to accommodate the 5 mm cover glass slips seeded with HEK293FT cells and neurons with minimal inductive heating of the microscope lens. When a 15 mm gap is used, fringing fields with larger amplitudes cause significant drift during magnetothermal stimulation, preventing real-time fluorescent imaging of GCaMP6s transfected cells. (Inset) A rendered image of axis (white line) relative to coil and microscope lens used during field profile measurement. (C) Model of field line distribution generated with finite element method magnetics software at 20 A DC current for a planar 23-turn two-dimensional gap coil (7.5 mm). The field in the gap is expected to scale linearly with the number of turns and linearly with the current. Small gaps reduce fringing fields, confining the field more uniformly in the machined gap. (D) Schematic showing sample holder design and sample placement allowing for concomitant alternating magnetic field stimulation and temperature measurement. (E) A photograph of the alternating magnetic field coil used for *in vitro* experiments.

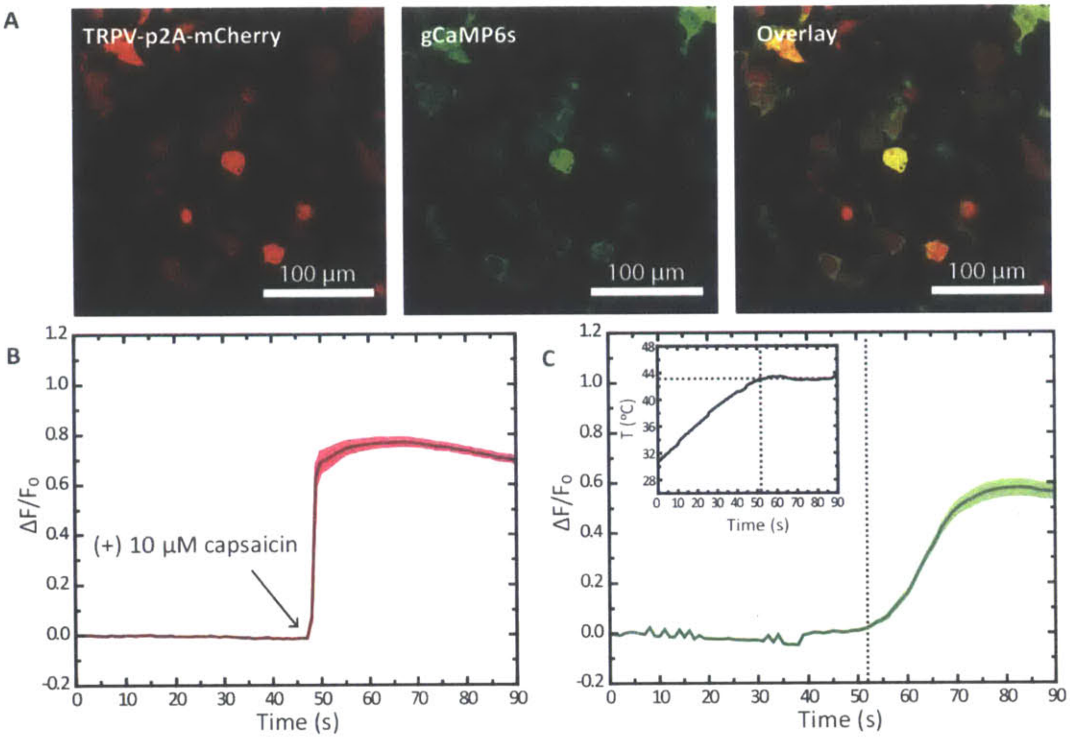

Figure 7.5 Dual transgene system for magnetothermal stimulation and visualization. (A) Confocal image of HEK293FT cells expressing the *Lenti-CamKIIα::TRPV1- p2A-mCherry* and *Lenti-hSyn::GCaMP6s* construct transfected with lipofectamine after 24 hours. To test the functionality of both the TRPV1 and GCaMP6s transgene, we added (B) capsaicin (magenta) and (C) exposed the cells to a temperature ramp up to 43 °C (green). Dashed lines indicate time when 43 °C is reached. Inset: Temperature profile during heat test. A large fluorescence increase was observed with both stimuli. Shaded areas represent standard error while solid line is the average over 20 cells.

7.4 *In vitro* magnetothermal stimulation.

We first demonstrated magnetothermal control of intracellular Ca^{2+} influx in HEK293FT cells. Fluorescence intensity maps indicated that only cells expressing TRPV1 ($TRPV1^{+}$) responded to the field stimulus (f=500kHz, H_o=15 kA/m) when incubated in MNP solutions (2 mg/mL), while cells not expressing TRPV1 ($TRPV1^{-}$) as well as $TRPV1^{+}$ and $TRPV1^{-}$ cells without field stimulus did not exhibit significant changes in intracellular Ca^{2+} concentration (**Fig. 7.6A, B**). Field-induced temperature increase in excess of 43 °C in MNP solutions triggered

GCaMP6s fluorescence increase $\Delta F/F_0 > 50\%$ in 36.1% ± 4.3 (mean ± std) of TRPV1$^+$ cells, while only 1.7% ± 1.6 (mean ± std) of TRPV1$^-$ cells exhibited a similar response (**Figure 7.6 C-F**). Magnetothermal membrane depolarization was sufficient to evoke trains of action potentials in primary hippocampal neurons expressing TRPV1 when exposed to 10 s field pulses at 60 s intervals (**Figure 7.1, 7.7**). Viral transfection with *AAV9-hSyn::GCaMP6s*, which allows for fluorescence detection of single action potential events [127], and *Lenti-CamKIIα::TRPV1-p2A-mCherry* (TRPV1$^+$) or *Lenti-CamKIIα::mCherry* (TRPV1$^-$) yielded a co-expression efficiency of 57 % after 5 days (**Figure 7.7A**). In MNP solutions (10 mg/ml), 85% ± 14 of TRPV1+ neurons exhibited synchronized firing within 5 s following stimulus, while only sporadic activity was observed in TRPV1– neurons (**Figure 7.7B-H**). This implies that the temperature increase (**Figure 7.7D**) in MNP solutions exposed to alternating magnetic field was sufficient to trigger TRPV1 (**Figure 7.7H**), while avoiding non-specific thermal effects such as changes in membrane capacitance (**Figure 7.7F**) [128]. In the absence of MNPs, magnetic field did not induce appreciable solution heating (**Figure 7.7C**), and no correlated response was observed in TRPV1$^+$ and TRPV1$^-$ neurons (**Figure 7.7B, E, G**). We recorded neural activity from GCaMP6s temporal fluorescence traces [129]. Waves of Ca^{2+} spikes were repeatedly induced by field pulses only in TRPV1$^+$ neurons in the presence of MNPs (**Figure 7.7I-P**). The observed 5 s latency between the field application and the onset of neural activity is 5-fold faster than previously described [12].

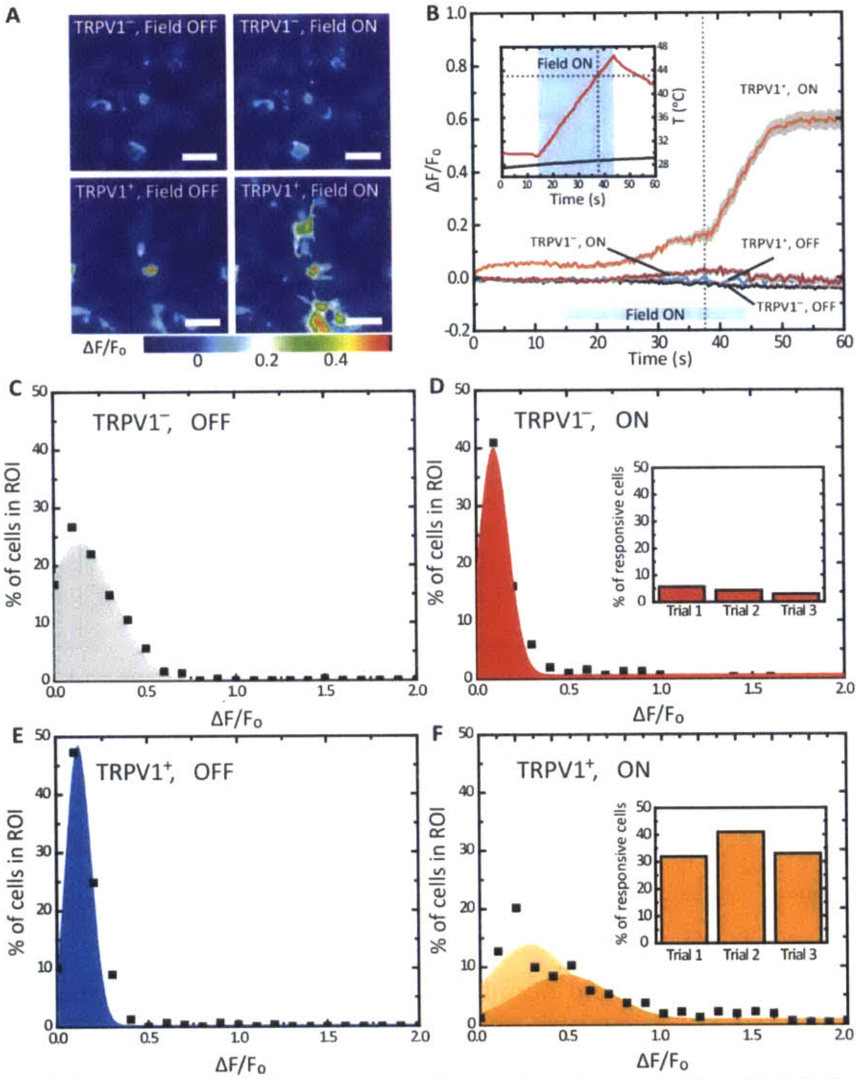

Figure 7.6 (A) Color maps of fluorescence intensity changes for TRPV1– and TRPV1+ HEK293FT cells before and during magnetic field stimulus. Scale bar = 50 μm. (B) Normalized fluorescence intensity change (ΔF/F0) as a function of time (solid lines = mean, shaded grey areas = standard error). Dashed line corresponds to the crossing of TRPV1 activation threshold temperature. Fluorescence increase observed only in TRPV1+ cells upon magnetic field application. Inset: Temperature profile without (gray) and with (red) magnetic field application. In all experiments field amplitude is Ho=15 kA/m and frequency is *f*=500 kHz. (C-F) Histograms of fluorescence intensity change measured for 300 HEK293FT cells across 3 trials of TRPV1- and TRPV1+ cells prior to (OFF) and immediately after (ON) alternating magnetic field stimulation. The fluorescent intensity change was binned into 10% ΔF/Fo increments (black square) and fitted with a Gaussian (filld curve). (F) Approximately 40% of TRPV1+ cells exhibited a fluorescence change > 50%, indicated by the second Gaussian fit in darker orange. Insets D, F: Percent of HEK cells responding to alternating magnetic field stimulus with a fluorescent change > 50 % across 3 trials. Heat alone did not change intracellular calcium levels demonstrating the necessity for cell lines to express the TRPV1.

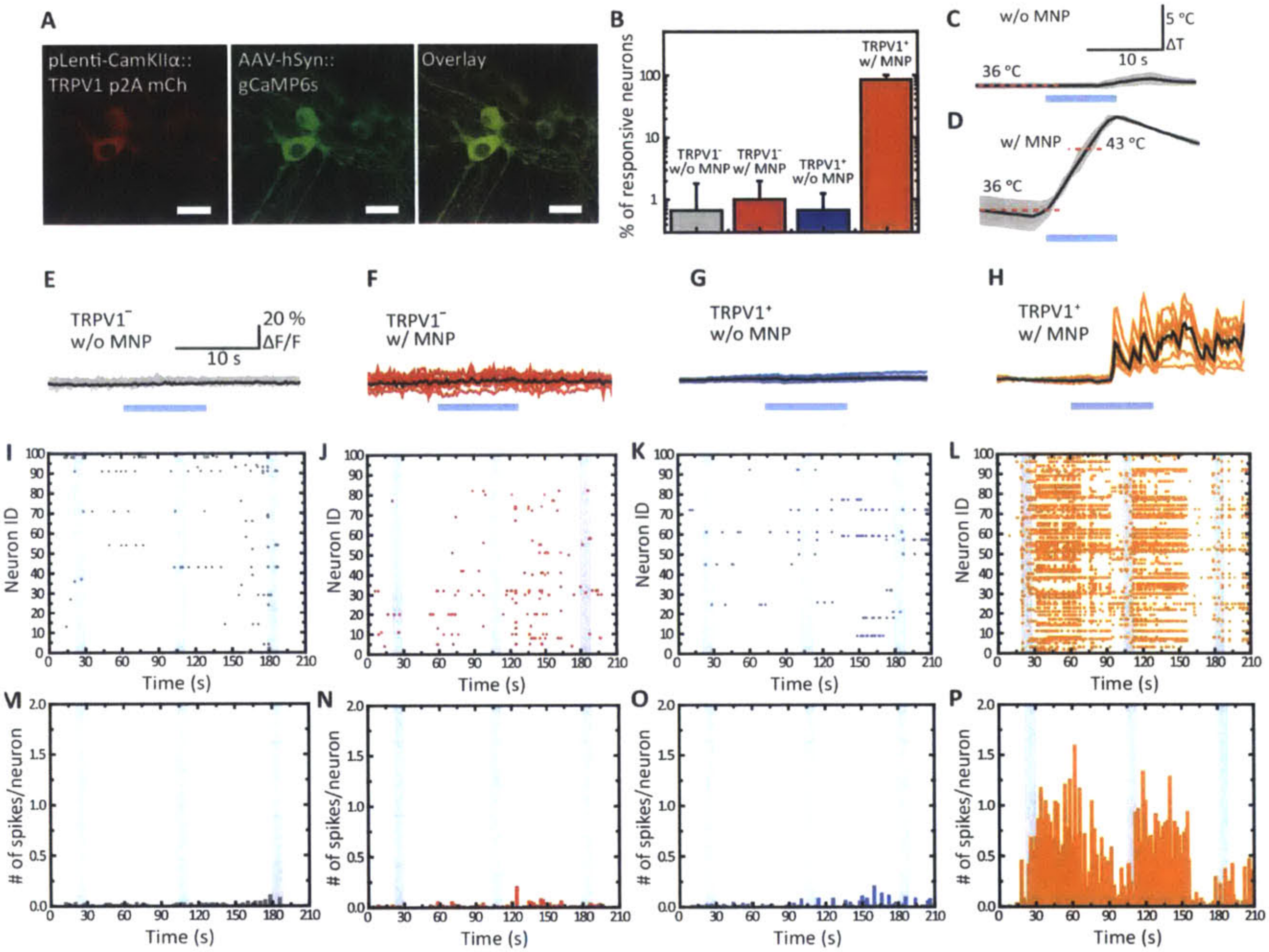

Figure 7.7 Alternating magnetic field stimulus evokes correlated and repeated trains of action potentials. (A) Confocal fluorescent images of co-transfected hippocampal neurons. Scale bar = 25 μm. (B) Population study of 100 neurons from 3 trials counting the number of neurons that spike within a 5 s bin following magnetic field stimulus. (C, D) Temperature profiles during magnetic field application in Tyrode's solution without (C) and with (D) MNPs. Shaded area is the standard deviation with average value overlaid (black). (E-H) Example fluorescence traces of 10 individual neurons with average overlaid (black). (I-L) Raster plots of 100 randomly selected neurons from 3 trials. Calcium spikes were counted according to an automated algorithm. (M-P) Peristimulus time histograms of the raster plots binned at 2 s. Color scheme for panels E-P: TRPV1$^-$ neurons in Tyrode's solution without MNPs (gray); TRPV1$^-$ neurons in Tyrode's solution with MNPs (red); TRPV1$^+$ neurons in Tyrode's solution without MNPs (blue); TRPV1$^+$ neurons in Tyrode's with MNPs (orange). Shaded blue bars represent alternating magnetic field pulses (H_o=15 kA/m, f=500 kHz).

7.5 Calibration of the thermal dosage for in vivo stimulation.

Before testing the magnetothermal scheme *in vivo*, the dissipated thermal load in tissue needed to be calibrated to avoid heat-induced cell death [130]. We calculated the steady-state temperature increase for a spherical microvolume of ferrofluid derived from Fourier's Law [114]:

$$\Delta T = \frac{SAR_v r^2}{2k} \tag{6.1}$$

where *r* is the radius of the loaded volume and *k* is the thermal conductivity of the medium. We found that high concentrations (>60 mg/mL) of nanoparticles need to be delivered for bilateral injections (2.5 μL) to reach sufficient temperature thresholds to actuate TRPV1 channels while avoiding hydrocephalus with short (< 10 s) AMF exposure time (**Figure 7.8A**). Due to perfusion of cerebrospinal fluid and blood in the brain for *in vivo* models, the calculated concentration from the Fourier analytical expression can be used only as an approximation of the required MNP concentration.

To account for heat transfer in an *in vivo* environment, Finite element modeling corroborated with temperature recordings in brain phantoms was used to predict local temperature changes in response to field stimulus (**Figure 7.8B-F, H**). The transient heat evolution of the infused MNPs allowed us to determine the length of magnetic field stimulation needed to reach 43 °C for different concentrations of MNPs (*36*). Pennes bioheat equation was used to model temperature transients within tissue:

$$\rho_B c_B \frac{\partial T}{\partial t} = k_B \nabla^2 T + \rho_b c_b w_b (T - T_b) + Q \tag{6.2}$$

Here Q is the heat power density generated by the nanoparticles. Q can be calculated as:

$$Q = V_{MNP} SLP_{MNP} \rho_{MNP} \tag{6.3}$$

where V_{MNP} is the total volume occupied by the magnetic nanoparticles in a 2.5 mm^3 droplet and ρ_{MNP} is the density of ferrites. Injections (2.5 μL) of MNP solution (100 mg/mL) delivered temperature gradients sufficient to reach the TRPV1 activation threshold within 5 s and cool back to 37 °C over 60 s cycles (**Fig. 7.8B-F**).

To determine whether prolonged exposure to noxious heat (~5 s) can induce irreversible cellular damage, we calculated the probability of cell survival as a function of exposure time (**Fig. 8.7G**) [131]. Hyperthermia effects on cellular components such as proteins, DNA, and membrane are dependent on reaction rates, which require an induction period before any thermal effect is observed. The temperature dependence of thermal damage can be estimated from quantifying resilience of different mammalian cells to hyperthermia [131]. The probability P of a cell surviving an exposure of time t (min) is:

$$P = 1 - (1 - (1 - R)^t)^n \tag{6.4}$$

where R is the rate of inactivation of a molecular target of number n, which varies from $R = 0.02 - 0.2$ min^{-1} at 44 °C [132]. The target number n is assumed to vary from 2-30 based on prior model fitting to empirical results. As an upper-bound estimate, only minor hyperthermic effects ($P < 0.5\%$) are predicted when cells are exposed for 30 s at 44 °C ($k = 0.2$ min-1) (Fig. 7.7G). In general, a minimum of 2 hours at 43 °C or 30 minutes at 45 °C was required to consistently produce a cytotoxic effect in primary neural culture [130]. Pulsed alternating magnetic field enables calibrated thermal dosages to excite TRPV1+ neurons while avoiding noxious heat damage. FEM modeling shows that the temperature drops below the 43 °C thermal threshold within 2 seconds at the MNP/neural interface. (**Fig. 7.8D-F**).

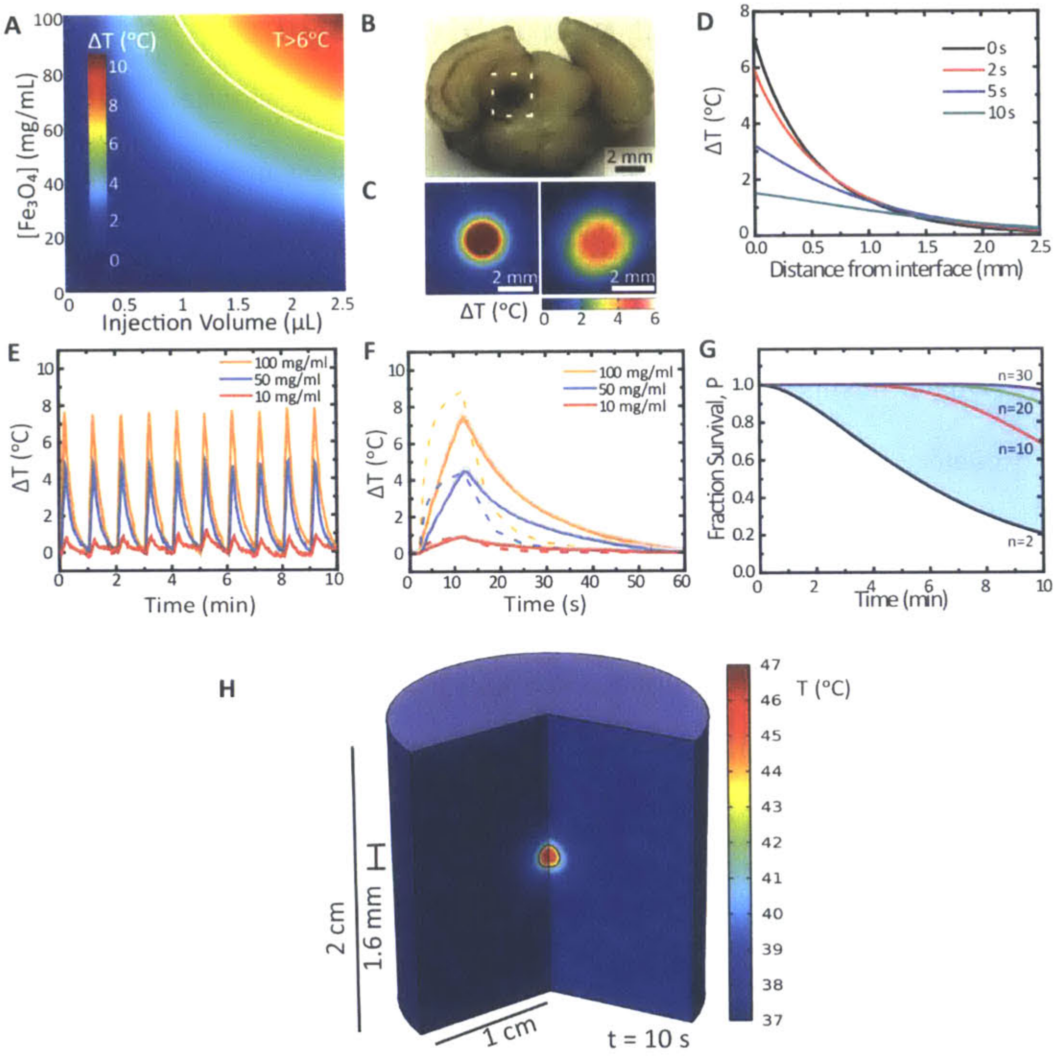

Figure 7.8 (A) Steady-state temperature change derived from Fourier's law as a function of MNP concentration and injection volume. Conditions that allow for temperature increase ΔT > 6 °C lie above the white line. **(B)** A photograph of a coronal slice of a mouse brain with MNP injection into the VTA indicated by the white box. **(C)** Temperature distribution within and around MNP injection after 10 s exposure to alternating magnetic field stimulus calculated by finite element modeling (left). Infrared thermograph indicating experimental temperature distribution within and around MNP droplet in brain tissue (right). **(D)** FEM of the thermal distribution change with time at the magnetic nanoparticle and neural tissue (starting at 0 mm). **(E)** Experimental data of temperature transients measured over 10 cycles of 10 s field pulses at 60 s intervals. **(F)** Average temperature transients over 20 cycles with standard deviation shaded in grey. FEM simulated data is indicated as dashed lines. **(G)** Upper bound estimation of cell survival in response to prolonged heat exposure at 44 °C for molecular targets ranging from n = 2-30 (shaded represents between range, solid lines for reference at n = 2, 10, 20 and 30). **(H)** FEM model used for calculating the temperature distribution within a ferrofluid infusion in brain tissue. The Pennes bioheat equation was used to account for perfusion and the corresponding physical parameters are given in **Table S2**.

7.6 Magnetothermal Deep Brain Stimulation

We next tested whether alternating magnetic field could activate a subpopulation of neurons in deep brain tissue in mice. With low endogenous expression of TRPV1 [133] and well-characterized projections [134], the ventral tegmental area (VTA) was an attractive deep brain target for initial demonstration of magnetothermal stimulation. Furthermore, phasic excitation in the VTA may have therapeutic implications in the treatment of major depression [31]. We sensitized excitatory neurons in the VTA to heat by lentiviral delivery of TRPV1, which was followed by MNP injection into the same region four weeks later (**Fig. 7.9A, B**). The anesthetized mice were exposed to the magnetic field conditions described in Section 7.5. Neuronal excitation was quantified by the extent of activity-dependent expression of the immediate early gene c-fos within a 250 μm vicinity of the MNP injection (**Fig. 7.9C-F**) [135]. Neural activity was only triggered by magnetic field in the VTA of mice transfected with TRPV1 in the presence of MNPs, resulting in a significantly higher proportion of c-fos positive (c-fos$^+$) cells as revealed by a two-way ANOVA with a Bonferroni post-hoc test ($F_{1,13}=47.5$, $P < 0.0001$, **Fig. 7.9G**). Control subjects testing whether the MNP injection, heat dissipation with field stimulus, or TRPV1 expression alone can result in neural stimulation showed no significant c-fos expression (**Fig. 7.9C-E, G**). Furthermore, the spatial extent of neuronal activation was largely collocated with TRPV1 expression in the VTA (**Fig. 7.9H, I**).

We next investigated whether neurons in the VTA can be activated 1 month after MNP injection to explore its chronic utility (**Fig. 7.10**). We again observed increased c-fos expression in the VTA only in mice transfected with TRPV1 in the presence of MNPs and exposed to the magnetic field protocol described above (**Fig. 7.10A, D "ON"**; Student's t-test, $P < 0.02$). In these mice, we also found evidence of field-evoked upregulation of c-fos in the medial prefrontal cortex (mPFC, **Fig. 7.10B, E "ON"**; Student's t-test, $P < 0.02$) and nucleus accumbens (NAc, **Fig. 7.10C, F "ON"**; Student's t-test, $P < 0.002$), which are known to receive excitatory inputs from VTA neurons [134, 136]. In the absence of stimulation, neurons in the VTA near the MNP injection site and the neurons in the mPFC and NAc did not exhibit increased c-fos expression (**Fig. 7.10A-F "OFF"**).

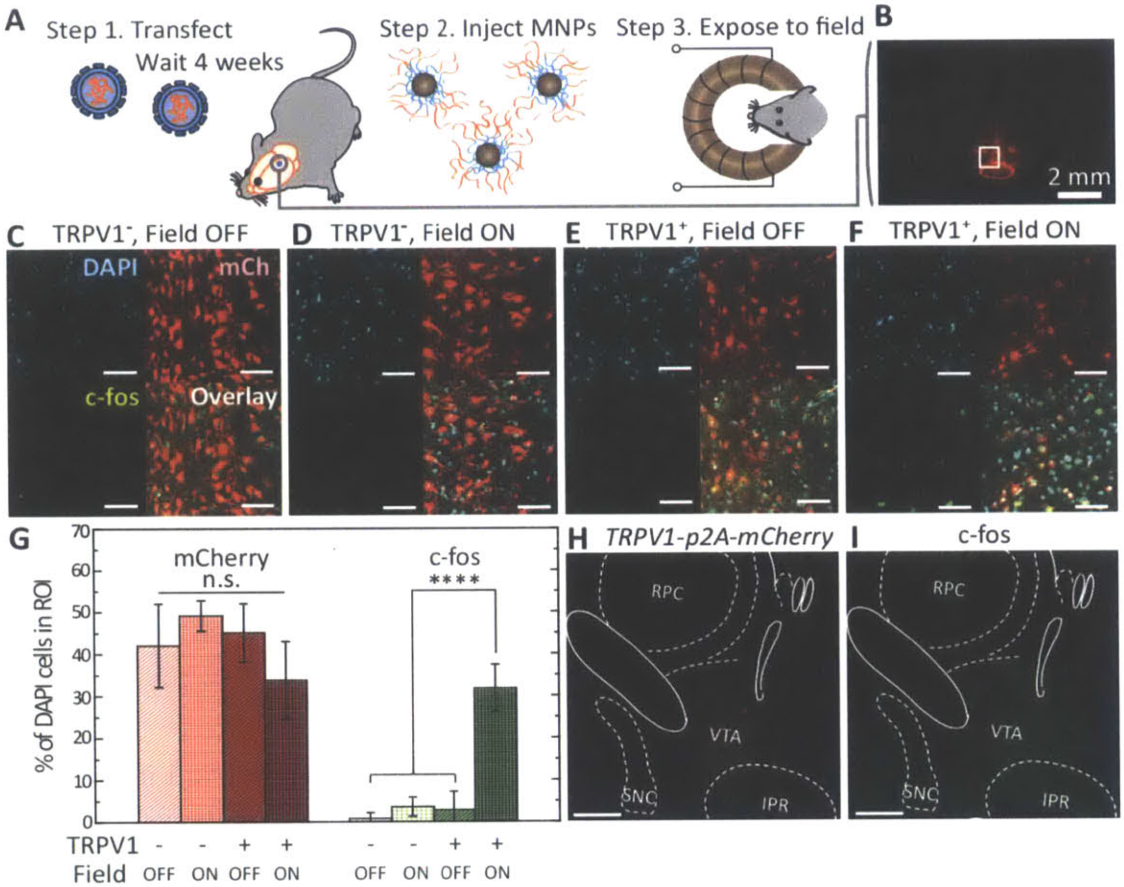

Figure 7.9 Wireless magnetothermal stimulation *in vivo*. **(A)** *In vivo* experimental scheme. **(B)** Confocal image of a coronal slice representative of the *TRPV1-p2A-mCherry* expression profile in the VTA. **(C-F)** DAPI (cyan), mCherry (red), and c-fos (green) and overlay confocal images of regions used for quantification of neural stimulation. Scale bar = 25 μm. All animals were injected with MNPs. Experimental conditions were **(C)** without (OFF) and **(D)** with (ON) magnetic field stimulation in TRPV1$^-$ VTA, and **(E)** OFF and **(F)** ON stimulation in TRPV1$^+$ VTA. **(G)** Percentage of mCherry-positive and c-fos-positive neurons within cell population indicated by DAPI corresponding to the four conditions presented in **C-F**. Significance is confirmed by two-way ANOVA with Bonferroni post-hoc test ($n=4$, $F_{1,13}=47.5$, $P < 0.0001$). **(H, I)** Confocal images of the VTA after acute magnetothermal stimulation. C-fos expression is largely confined to the VTA in regions where TRPV1 is expressed. Scale bar = 100 μm.

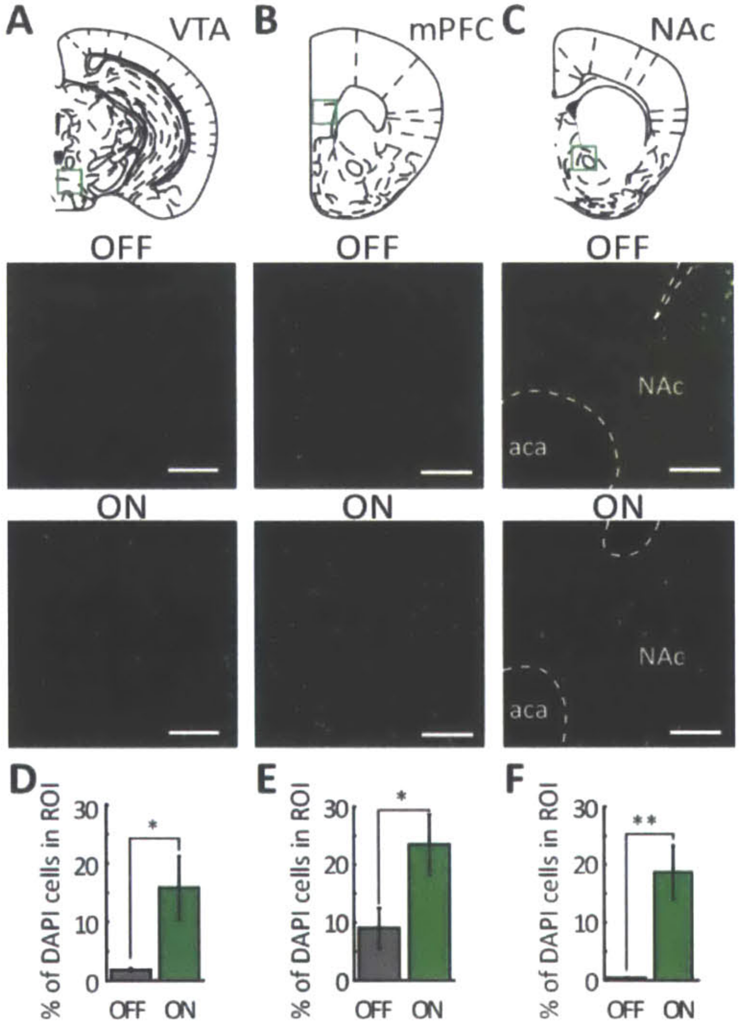

Figure 7.10 (A-C) Confocal images of the (J) VTA, (K) mPFC, and (L) NAc 1 month following MNP injection without (OFF) and with (ON) field treatment. Scale bar = 100 μm. (M) Percentage of c-fos+ neurons in the VTA among DAPI-labeled cells with and without magnetic field stimulation. Increased c-fos expression is observed following field treatment (ON) as compared to unstimulated (OFF) controls (n=3 OFF/ON; Student's t-test, $P < 0.02$). (N, O) Similarly, upregulation is observed in (N) the mPFC and (O) in the NAc with alternating magnetic field (ON) as compared to the same regions without (OFF) the field stimulus (n=3 OFF/ON; Student's t- test * $P < 0.02$, ** $P < 0.002$).

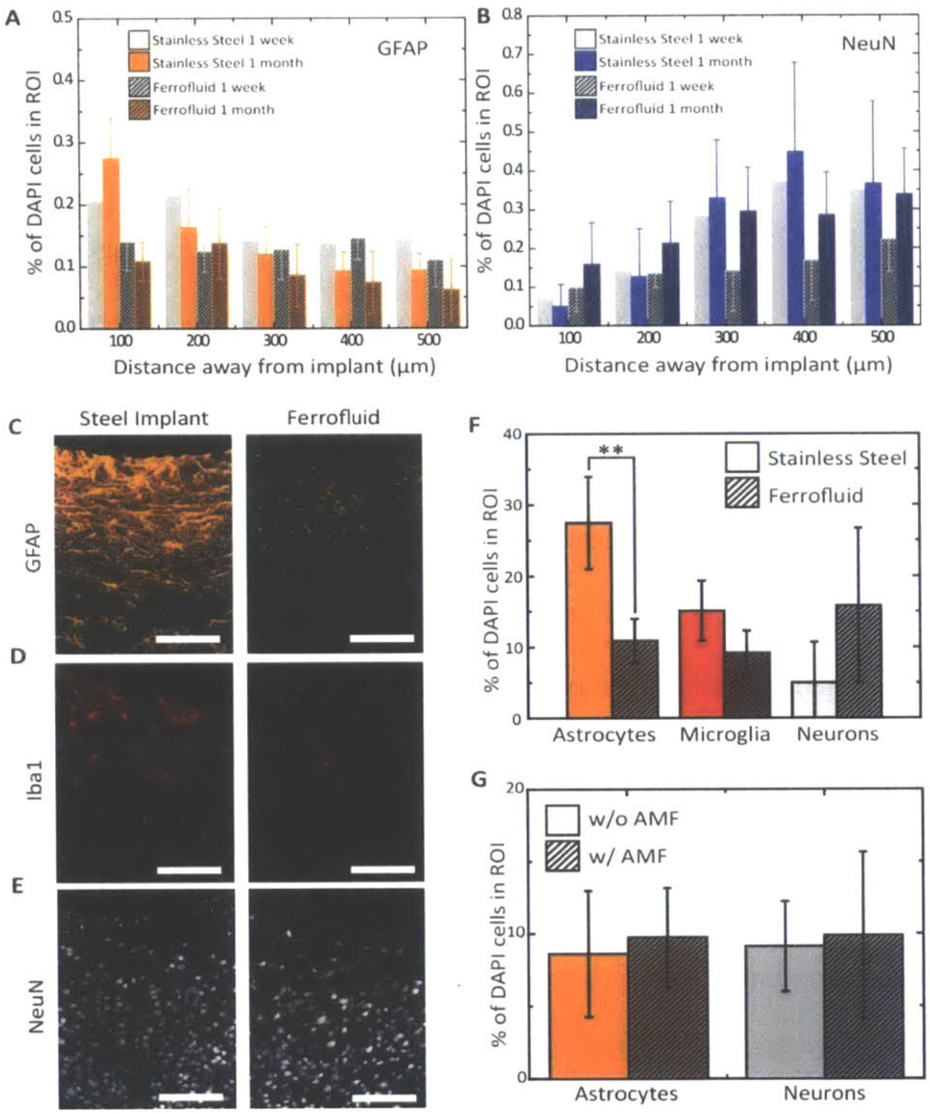

Figure 7.11 Assessment of chronic biocompatibility of MNP injection. (A) GFAP$^+$ astrocytes quantified within cell population indicated by DAPI as a function of distance in 100 μm bins from the neural/implant interface 1 week and 1 month following MNP injection or wire implantation surgery. (B) Neurons quantified by NeuN stain within cell population indicated by DAPI as a function of distance in 100 μm bins from the neural/implant interface 1 week and 1 month following surgery. (C-E) Confocal images of (C) astrocytes (GFAP), (D) activated microglia (Iba1), and (E) neurons (NeuN) at the stainless steel wire and injected MNP interfaces. (F) Density of astrocytes, neurons, and microglia within a 100 μm vicinity of a stainless steel wire and ferrofluid injection interfaces at 1 month following implantation/injection (n=3; GFAP Student's t-test, $P < 0.01$). (G) Density of astrocytes and neurons within a 100 μm vicinity of a ferrofluid interface at 1 week with and without 3 alternating magnetic field treatment sessions (n=3, $P > 0.05$). Scale bar = 100 μm.

7.7 Biocompatibility of Injected Nanoparticles

Due to blood-brain barrier breach and large modulus mismatch, foreign devices implanted into the brain will elicit an immunoreactive response [137]. To sequester the implant, activated cells supportive of the nervous system, such as astrocytes, macrophages, and microglia, accumulate at the site of injury to form a glial scar, which may hinder proper neural function at the implantation site [138]. We compared the biocompatibility of the MNP injection to a similarly sized stainless steel implant through immunohistochemical staining of $NeuN^+$ neurons, $GFAP^+$ astrocytes, and $IbaI^+$ microglia to characterize this foreign body response (**Fig. 7.11**). The interface between the MNP injection and the tissue exhibited significantly lower glial activation and macrophage accumulation, and higher proportion of neurons as compared to the steel implant 1 week and 1 month after surgery (**Fig. 7.11A-F**). The improved tissue compatibility can likely be attributed to the mechanically pliable nature of the MNP injection and sequestration via endocytosis [41, 121]. No difference in neuronal or glial density was observed between brain tissue of stimulated and unstimulated mice, suggesting that the rapidly dissipated magnetothermal cycles cause minimal thermal damage to the surrounding tissue (**Fig. 7.11G**).

7.8 Reducing Stimulation Latencies with High Loss Powers

We next explored whether SORT nanoparticles with improved SLPs can act as efficient transducers to convert AMF into a rapid thermally mediated calcium ion (Ca^{2+}) influx with sub-second latencies.[4, 13] HEK293FT were co-transfected using lipofectamine with TRPV1 and GCaMP6s. The HEK293FT cells were immersed in solutions of MNPs (2 mg/mL of [Fe]) dispersed in Tyrode's solution and exposed to AMF (f = 150 kHz, H_o = 32 kA/m). Within 20 s of the applied field, temperature of the SORT-synthesized MNP solution (SLP = 770±50 $W/g_{[Fe]}$) increased from 36 °C to 43 °C, surpassing the thermal threshold for TRPV1 activation. The AMF-induced Ca^{2+}-influx was manifested as a fluorescence change ($\Delta F/F_o > 50\%$) in 75% of the 120 cells counted across 3 trials (Figure 5A, B). Notably, HEK293FT cells surrounded by SORT-synthesized MNPs exhibited minor and major activation onsets with latencies of ~750 ms and ~5 s respectively (**Figure 7.12A-C**). While the latter influx of Ca^{2+} is due to the bulk temperature increase within the ferrofluid, the former may potentially be attributed to the local heat dissipation by MNPs adjacent to the cell membranes. Consistent with poor heat dissipation, a solution of oxidized MNPs synthesized in SQE at the same particle concentration was not able to reach 40 °C

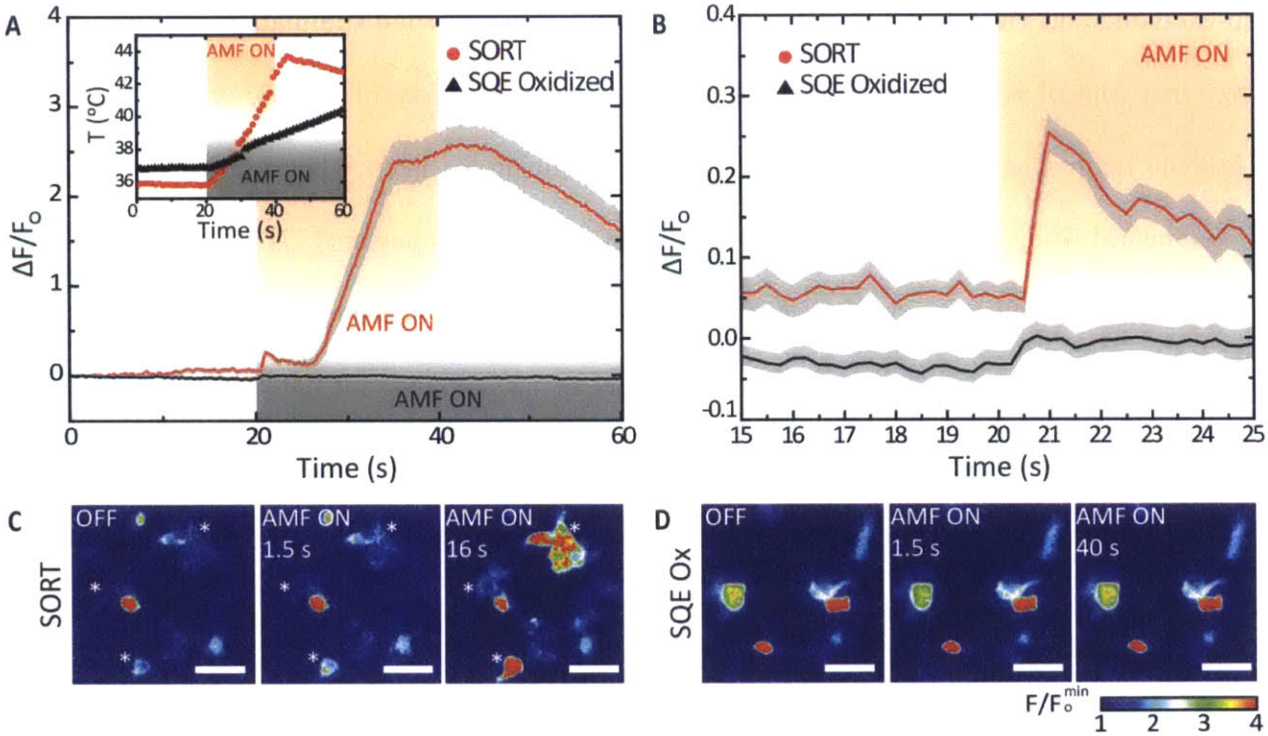

Figure 7.12 High-performance nanoparticles enables rapid magnetothermal control of intracellular concentration (A) Normalized fluorescence traces of GCaMP6s as a function of time averaged over 50 $TRPV1^+$ HEK293FT cells in response to an applied field (duration indicated by AMF ON, f = 150 kHz, H_o = 30 kA/m) for SORT (red line) and SQE Oxidized (black line) nanoparticles at a concentration of 2 mg/mL [Fe]. The shaded grey area indicates standard error. (Inset) Temperature profile of SORT (red) and SQE Oxidized (black) nanoparticle solutions during cell stimulation. (B) Close-up of dashed box in 7.11A showing minor onset within ~750 ms of applied field. Heat maps of fluorescence intensity normalized to baseline before and during field stimulus for HEK293FT cells incubated with (C) SORT and (D) SQE Oxidized nanoparticles. Cells with observable minor onset are denoted with an *. Scale bar = 100 μm.

even after 40 s of AMF exposure, resulting in insignificant intracellular Ca^{2+} increase (**Figure 7.12D**). The improved temporal control over intracellular Ca^{2+} levels with SORT-synthesized nanoparticles is directly correlated to its efficient heat dissipation, which may be therapeutically advantageous in lowering the MNP concentration and AMF exposure time required for other biomedical applications such as cancer hyperthermia.

7.9 Conclusion

In this chapter, we demonstrated widespread and repeatable control of cellular signaling in non-excitable and electroactive cells using wireless magnetothermal stimulation *in vitro* and *in vivo*. Finer control over stimulation intensity to facilitate applications of this approach to problems in systems neuroscience can be achieved by further reducing the latency between field onset and evoked neural firing by developing MNPs with high specific loss powers [77] and by introducing heat-sensitive ion channels with lower thermal thresholds [139]. Mechanosensitive potassium and chloride channels may serve as potential mediators of magnetothermal inhibition [140]. While demonstrated for chronic stimulation of targeted neural circuits, this magnetothermal paradigm may be formulated to trigger thermosensitive ion channels endogenously expressed in the peripheral nervous system [123], enabling wireless control in deep tissue regions that currently pose significant challenges to bioelectronic medicines [141].

Chapter 8

Conclusions and Future Directions

8.1 Thesis Summary

Guided by a general model of dynamic hysteresis, we synthesized ferrite nanoparticles with sizes near the superparamagnetic to ferromagnetic transition that exhibited significant loss powers at clinically relevant AMF conditions. While well-stablished protocols produce ferrite nanoparticles with variable magnetic properties, a novel redox mechanism was identified to assure batch to batch consistency. We found that reducing environments promoted the formation of metastable wüstite coherently embedded in magnetite, which lead to unfavorable exchange coupling and poor hyperthermic performance. Annealing nanoparticles in oxidizing environments was insufficient to promote cation diffusion to remove all defects. By tuning the electrochemical potential of the solvent environment with aromatic ethers, nearly-defect free magnetite nanoparticles were synthesized. The resulting performance of these optimized nanoparticles as both MRI contrast agents and magnetothermal transducers was directly correlated to their defect-free structure. To render the initially hydrophobic nanoparticles water-soluble, we adopted ligands and amphiphiles with multiple binding groups to ensure substantial nanoparticle interaction and reduced the time for phase transfer from a multiday process to tens of minutes. Using 22 nm water-soluble and biocompatible ferrite nanoparticles, we proceeded to stimulate heat-sensitized neurons and demonstrate the feasibility of wireless magnetothermal excitation in arbitrarily deep brain structures. To enable neural excitation with faster dynamics and higher spatial resolution, further steps need to be explored and are proposed below:

8.2 Targeted magnetothermal stimulation

While we relied on global heating of the medium surrounding cells to achieve magnetothermal excitation, recent work has demonstrated the ability of targeted nanoparticles to evoke a similar response [12, 13]. Local temperature at the MNP surface can significantly exceed that of bulk with AMF stimulus and may enable targeted stimulation with sub-second latencies [104, 116, 142]. Indirect measurements of fluorophore release by thermally labile linkers, such as azide decomposition or DNA de-hybridization, have demonstrated that nanoparticles with high loss powers exhibit local surface temperatures >50 K greater than the surrounding solution. The temperature, however, rapidly decays such that no appreciable difference is observed beyond 5 nm from the nanoparticle surface [104]. New experimental schemes and theoretical models need to be established to determine whether sufficient thermal gradients can be reached to repeatedly induce neural excitation.

We begin by developing a nanoscale thermometry platform by coating the optimized nanoparticles in a silica cell impregnated with fluorescent dye [80]. Embedding fluorophores directly into silica coatings is advantageous because it 1) improves the nanoparticles'

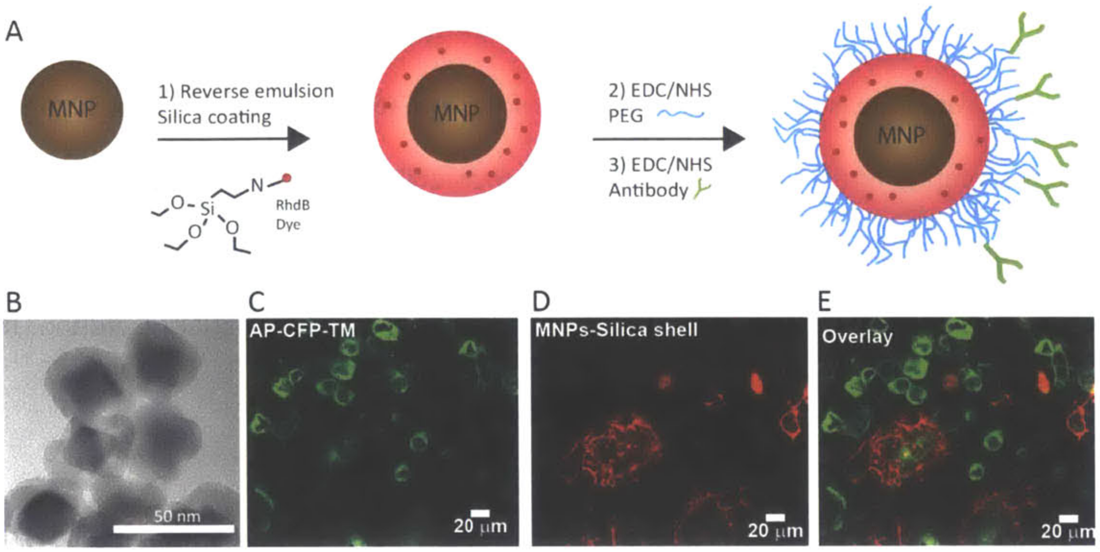

Figure 8.1 (A) Reverse emulsion and surface functionalization scheme for multifunctional nanoparticles that can target neuronal membrane and facilitate nanoscale thermometry measurements. (B) Transmission electron microscope image of amorphous silica coated nanoparticles embedded with rhodamine dye. (C-E) Fluorescence images of HEK 293FT cells (C) transfected with a biotinylated fluorescent protein marker on the cell membrane and (D) incubated with silica coated nanoparticles bound to streptavidin. (E) Overlay of C and D.

biocompatibility and colloidal stability, 2) increases fluorescence lifetime compared to free dye due to elimination of non-radiative recombination processes, 3) protects the dye from photobleaching, and 4) enables nanoscale thermometry due to temperature dependent changes in the dye's quantum yield [80]. We have utilized a reverse microemulsion protocol to coat our nanoparticles with rhodamine-doped amorphous silica and interfaced the nanoparticles to the cell membrane [80, 143] (**Figure 8.1**). This experimental scheme, which allows for tunable shell thickness and nanoparticle distance from the membrane surface, may allow direct correlation of SLP determined from bulk measurements to nanoscale heat transfer events on the cell membrane.

8.3 Multiplexed Heating of Multiple Targets

We recently identified that selective heating of different nanoparticle populations collocated in the same volume was possible by tailoring the nanoparticle's chemical composition and size to the AMF driving conditions [6]. MNPs operated at amplitudes close to their coercive field will produce maximal hysteretic losses per cycle. Hence, nanoparticles with different coercivities can be selectively heated at different field amplitudes and frequencies. We demonstrated this concept of multiplexed heating with 22 nm iron oxide nanoparticles subjected to two different field conditions at 100 kHz and 35 kA/m (Mode I) and at 2.55 MHz and 5 kA/m (Mode II), which exhibited SLPs of 500 W/g and 40 W/g respectively [6]. Less coercive manganese-doped ferrite nanoparticles 13 nm in diameter dissipated SLPs of 30 W/g at Mode I and 400 W/g at Mode II. We believe that selective heating of different nanoparticle populations can lead to multiplexed control of different neural circuits or drive both neural excitation and inhibition when interfaced to two types of ion channels [140].

To realize this experimental scheme *in vivo*, further optimization of the materials set is required to identify alternating magnetic field conditions that are readily accessible for robust multiplexing. Ideally, the field amplitude and frequency should be closer in magnitude such that the same hardware architecture can be used to switch between driving modes [6]. The SORT

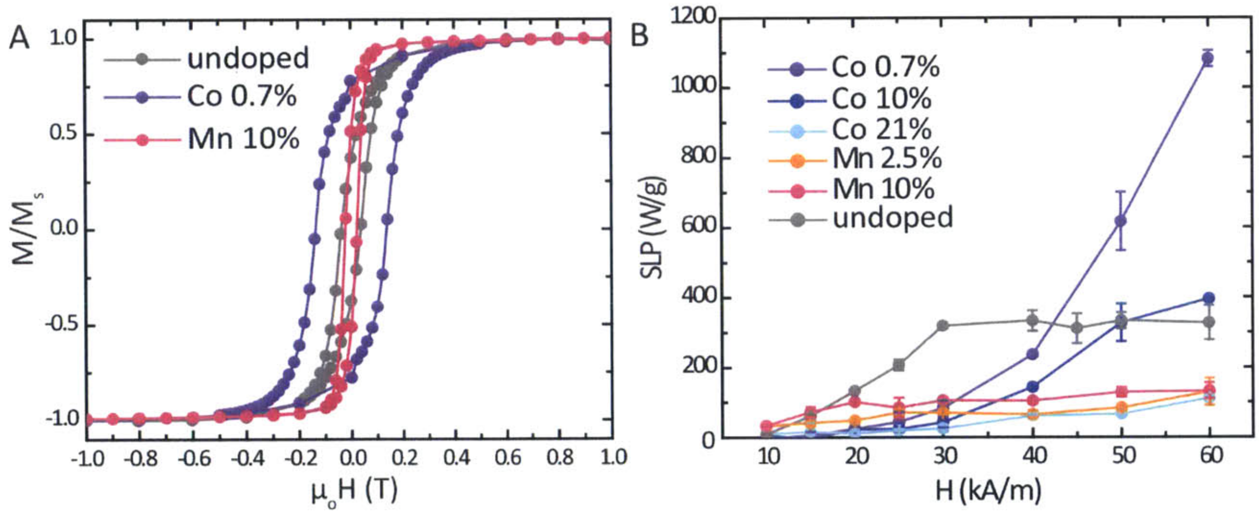

Figure 8.2 (A) Normalized magnetization curve measured at 5 K of 18 nm nanoparticles with different composition. (B) SLP measurement conducted at a frequency of 100 kHz at amplitudes 10-60 kA/m for 18 nm nanoparticles doped with different amounts of manganese or cobalt.

method developed in Chapter 4 was used to synthesize 18 nm nanoparticles with different dopant concentrations of manganese and cobalt. Compared to iron oxide, we find that incorporation of 10% manganese decreased the coercive field from 33 to 22 mT measured at 5 K (**Figure 8.2A**). Incorporation of just 0.7% cobalt increased the coercivity to 133 mT. Calorimetry in the presence of AMF with a frequency of 100 kHz revealed dramatic effects doping had on SLP dependence on field amplitude (**Figure 8.2B**). Cobalt doping necessitated higher field amplitudes to access large SLPs while manganese incorporation resulted in lower hysteretic losses compared to iron oxide. This preliminary work demonstrates the possibilities of identifying new modes to achieve magnetothermal multiplexing with subtle changes in the chemical composition of the nanoparticles.

8.4 Shaping Behavior with Magnetothermal Stimulation

In Chapter 7, we presented indirect evidence of neural excitation by immunohistochemistry staining for the immediate early gene marker c-fos. To demonstrate dynamic stimulation effects on neural activity, we propose to use fiber photometry in freely-behaving rodents and to correlate magnetothermal stimulation with behavioral changes [136].

Because noise from the AMF hardware can drown signals recorded with standard electrophysiology, we can employ optical readout methods to measure neural activity. Fiber photometry utilizes a fiber optic to record calcium fluorescence changes from neurons expressing the genetically encoded calcium indicator GCaMP6 [127, 136]. A 473 nm laser is used to excite neurons expressing GCaMP6s through the fiber optic and green emission at 512 nm is filtered through a dichroic and a band pass and read out by a femtowatt photodetector (**Figure 8.3**). This optical setup allowed us to record GCaMP6s activity from the VTA upon pinching the paw of an anesthetized mouse and will allow us to correlate fluorescence signal changes with magnetothermal stimulation of neurons co-expressing TRPV1 and GCaMP6s.

Phasic excitation of dopaminergic neurons in the VTA and its projections to the NAc is a strong reinforcer for reward [31]. The possibility for MNPs to remotely control behavior through magnetothermal stimulation will be investigated by stimulation of this neural circuit. We plan to construct a two chamber behavioral setup to demonstrate conditioned place preference for the chamber subjected to AMF.

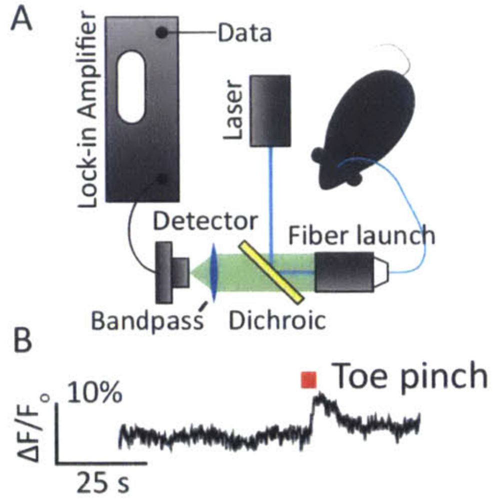

Figure 8.3 (A) Schematic of fiber photometry setup. A 473 nm laser is used to excite GCaMP6s expressed in a mouse. The 512 nm emission is passed through a dichroic and filtered through a bandpass into a photodetector. A lock-in amplifier amplifies signal from a certain frequency to reduce noise. (B) Fluorescence trace of GCaMP6s in a freely moving mouse. Upon toe pinch, increased neural activity is observed in the VTA.

8.5 Thesis Conclusion

Current neuromodulation technologies for deep brain stimulation require the implantation of tethered probes. While wireless features may be integrated [29, 30, 144], devices that can perturb neural circuits in arbitrarily deep brain structures without the reliance on transgenes remains to be demonstrated. Alternative contactless methods, such as transcranial magnetic and ultrasound stimulation, are limited primarily to superficial brain structures with limited spatial resolution exceeding >1 mm [19, 145]. The coupling of wirelessly applied stimuli with engineered nanomaterials may facilitate localized control of neural activity without the need for implanted hardware. We have demonstrated a proof-of-concept experiment as a first step towards realizing contactless neuromodulation with cellular specificity by stimulating heat sensitized neurons *in vitro* and *in vivo* with magnetic nanoparticles. Improving this technique will require targeting nanoparticles to the neuronal membrane, which may translate to magnetothermal stimulation with sub-second latencies. Endogenously expressed ion channels that can respond to heat will also need to be identified. Further efficacy studies such as eliciting behavior and correlation with electrophysiological recording *in vivo* may eventually lead to adoption of nanomaterial technologies by the neuroscience community. In conjunction with neural stimulation by surface plasmons on gold nanoparticles [34], piezoelectric conversion of ultrasound with ferroelectric nanoparticles [37], and photoelectricity generated by quantum dot [146], nanomaterials present exciting possibilities for next-generation minimally invasive bioelectronics tools. Pending further safety and efficacy studies, nanoparticle mediated stimulation may facilitate the treatment of neurological and non-neurological diseases, where nanoparticles are orally administered and wirelessly activated to repair broken cellular pathways as a new class of non-pharmacological medicine.

References

1. Chen, R., M.G. Christiansen, and P. Anikeeva, *Maximizing Hysteretic Losses in Magnetic Ferrite Nanoparticles via Model-Driven Synthesis and Materials Optimization.* ACS Nano, 2013. **7**(10): p. 8990-9000.
2. Chen, R., et al., *High-Performance Ferrite Nanoparticles through Nonaqueous Redox Phase Tuning.* Nano Letters, 2016. **16**(2): p. 1345-1351.
3. O'handley, R.C., *Modern magnetic materials: principles and applications.* Vol. 830622677. 2000: Wiley New York.
4. Chen, R., et al., *Wireless magnetothermal deep brain stimulation.* Science, 2015. **347**(6229): p. 1477-1480.
5. van Embden, J., A.S.R. Chesman, and J.J. Jasieniak, *The Heat-Up Synthesis of Colloidal Nanocrystals.* Chemistry of Materials, 2015. **27**(7): p. 2246-2285.
6. Christiansen, M.G., et al., *Magnetically multiplexed heating of single domain nanoparticles.* Applied Physics Letters, 2014. **104**(21): p. -.
7. Insel, T.R., S.C. Landis, and F.S. Collins, *The NIH brain initiative.* Science, 2013. **340**(6133): p. 687-688.
8. Boyden, E.S., et al., *Millisecond-timescale, genetically targeted optical control of neural activity.* Nat Neurosci, 2005. **8**(9): p. 1263-1268.
9. Armbruster, B.N., et al., *Evolving the lock to fit the key to create a family of G protein-coupled receptors potently activated by an inert ligand.* Proceedings of the National Academy of Sciences, 2007. **104**(12): p. 5163-5168.
10. Kotov, N.A., et al., *Nanomaterials for neural interfaces.* Advanced Materials, 2009. **21**(40): p. 3970-4004.
11. Wang, Y. and L. Guo, *Nanomaterial-Enabled Neural Stimulation.* Frontiers in Neuroscience, 2016. **10**: p. 69.
12. Huang, H., et al., *Remote Control of Ion Channels and Neurons through Magnetic-Field Heating of Nanoparticles*, in *Nature Nanotechnology*2010. p. 602-606.
13. Stanley, S.A., et al., *Radio-Wave Heating of Iron Oxide Nanoparticles Can Regulate Plasma Glucose in Mice.* Science, 2012. **336**(6081): p. 604-608.
14. Lee, N., et al., *Iron Oxide Based Nanoparticles for Multimodal Imaging and Magnetoresponsive Therapy.* Chemical Reviews, 2015. **115**(19): p. 10637-10689.
15. Lee, N. and T. Hyeon, *Designed synthesis of uniformly sized iron oxide nanoparticles for efficient magnetic resonance imaging contrast agents.* Chemical Society Reviews, 2012. **41**(7): p. 2575-2589.
16. Mayberg, H.S., et al., *Deep Brain Stimulation for Treatment-Resistant Depression.* Neuron, 2005. **45**(5): p. 651-660.
17. Perlmutter, J.S. and J.W. Mink, *Deep brain stimulation.* Annu. Rev. Neurosci., 2006. **29**: p. 229-257.
18. Gradinaru, V., et al., *Optical Deconstruction of Parkinsonian Neural Circuitry.* Science, 2009. **324**(5925): p. 354-359.

19. Walsh, V. and A. Cowey, *Transcranial magnetic stimulation and cognitive neuroscience.* Nat Rev Neurosci, 2000. **1**(1): p. 73-80.
20. Nitsche, M.A., et al., *Transcranial direct current stimulation: State of the art 2008.* Brain Stimulation, 2008. **1**(3): p. 206-223.
21. Bean, B.P., *The action potential in mammalian central neurons.* Nat Rev Neurosci, 2007. **8**(6): p. 451-465.
22. Kirkton, R.D. and N. Bursac, *Engineering biosynthetic excitable tissues from unexcitable cells for electrophysiological and cell therapy studies.* Nat Commun, 2011. **2**: p. 300.
23. Clapham, D.E., L.W. Runnels, and C. Strubing, *The trp ion channel family.* Nat Rev Neurosci, 2001. **2**(6): p. 387-396.
24. Liao, M., et al., *Structure of the TRPV1 ion channel determined by electron cryo-microscopy.* Nature, 2013. **504**(7478): p. 107-112.
25. Caterina, M.J., et al., *The capsaicin receptor: a heat-activated ion channel in the pain pathway.* Nature, 1997. **389**(6653): p. 816-824.
26. Tóth, A., et al., *Expression and distribution of vanilloid receptor 1 (TRPV1) in the adult rat brain.* Molecular Brain Research, 2005. **135**(1–2): p. 162-168.
27. Tye, K.M. and K. Deisseroth, *Optogenetic investigation of neural circuits underlying brain disease in animal models.* Nat Rev Neurosci, 2012. **13**(4): p. 251-266.
28. Yizhar, O., et al., *Optogenetics in Neural Systems.* Neuron, 2011. **71**(1): p. 9-34.
29. Kim, T.-i., et al., *Injectable, Cellular-Scale Optoelectronics with Applications for Wireless Optogenetics.* Science, 2013. **340**(6129): p. 211-216.
30. Park, S.I., et al., *Soft, stretchable, fully implantable miniaturized optoelectronic systems for wireless optogenetics.* Nat Biotech, 2015. **33**(12): p. 1280-1286.
31. Tye, K.M., et al., *Dopamine neurons modulate neural encoding and expression of depression-related behaviour.* Nature, 2012. **493**: p. 537–541.
32. Urban, D.J. and B.L. Roth, *DREADDs (designer receptors exclusively activated by designer drugs): chemogenetic tools with therapeutic utility.* Annual review of pharmacology and toxicology, 2015. **55**: p. 399-417.
33. Alexander, G.M., et al., *Remote Control of Neuronal Activity in Transgenic Mice Expressing Evolved G Protein-Coupled Receptors.* Neuron, 2009. **63**(1): p. 27-39.
34. Carvalho-de-Souza, João L., et al., *Photosensitivity of Neurons Enabled by Cell-Targeted Gold Nanoparticles.* Neuron. **86**(1): p. 207-217.
35. Nikoobakht, B. and M.A. El-Sayed, *Preparation and Growth Mechanism of Gold Nanorods (NRs) Using Seed-Mediated Growth Method.* Chemistry of Materials, 2003. **15**(10): p. 1957-1962.
36. Nakatsuji, H., et al., *Thermosensitive Ion Channel Activation in Single Neuronal Cells by Using Surface-Engineered Plasmonic Nanoparticles.* Angewandte Chemie International Edition, 2015. **54**(40): p. 11725-11729.
37. Marino, A., et al., *Piezoelectric Nanoparticle-Assisted Wireless Neuronal Stimulation.* ACS Nano, 2015. **9**(7): p. 7678-7689.
38. Young, J.H., M.T. Wang, and I.A. Brezovich, *Frequency/depth-penetration considerations in hyperthermia by magnetically induced currents.* Electronics Letters, 1980. **16**(10): p. 358-359.
39. Mannix, R.J., et al., *Nanomagnetic actuation of receptor-mediated signal transduction.* Nat Nano, 2008. **3**(1): p. 36-40.

40. Liu, X.L., et al., *Magnetic Vortex Nanorings: A New Class of Hyperthermia Agent for Highly Efficient In Vivo Regression of Tumors.* Advanced Materials, 2015. **27**(11): p. 1939-1944.
41. van Landeghem, F.K.H., et al., *Post-mortem studies in glioblastoma patients treated with thermotherapy using magnetic nanoparticles.* Biomaterials, 2009. **30**(1): p. 52-57.
42. Jang, J., et al., *Critical Enhancements of MRI Contrast and Hyperthermic Effects by Dopant-Controlled Magnetic Nanoparticles.* Angewandte Chemie, International Edition, 2009. **48**(7): p. 1234-1238.
43. Slonczewski, J., *Origin of magnetic anisotropy in cobalt-substituted magnetite.* Physical Review, 1958. **110**(6): p. 1341.
44. Shavel, A. and L.M. Liz-Marzan, *Shape control of iron oxide nanoparticles.* Physical Chemistry Chemical Physics, 2009. **11**(19): p. 3762-3766.
45. Hou, Y., Z. Xu, and S. Sun, *Controlled Synthesis and Chemical Conversions of FeO Nanoparticles.* Angewandte Chemie, International Edition, 2007. **46**(33): p. 6329-6332.
46. Sun, X., et al., *Tuning Exchange Bias in Core/Shell FeO/Fe3O4 Nanoparticles.* Nano Letters, 2012. **12**(1): p. 246-251.
47. Redl, F.X., et al., *Magnetic, electronic, and structural characterization of nonstoichiometric iron oxides at the nanoscale.* Journal of the American Chemical Society, 2004. **126**(44): p. 14583-14599.
48. O'Brien, S., L. Brus, and C.B. Murray, *Synthesis of monodisperse nanoparticles of barium titanate: Toward a generalized strategy of oxide nanoparticle synthesis.* Journal of the American Chemical Society, 2001. **123**(48): p. 12085-12086.
49. Wetterskog, E., et al., *Anomalous Magnetic Properties of Nanoparticles Arising from Defect Structures: Topotaxial Oxidation of Fe1−xO|Fe3−δO4 Core|Shell Nanocubes to Single-Phase Particles.* ACS Nano, 2013. **7**(8): p. 7132-7144.
50. Levy, M., et al., *Correlating Magneto-Structural Properties to Hyperthermia Performance of Highly Monodisperse Iron Oxide Nanoparticles Prepared by a Seeded-Growth Route.* Chemistry of Materials, 2011. **23**(18): p. 4170-4180.
51. Walter, A., et al., *Mastering the Shape and Composition of Dendronized Iron Oxide Nanoparticles To Tailor Magnetic Resonance Imaging and Hyperthermia.* Chemistry of Materials, 2014. **26**(18): p. 5252-5264.
52. Laurent, S., et al., *Magnetic iron oxide nanoparticles: synthesis, stabilization, vectorization, physicochemical characterizations, and biological applications.* Chemical reviews, 2008. **108**(6): p. 2064.
53. Pankhurst, Q.A., et al., *Progress in applications of magnetic nanoparticles in biomedicine.* Journal of Physics D: Applied Physics, 2009. **42**(22): p. 224001.
54. Jordan, A., et al., *Magnetic fluid hyperthermia (MFH): Cancer treatment with AC magnetic field induced excitation of biocompatible superparamagnetic nanoparticles.* Journal of Magnetism and Magnetic Materials, 1999. **201**(1–3): p. 413-419.
55. Aragón, R., *Cubic magnetic anisotropy of nonstoichiometric magnetite.* Physical Review B, 1992. **46**(9): p. 5334-5338.
56. Jamet, M., et al., *Magnetic Anisotropy of a Single Cobalt Nanocluster.* Physical Review Letters, 2001. **86**(20): p. 4676-4679.
57. Salazar-Alvarez, G., et al., *Cubic versus Spherical Magnetic Nanoparticles: The Role of Surface Anisotropy.* Journal of the American Chemical Society, 2008. **130**(40): p. 13234-13239.

58. Carrey, J., B. Mehdaoui, and M. Respaud, *Simple Models for Dynamic Hysteresis Loop Calculations of Magnetic Single-domain Nanoparticles: Application to Magnetic Hyperthermia Optimization.* Journal of Applied Physics, 2011. **109**(8): p. 083921-17.
59. Guardia, P., et al., *Water-Soluble Iron Oxide Nanocubes with High Values of Specific Absorption Rate for Cancer Cell Hyperthermia Treatment.* ACS Nano, 2012. **6**(4): p. 3080-3091.
60. Lee, J.-H., et al., *Exchange-coupled magnetic nanoparticles for efficient heat induction.* Nat Nano. **6**(7): p. 418-422.
61. Fortin, J.-P., et al., *Size-Sorted Anionic Iron Oxide Nanomagnets as Colloidal Mediators for Magnetic Hyperthermia.* Journal of the American Chemical Society, 2007. **129**(9): p. 2628-2635.
62. Rosensweig, R.E., *Heating Magnetic Fluid with Alternating Magnetic Field.* Journal of Magnetism and Magnetic Materials, 2002. **252**(0): p. 370-374.
63. Stoner, E.C. and E.P. Wohlfarth, *A Mechanism of Magnetic Hysteresis in Heterogeneous Alloys.* Philosophical Transactions of the Royal Society of London. Series A. Mathematical and Physical Sciences, 1948: p. 599-642.
64. Usov, N.A. and Y.B. Grebenshchikov, *Hysteresis Loops of an Assembly of Superparamagnetic Nanoparticles with Uniaxial Anisotropy.* Journal of Applied Physics, 2009. **106**(2): p. 023917-11.
65. Ibusuki, T., et al., *Magnetic Anisotropy and Behaviors of Fe Nanoparticles.* Magnetics, IEEE Transactions on, 2001. **37**(4): p. 2223-2225.
66. Navrotsky, A., L. Mazeina, and J. Majzlan, *Size-Driven Structural and Thermodynamic Complexity in Iron Oxides.* Science, 2008. **319**(5870): p. 1635-1638.
67. Murray, C.B., D.J. Norris, and M.G. Bawendi, *Synthesis and characterization of nearly monodisperse CdE (E = sulfur, selenium, tellurium) semiconductor nanocrystallites.* Journal of the American Chemical Society, 1993. **115**(19): p. 8706-8715.
68. Park, J., et al., *Ultra-Large-Scale Syntheses of Monodisperse Nanocrystals.* Nat Mater, 2004. **3**(12): p. 891-895.
69. LaMer, V.K. and R.H. Dinegar, *Theory, Production and Mechanism of Formation of Monodispersed Hydrosols.* Journal of the American Chemical Society, 1950. **72**(11): p. 4847-4854.
70. Park, J., et al., *Synthesis of Monodisperse Spherical Nanocrystals.* Angewandte Chemie, International Edition, 2007. **46**(25): p. 4630-4660.
71. Bao, N., et al., *A Facile Thermolysis Route to Monodisperse Ferrite Nanocrystals.* Journal of the American Chemical Society, 2007. **129**(41): p. 12374-12375.
72. Sun, S., et al., *Monodisperse MFe2O4 (M = Fe, Co, Mn) Nanoparticles.* Journal of the American Chemical Society, 2003. **126**(1): p. 273-279.
73. Bronstein, L.M., et al., *Influence of Iron Oleate Complex Structure on Iron Oxide Nanoparticle Formation.* Chemistry of Materials, 2007. **19**(15): p. 3624-3632.
74. Bao, N., et al., *Formation Mechanism and Shape Control of Monodisperse Magnetic CoFe2O4 Nanocrystals.* Chemistry of Materials, 2009. **21**(14): p. 3458-3468.
75. Kwon, S.G., et al., *Kinetics of Monodisperse Iron Oxide Nanocrystal Formation by "Heating-Up" Process.* Journal of the American Chemical Society, 2007. **129**(41): p. 12571-12584.

76. Song, Q., et al., *Tuning the Thermal Stability of Molecular Precursors for the Nonhydrolytic Synthesis of Magnetic MnFe2O4 Spinel Nanocrystals.* Chemistry of Materials, 2007. **19**(19): p. 4633-4638.
77. Lee, J., et al., *Exchange-coupled Magnetic Nanoparticles for Efficient Heat Induction.* Nature Nanotechnology, 2011. **6**(7): p. 418-422.
78. Xie, J., et al., *One-Pot Synthesis of Monodisperse Iron Oxide Nanoparticles for Potential Biomedical Applications.* Pure and applied chemistry, 2006. **78**(5): p. 1003-1014.
79. Noh, S., et al., *Nanoscale Magnetism Control via Surface and Exchange Anisotropy for Optimized Ferrimagnetic Hysteresis.* Nano Letters, 2012. **12**(7): p. 3716-3721.
80. Zhang, H., et al., *Monodisperse Magnetofluorescent Nanoplatforms for Local Heating and Temperature Sensing.* Nanoscale, 2014. **6**: p. 13463.
81. Pichon, B.P., et al., *Microstructural and Magnetic Investigations of Wüstite-Spinel Core-Shell Cubic-Shaped Nanoparticles.* Chemistry of Materials, 2011. **23**(11): p. 2886-2900.
82. Chen, O., et al., *Synthesis of Metal–Selenide Nanocrystals Using Selenium Dioxide as the Selenium Precursor.* Angewandte Chemie International Edition, 2008. **47**(45): p. 8638-8641.
83. Gilbert, K.E. and J.J. Gajewski, *Coal liquefaction model studies: free radical chain decomposition of diphenylpropane, dibenzyl ether, and phenethyl phenyl ether via .beta.-scission reactions.* The Journal of Organic Chemistry, 1982. **47**(25): p. 4899-4902.
84. Hai, H.T., et al., *Size control and characterization of wustite (core)/spinel (shell) nanocubes obtained by decomposition of iron oleate complex.* Journal of Colloid and Interface Science, 2010. **346**(1): p. 37-42.
85. Baxendale, J.H. and J. Magee, *The oxidation of benzene by hydrogen peroxide and iron salts.* Discuss. Faraday Soc., 1953. **14**: p. 160-169.
86. Kim, D., et al., *Synthesis of uniform ferrimagnetic magnetite nanocubes.* Journal of the American Chemical Society, 2008. **131**(2): p. 454-455.
87. Kovalenko, M.V., et al., *Fatty Acid Salts as Stabilizers in Size- and Shape-Controlled Nanocrystal Synthesis: The Case of Inverse Spinel Iron Oxide.* Journal of the American Chemical Society, 2007. **129**(20): p. 6352-6353.
88. Casula, M.F., et al., *The Concept of Delayed Nucleation in Nanocrystal Growth Demonstrated for the Case of Iron Oxide Nanodisks.* Journal of the American Chemical Society, 2006. **128**(5): p. 1675-1682.
89. Hai, H.T., et al., *Phase transformation of FeO/Fe 3 O 4 core/shell nanocubes and facile synthesis of Fe 3 O 4 nanocubes.* Journal of Applied Physics, 2010. **107**(9): p. 09E301-09E301-3.
90. Salas, G., et al., *Controlled Synthesis of Uniform Magnetite Nanocrystals with High-Quality Properties for Biomedical Applications.* Journal of Materials Chemistry, 2012. **22**(39): p. 21065-21075.
91. Xu, Y., et al., *Water-Soluble Iron Oxide Nanoparticles with High Stability and Selective Surface Functionality.* Langmuir, 2011. **27**(14): p. 8990-8997.
92. Mittemeijer, E.J. and U. Welzel, *The "state of the art" of the diffraction analysis of crystallite size and lattice strain.* Zeitschrift für Kristallographie International journal for structural, physical, and chemical aspects of crystalline materials, 2008. **223**(9): p. 552-560.
93. Morales, M.P., et al., *Surface and Internal Spin Canting in γ-Fe2O3 Nanoparticles.* Chemistry of Materials, 1999. **11**(11): p. 3058-3064.

94. Nogués, J. and I.K. Schuller, *Exchange Bias.* Journal of Magnetism and Magnetic Materials, 1999. **192**(2): p. 203-232.

95. Nogués, J., et al., *Exchange Bias in Nanostructures.* Physics Reports, 2005. **422**(3): p. 65-117.

96. Kavich, D.W., et al., *Exchange Bias of Singly Inverted FeO/Fe3O4 Core-Shell Nanocrystals.* Physical Review B, 2008. **78**(17): p. 174414.

97. Lee, J., et al., *Size Dependence of Metal–Insulator Transition in Stoichiometric Fe3O4 Nanocrystals.* Nano Letters, 2015. **15**(7): p. 4337-4342.

98. Senn, M.S., J.P. Wright, and J.P. Attfield, *Charge order and three-site distortions in the Verwey structure of magnetite.* Nature, 2012. **481**(7380): p. 173-176.

99. Baaziz, W., et al., *Tuning of Synthesis Conditions by Thermal Decomposition toward Core–Shell CoxFe1–xO@CoyFe3–yO4 and CoFe2O4 Nanoparticles with Spherical and Cubic Shapes.* Chemistry of Materials, 2014. **26**(17): p. 5063-5073.

100. Xu, Y., et al., *A general approach to the synthesis and detailed characterization of magnetic ferrite nanocubes.* Nanoscale, 2015. **7**(29): p. 12641-12649.

101. Wu, W., Q. He, and C. Jiang, *Magnetic Iron Oxide Nanoparticles: Synthesis and Surface Functionalization Strategies.* Nanoscale Research Letters, 2008. **3**(11): p. 397-415.

102. Palma, S.I.C.J., et al., *Effects of phase transfer ligands on monodisperse iron oxide magnetic nanoparticles.* Journal of Colloid and Interface Science, 2015. **437**: p. 147-155.

103. Wijaya, A. and K. Hamad-Schifferli, *High-Density Encapsulation of Fe3O4 Nanoparticles in Lipid Vesicles.* Langmuir, 2007. **23**(19): p. 9546-9550.

104. Riedinger, A., et al., *Subnanometer Local Temperature Probing and Remotely Controlled Drug Release Based on Azo-Functionalized Iron Oxide Nanoparticles.* Nano Letters, 2013. **13**(6): p. 2399-2406.

105. Zhang, T., et al., *A General Approach for Transferring Hydrophobic Nanocrystals into Water.* Nano Letters, 2007. **7**(10): p. 3203-3207.

106. Yu, W.W., et al., *Forming biocompatible and nonaggregated nanocrystals in water using amphiphilic polymers.* Journal of the American Chemical Society, 2007. **129**(10): p. 2871-2879.

107. Schöttler, S., et al., *Protein adsorption is required for stealth effect of poly(ethylene glycol)- and poly(phosphoester)-coated nanocarriers.* Nat Nano, 2016. **advance online publication**.

108. Fröhlich, E., *The role of surface charge in cellular uptake and cytotoxicity of medical nanoparticles.* International Journal of Nanomedicine, 2012. **7**: p. 5577-5591.

109. Wei, H., et al., *Compact Zwitterion-Coated Iron Oxide Nanoparticles for Biological Applications.* Nano Letters, 2012. **12**(1): p. 22-25.

110. Fortin, J., et al., *Size-Sorted Anionic Iron Oxide Nanomagnets as Colloidal Mediators for Magnetic Hyperthermia.* Journal of the American Chemical Society, 2007. **129**(9): p. 2628-2635.

111. Arora, S.K., et al., *Antiphase boundaries induced exchange coupling in epitaxial Fe3O4 thin films.* Journal of Magnetism and Magnetic Materials, 2005. **286**: p. 463-467.

112. Kallumadil, M., et al., *Suitability of commercial colloids for magnetic hyperthermia.* Journal of Magnetism and Magnetic Materials, 2009. **321**(10): p. 1509-1513.

113. Lee, N., et al., *Water-Dispersible Ferrimagnetic Iron Oxide Nanocubes with Extremely High r2 Relaxivity for Highly Sensitive in Vivo MRI of Tumors.* Nano Letters, 2012. **12**(6): p. 3127-3131.

114. Rabin, Y., *Is intracellular hyperthermia superior to extracellular hyperthermia in the thermal sense?* Int. J. Hyperther., 2002. **18**(3): p. 194-202.
115. Keblinski, P., et al., *Limits of localized heating by electromagnetically excited nanoparticles.* Journal of applied physics, 2006. **100**(5): p. 054305.
116. Dong, J. and J.I. Zink, *Taking the Temperature of the Interiors of Magnetically Heated Nanoparticles.* ACS Nano, 2014. **8**(5): p. 5199-5207.
117. Piñol, R., et al., *Joining Time-Resolved Thermometry and Magnetic-Induced Heating in a Single Nanoparticle Unveils Intriguing Thermal Properties.* ACS Nano, 2015. **9**(3): p. 3134-3142.
118. Hoogeboom-Pot, K.M., et al., *A new regime of nanoscale thermal transport: Collective diffusion increases dissipation efficiency.* Proceedings of the National Academy of Sciences, 2015. **112**(16): p. 4846-4851.
119. Tenzer, S., et al., *Rapid formation of plasma protein corona critically affects nanoparticle pathophysiology.* Nature Nanotechnology, 2013. **8**(10): p. 772-781.
120. Salvati, A., et al., *Transferrin-functionalized nanoparticles lose their targeting capabilities when a biomolecule corona adsorbs on the surface.* Nature Nanotechnology, 2013. **8**(2): p. 137-143.
121. Petters, C., et al., *Uptake and Metabolism of Iron Oxide Nanoparticles in Brain Cells.* Neurochemical Research, 2014. **39**(9): p. 1648-1660.
122. Maier-Hauff, K., et al., *Efficacy and safety of intratumoral thermotherapy using magnetic iron-oxide nanoparticles combined with external beam radiotherapy on patients with recurrent glioblastoma multiforme.* Journal of Neuro-Oncology, 2011. **103**(2): p. 317-324.
123. Basbaum, A.I., et al., *Cellular and Molecular Mechanisms of Pain.* Cell, 2009. **139**(2): p. 267-284.
124. Naldini, L., et al., *Efficient transfer, integration, and sustained long-term expression of the transgene in adult rat brains injected with a lentiviral vector.* Proc. Natl. Acad. Sci. U.S.A, 1996. **93**(21): p. 11382-11388.
125. Kim, J.H., et al., *High Cleavage Efficiency of a 2A Peptide Derived from Porcine Teschovirus-1 in Human Cell Lines, Zebrafish and Mice.* PLoS ONE, 2011. **6**(4): p. e18556.
126. Asante-Appiah, E. and A.M. Skalka, *Molecular mechanisms in retrovirus DNA integration.* Antiviral Research, 1997. **36**(3): p. 139-156.
127. Chen, T.-W., et al., *Ultrasensitive fluorescent proteins for imaging neuronal activity.* Nature, 2013. **499**(7458): p. 295-300.
128. Shapiro, M.G., et al., *Infrared light excites cells by changing their electrical capacitance.* Nat Commun, 2012. **3**: p. 736.
129. Grewę, B.F., et al., *High-speed in vivo calcium imaging reveals neuronal network activity with near-millisecond precision.* Nat Meth, 2010. **7**(5): p. 399-405.
130. White, M.G., et al., *Caspase activation contributes to delayed death of heat-stressed striatal neurons.* Journal of Neurochemistry, 2003. **87**(4): p. 958-968.
131. Lepock, J.R., *Cellular effects of hyperthermia: relevance to the minimum dose for thermal damage.* Int. J. Hyperther., 2003. **19**(3): p. 252-266.
132. Leith, J.T., et al., *Hyperthermic potentiation. Biological aspects and applications to radiation therapy.* Cancer, 1977. **39**(S2): p. 766-779.

133. Cavanaugh, D.J., et al., *Trpv1 reporter mice reveal highly restricted brain distribution and functional expression in arteriolar smooth muscle cells.* J. Neurosci., 2011. **31**(13): p. 5067-5077.
134. Swanson, L.W., *The projections of the ventral tegmental area and adjacent regions: a combined fluorescent retrograde tracer and immunofluorescence study in the rat.* Brain research bulletin, 1982. **9**(1): p. 321-353.
135. Hunt, S.P., A. Pini, and G. Evan, *Induction of c-fos-like protein in spinal cord neurons following sensory stimulation.* Nature, 1987(328): p. 632-634.
136. Gunaydin, Lisa A., et al., *Natural Neural Projection Dynamics Underlying Social Behavior.* Cell, 2014. **157**(7): p. 1535-1551.
137. Polikov, V.S., P.A. Tresco, and W.M. Reichert, *Response of brain tissue to chronically implanted neural electrodes.* Journal of neuroscience methods, 2005. **148**(1): p. 1-18.
138. Silver, J. and J.H. Miller, *Regeneration beyond the glial scar.* Nature Reviews Neuroscience, 2004. **5**(2): p. 146-156.
139. Gracheva, E.O., et al., *Molecular basis of infrared detection by snakes.* Nature, 2010. **464**(7291): p. 1006-1011.
140. Yoo, S., et al., *Photothermal Inhibition of Neural Activity with Near-Infrared-Sensitive Nanotransducers.* ACS Nano, 2014. **8**(8): p. 8040-8049.
141. Birmingham, K., et al., *Bioelectronic medicines: a research roadmap.* Nat Rev Drug Discov, 2014. **13**(6): p. 399-400.
142. Dias, J.T., et al., *DNA as a Molecular Local Thermal Probe for the Analysis of Magnetic Hyperthermia.* Angewandte Chemie International Edition, 2013. **52**(44): p. 11526-11529.
143. Lu, Y., et al., *Modifying the Surface Properties of Superparamagnetic Iron Oxide Nanoparticles through A Sol−Gel Approach.* Nano Letters, 2002. **2**(3): p. 183-186.
144. Montgomery, K.L., et al., *Wirelessly powered, fully internal optogenetics for brain, spinal and peripheral circuits in mice.* Nat Meth, 2015. **12**(10): p. 969-974.
145. Legon, W., et al., *Transcranial focused ultrasound modulates the activity of primary somatosensory cortex in humans.* Nat Neurosci, 2014. **17**(2): p. 322-329.
146. Pappas, T.C., et al., *Nanoscale Engineering of a Cellular Interface with Semiconductor Nanoparticle Films for Photoelectric Stimulation of Neurons.* Nano Letters, 2007. **7**(2): p. 513-519.